Study on Stability Control and Low-Cost Structure of Power Converter for Doubly-Fed Induction Generator Wind Turbine

by

Danvu Nguyen

B.E. Hon. (Hochiminh University of Technology) 2010
M.E. (Shibaura Institute of Technology) 2012

A dissertation submitted in partial satisfaction
of the requirements for the degree of Ph.D in Electrical Engineering

in the

GRADUATE SCHOOL

SHIBAURA INSTITUTE OF TECHNOLOGY

September 2015

Study on Stability Control and Low-Cost Structure of Power Converter for Doubly-Fed Induction Generator Wind Turbine

by

Danvu Nguyen

Acknowledgements

Pursuit of PhD degree is a tough and intense period for me, and it has not been possible to complete this work without support and encouragement from many people.

I am deeply grateful for my supervisor professor Goro Fujita for inspiration and support. I have learnt and improved many skills from my supervisor. Especially, the way he works and helps students has greatly influenced me. This experience would help me become a good teacher and researcher in my future career.

I would also like to thank professors in my defence committee: Prof. Matsumoto, Prof. Takami, Prof. Akatsu and Prof. Iba for their comments and assessment. Their knowledge and experience are very valuable for me to improve my thesis.

My thanks goes to many friends in my lab for their collaboration, assistance and communication as well. They have helped me not only in my study but also in my daily life in Japan.

I am so grateful for the scholarship from my university, Shibaura Institute of Technology, during my four years in Japan. This thesis is not possible without the scholarship.

Finally, I would like to thank my parents for their love and support. My grandparents, my aunt and many relatives also help me a lot. They have been with me in any circumstances during my life. I would also like to express my love to my honey, Oanh Nguyen. Her love and understanding are always along with me. I could never fully express my love and gratitude to them.

Dedicated to my beloved family

Abstract

Study on Stability Control and Low-Cost Structure of Power Converter for Doubly-Fed Induction Generator Wind Turbine

by

Danvu Nguyen

This thesis deals with two main topics of DFIG-based wind power system: Control and Structures. These are very fundamental yet essential for DFIG research. New approach for these aspects are proposed in this research. The nonlinear control method is proposed to stabilize the DFIG system under several scenarios, as changes of machine parameters and voltage disturbances. The proposed method can overcome the issues of a traditional PI-controller for DFIG under these case studies, as reported in simulation study.

The research also proposes a low-cost structure, in which a simplified converter is employed to replace grid-side converter of DFIG. Hence, it can decrease the cost of the conventional DFIG system. Moreover, to keep the power quality in the simplified structure, the method of Self-compensating DFIG is proposed and analyzed. The low-cost system is compared with the traditional DFIG system in detail. In addition, the new sensorless MPPT method is presented for the hybrid PV-DFIG system. The hybrid system is introduced in previous research to combine PV and DFIG and reduce the number of converters. The proposed MPPT method can also reduce the number of PV sensors. Hence, with the sensorless control, the cost of the hybrid system can become cheaper.

In the chapter on experiments, the module-based experimental systems are demonstrated. These systems are built based on respective projects in Power System Lab,

Shibaura Institute of Technology. The wind power system based on modules, which is mainly involved in this thesis, is designed and developed. In addition, a review of flicker issues and flicker mitigation methods in Wind power system is stated in this thesis. It provides fundamental understanding on the state of the art in mitigation methods.

Contents

List of Figures

List of Tables

List of Abbreviations

Chapter 1

WT	Wind Turbine
DFIG	Doubly-Fed Induction Generator
VOC	Vector-Oriented Control
DPC	Direct Power Control
LVRT	Low Voltage Ride Through
PV	Photovoltaic
GSC	Grid-Side Converter
SC-DFIG	Self-Compensating DFIG
MPPT	Maximum Power Point Pranking

Chapter 2

FSWT	Fixed-Speed Wind Turbine
VSWT	Variable-Speed Wind Turbine
SG	Synchronous Generators
GE	General Electric

Chapter 3

RSC	Rotor-Side Converter
DC-Link	Direct Current Link

Chapter 4

PCC	Point of Common Coupling
6DR	6-Diode Sectifier
SSR	Single-Switch Sectifier
B2B	Back-to-Back
THD	Total Harmonic Distortion

Chapter 5

BB	Buck-Boost
P&O	Perturbation and Observation

Chapter 6

EPRI	Electric Power Research Institute
STATCOM	Static Compensator

Chapter 7

DG	Distributed Generation
IM-SG	Induction Motor and Synchronous Generator
PBL	Project-Based Learning
GOV	Speed Governor
AVR	Automatic Voltage Regulator
WECS	Wind Energy Conversion Systems
DLL	Data Logger Light

List of Symbols

Chapter 2

k	Shape parameter
c	Scale parameter
ω	Wind speed
$\Gamma(z)$	Euler's gamma function
$S(f)$	Complex cross spectral matrix
$S_{rc}(f)$	Cross power spectrum
$\gamma()$	Coherence function
d_{rc}	Distance between two turbines
V_0	Mean wind speed
τ_{rc}	Delay time
u^*	friction velocity
z	hub height
V_H	hub-height wind speed
r	radial distance
W_s	wind shear shape function
α	empirical wind shear exponent
P_v	wind power

V_v	wind speed
A	crossing surface
ρ	air density
C_p	power coefficient
λ	tip speed ratio
R	radius of blades
Ω_t	angular speed of the rotor
C_t	Torque coefficient
$\overrightarrow{v}_s$	Stator voltage
$\overrightarrow{i}_s$	Stator current
$\overrightarrow{\psi}_s$	Stator flux
$\overrightarrow{v}_r$	Rotor voltage
$\overrightarrow{i}_r$	Rotor current
$\overrightarrow{\psi}_r$	Rotor flux
R_s	Stator resistance
R_r	Rotor resistance
L_s	Stator inductance
L_r	Rotor inductance
L_m	Magnetizing inductance
$L_{\sigma s}$	Stator leakage inductance
$L_{\sigma r}$	Rotor leakage inductance
P_s	Stator active power
P_r	Rotor active power
Q_s	Stator reactive power
Q_r	Rotor reactive power
T_{em}	Electromagnetic torque

Chapter 3

v_{dqs}	Stator voltage in dq-axis
i_{dqs}	Stator current in dq-axis
v_{dqr}	Rotor voltage in dq-axis
i_{dqr}	Rotor current in dq-axis
$\varepsilon_d q$	Error of rotor current in dq-axis
δ_d	Hysteresis band
h_{dq}	Output of hysteresis block
$\vec{e_r^r}$	Electromagnetic force on rotor side
$\left\|\hat{E}_r\right\|$	Amplitude of emf on rotor side
$\vec{\psi}_{sf}$	Forced flux
$\vec{\psi}_{sn}$	Natural flux
s	slip value

Chapter 4

$v_{\alpha\beta}$	Instantaneous voltage in $\alpha\beta$-axis
$i_{\alpha\beta}$	Instantaneous current in $\alpha\beta$-axis
p	Instantaneous real power
q	Instantaneous imaginary power
$\bar{p}, \bar{q}$	Average terms of p, q
$\tilde{p}, \tilde{q}$	Oscillating terms of p, q

Chapter 5

I_{pv}	PV current
V_{pv}	PV voltage
I_D	Diode saturation current
q	Electron charge
A	Material factor of diode
K	Boltzmann constant
R_S	Series resistor
T	Absolute temperature
P_{GSC}	GSC power
P_{RSC}	RSC power
P_{PV}	PV power
i_{RSC}	Dummy current for estimation
s_{abc}	Switching values of phase a, b and c

Chapter 6

V_{1pk}	Minimum positive peak of voltage
V_{2pk}	Maximum positive peak of voltage
W	weighted average flicker level
P_{st}	short-term flicker severity
P_k	flicker levels exceed for k% of observation time
ΔV	change in voltage
X	line reactance
R	line resistance

Chapter 1

Introduction

1.1 Overview of DFIG Research

Nowadays, wind energy has emerged as the most important renewable source compared to others like solar, fuel cell etc. Around 45 GW of new wind power are globally installed in 2012 [1]. Among current topologies, Doubly Fed Induction Generators (DFIGs) have been the most popularly used for variable-speed wind power systems [2]. Variable speed operation and bidirectional power control are advantageous capabilities of this configuration. Furthermore, DFIGs power converter is rated for approximately 20-30% of its rating [3–5]. These advantages make DFIG-study a highly-concerned topic in renewable energy during the past decades.

There are 2 fundamental control methods of DFIG: Vector-oriented control (VOC) and Direct power control (DPC). The VOC can regulate the powers of DFIG using reference frame transformations of control variables [6–8]. On the other hand, the DPC can choose the control vector by monitoring a stator flux directly [9–11]. Many advanced control methods are also proposed to improve traditional ones. For example, applications of predictive control, fuzzy model and neural network on DFIG

controllers are investigated in current research [12–14].

Operations of DFIG under disturbances are considered notably. In the past, a system of crowbar was used to disconnect power converters on the rotor side of DFIG to protect the whole system [15]. However, because of recent grid codes, wind power system must keep connected to the grid and inject the reactive power to support the grid during voltage dips. Therefore, studies on low voltage ride through (LVRT) method for DFIG systems are proposed and analyzed [36, 38]. With the capability of LVRT, the DFIG system can efficiently support the grid under disturbances [16].

Other researchers focus on new structures for DFIG systems. Traditionally, back-to-back converter is applied to control DFIG [3]. In order to improve the control quality, multi-level converters are proposed for DFIG systems [17, 18]. Because multi-level converters can increase the size and cost of the system, some researchers employ a matrix converter to control the DFIG [19]. The matrix converter can reduce the size of the converter due to elimination of capacitors. Simplified and low-cost structures are also proposed for DFIG systems [20, 21].

Study of DFIG integration into various systems is very promising. A battery storage system can stabilize the DFIG system [22], and combination with photovoltaic (PV) system can boost the development of renewable energy [56]. Besides, cooperation of hydropower plant and DFIG systems is proposed and investigated [58].

On the other hand, the intermittence of wind power source can strongly affect the output power of DFIG. It can cause oscillations of power and voltages. Therefore, research on these issues is very necessary. Power-smoothing control methods for DFIG are proposed using inertia energy [23]. The voltage stability methods for DFIG are considered in literature [76, 77].

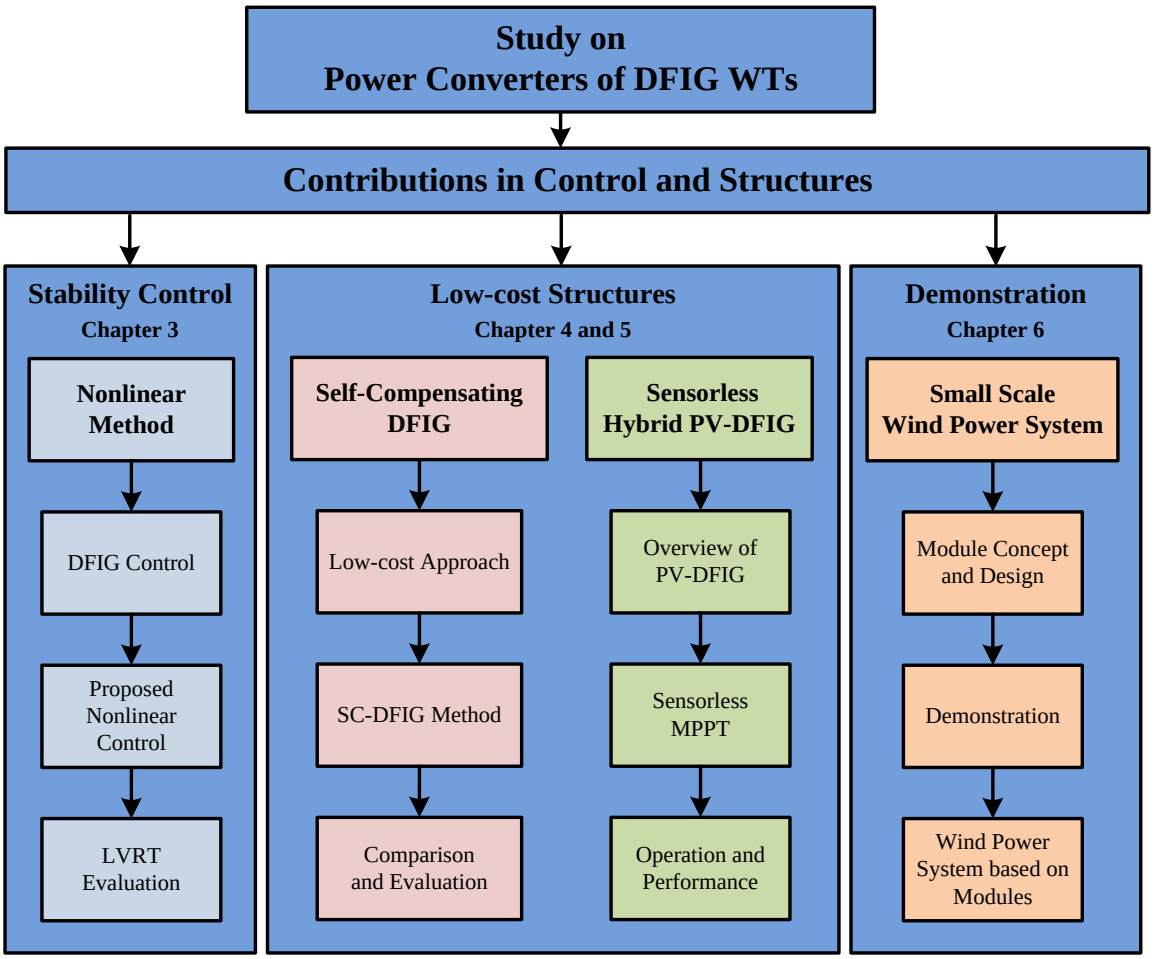

Figure 1.1: Structure of research in the thesis

1.2 Study and Contributions in this Thesis

This thesis deals with several topics of Power Converters in a DFIG system: Stability Control and Low-cost Structure. They are fundamental yet important aspects of DFIG power converter research in the literature. The entire structure of research in the thesis is illustrated in Fig. 1.1 in detail. From the chapter 3, every chapter proposes and analyzes a new approach of DFIG power converter research, namely Nonlinear method for Stability control in chapter 3, Self-compensating DFIG and Sensorless hybrid PV-DFIG for Low-cost structures in chapter 4 and 5 respectively.

In addition, Chapter 6 introduces the module-based system and the on-going development of Wind Power System. The contributions in every chapters are stated in detail in the following.

Chapter 3: A new nonlinear control approach for DFIG power converter is proposed to enhance stability of system under operations. The proposed method can overcome issues due to errors of machine parameters, which strongly impact traditional PI methods. The low voltage ride-through (LVRT)capability of this control method is also validated in the simulation study. With this capability, it can improve stability of DFIG WTs during voltage dips.

Chapter 4: This chapter proposes and analyzes the low-cost structures of DFIG power converter. In this structures, simplified converters are used to replace the conventional grid-side converter (GSC) of DFIG. Therefore, it can reduce the cost of the traditional structure due to the low-cost converters and elimination of associated circuits of GSC. In addition, to apply the simplified structure, a concept of Self-Compensating DFIG (SC-DFIG) is introduced. The method of SC-DFIG controls the DFIG to compensate distorted currents which injected by the simplified structure to the grid. So it can maintain the power quality of the low-cost DFIG system. The results of SC-DFIG system are analyzed, and the comparisons between the low-cost structures and the traditional structure using back-to-back converter are demonstrated in simulation study.

Chapter 5: A sensorless maximum power point tranking (MPPT) method for hybrid Photovoltaic-Wind system is presented in this chapter. This hybrid system is previously considered to reduce the cost of the two separate systems of PV and DFIG in literature, which is reviewed in the chapter as well. The new sensorless method can track the maximum power of PV system without the PV current sensor. The main idea of the method is to use the sensors of DFIG power

converters to estimate the output power of PV. Consequently, it can efficiently decrease the cost of the hybrid system. The new method's results are reported, and coordinating operations of the entire system are also analyzed.

Chapter 6: This chapter introduces module-based experimental systems in Power System Lab, Shibaura Institute of Technology. Concepts, design and developments of these systems are presented in detail. Three projects based on modules are demonstrated, namely Transmission system, Hydropower system and Grid-connected inverter system. In addition, the ongoing development of Wind power system based on modules is explained. The system is a fundamental model for several further study on Wind power system in future.

In addition, flicker mitigation is a very important topic in DFIG WTs. Previous research on flicker mitigation of WECS is summarized in Appendix A. Many methods of mitigation are outlined and explained in details. Moreover, important points of flicker mitigation study are presented, such as flicker definitions, flicker meter (IEC standard), flicker causes in wind power system.

Chapter 2

Wind Energy Conversion System

2.1 Wind Statistics and Modeling

2.1.1 Weibull Distribution

Weibull distribution is very popular to express the probability density function of the wind speed. The Weibull function is derived as [24]:

$$f(\omega) = \frac{k}{c}\left(\frac{\omega}{c}\right)^{k-1} e^{-(\omega/c)^k} \tag{2.1}$$

Where k is a shape parameter, c is a scale parameter and ω is the wind speed.

The average wind speed can be obtained by the density function:

$$\bar{\omega} = \int_0^\infty \omega f(\omega) d\omega = \frac{c}{k}\Gamma(\frac{1}{k}) \tag{2.2}$$

$$\Gamma(z) = \int_0^\infty t^{z-1} e^{-t} dt \tag{2.3}$$

Where Γ is Euler's gamma function.

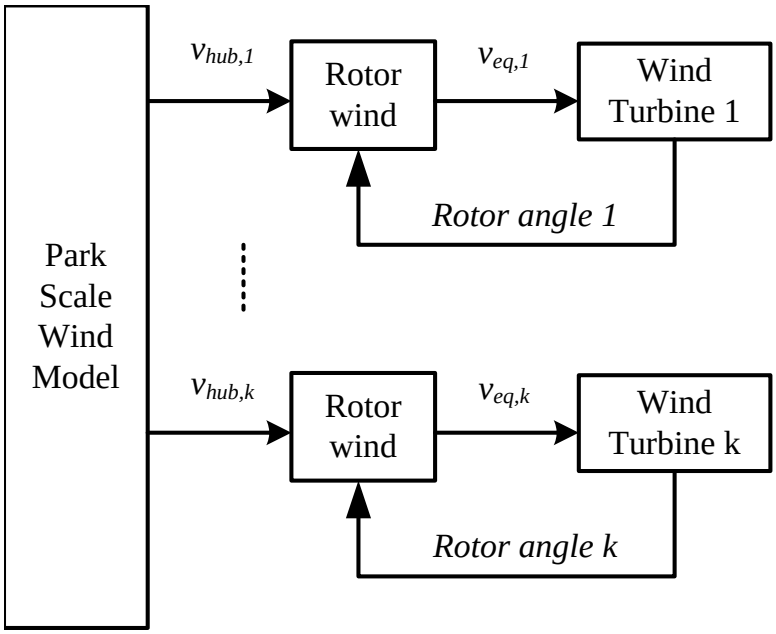

Figure 2.1: Park scale wind model

Particularly, when the shape parameter is 2, the Weibull distribution becomes the Rayleigh distribution. The scale factor of Rayleigh distribution c is calculated in respect with a given average wind speed as:

$$c = \frac{2}{\sqrt{\pi}}\bar{\omega} \tag{2.4}$$

2.1.2 Wind Model in Park Scale

A structure of wind model in park scale is demonstrated in Fig. 2.1. There are two levels in the structure: park scale level and rotor wind level [25]. At the first level, wind speeds in hub height are calculated considering coherence of turbines. The second level generates equivalent wind speeds, including effects of wind shear and tower shadow.

Complex cross spectral matrix $S(f)$ is used to calculate wind speeds of turbines

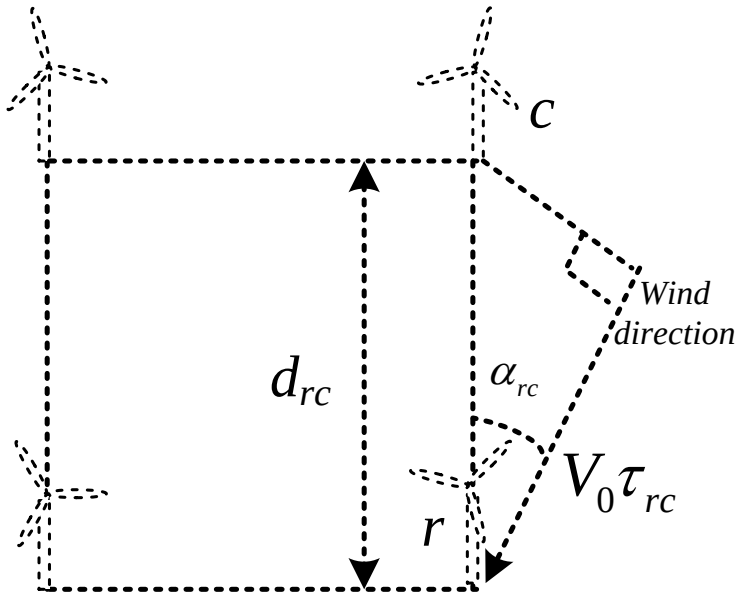

Figure 2.2: Coherence of turbines

considering turbulence coherence [25]. If a wind park has N turbines, dimension of matrix S is NxN. For example, an element $S_{rc}(f)$ is the cross power spectrum between turbulence at wind turbine number r and c. $S_{rc}(f)$ is expressed as the following:

$$S_{rc}(f) = \gamma(f, d_{rc}, V_0)\sqrt{S_{rr}(f)S_{cc}(f)}\, e^{-j2\pi f\tau_{rc}} \tag{2.5}$$

Where γ is coherence function, d_{rc} is distance between two turbines, V_0 is mean wind speed, and τ_{rc} is delay time.

Fig. 2.2 illustrates distance and delay time between turbines r and c of four turbines in a wind park. The spectrum $S_{kk}(f)$ used in this research is two-sided Kaimal spectrum:

$$S_{Kai}(f) = u_*^2 \frac{52.5(z/V0)}{(1+33(z/V0)f)^{5/3}} \tag{2.6}$$

Where u^* is friction velocity and z is hub height.

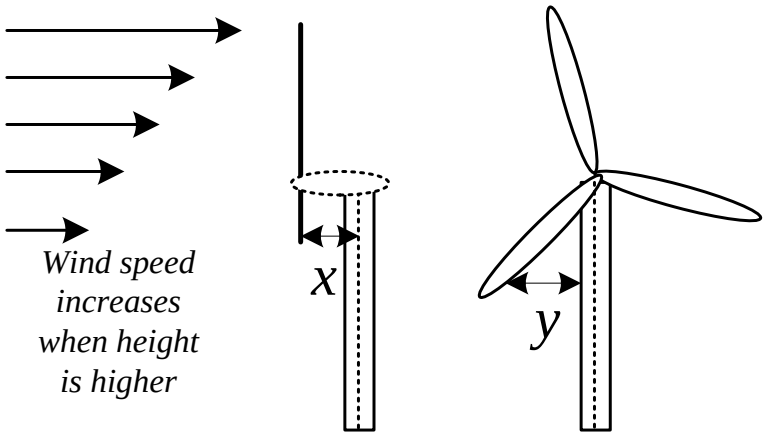

Figure 2.3: Mechanical illustration of turbines

The matrix S(f) is discretized in frequency domain to estimate Fourier coefficients of wind speed time series. These coefficients are used to perform an inverse Fourier transform to generate the hub height wind speed v_{hub} in time domain.

In rotor wind model, it is very necessary to take into account wind shear and tower shadow. The term wind shear is defined as variations of wind speed with height, whereas the term tower shadow is used to describe the redirection of wind due to the tower structure.

Wind shear, as explained in Fig. 2.3, is expressed as the function below.

$$V(r,\theta) = V_H(\frac{r\cos\theta + H}{H})^{\alpha} = V_H(1 + W_s(r,\theta)) \tag{2.7}$$

Where V_H is hub-height wind speed, r is the radial distance from rotor axis, W_s is wind shear shape function, α is the empirical wind shear exponent, H is hub height.

The wind shear function can be approximated using Taylor series expansion as follows:

$$W_s(r,\theta) \approx \alpha(\frac{r}{H})\cos\theta + \frac{\alpha(\alpha-1)}{2}(\frac{r}{H})^2\cos^2\theta \tag{2.8}$$

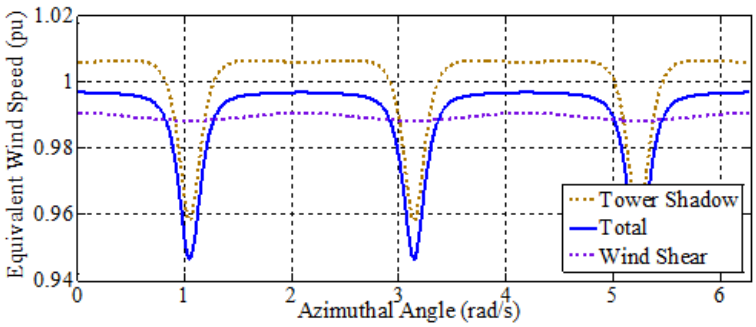

Figure 2.4: Wind shear and Tower Shadow effects

On the other hand, tower shadow effect can be calculated based on the lateral distance y and the distance x from the blade to the tower midline as shown in Fig. 2.3. Tower shadow function is determined as follows.

$$v_{tower}(y,x) = V_0 a^2 \left(\frac{y^2 - x^2}{(y^2 + x^2)^2}\right) \tag{2.9}$$

Fig. 2.4 illustrates the influence of wind shear and tower shadow on equivalent wind speed. Impact of wind shear and tower shadow on torque oscillations are also discussed in depth in [26].

2.2 Aerodynamic Power Conversion and Control

2.2.1 Aerodynamic Power from Wind

The theory of momentum is used to study the process of extracting the kinetic energy in the wind. Based on energy conservation and Bernoullis equation, the power in the form of kinetic energy is derived as [27]:

$$P_v = \frac{1}{2}\rho A V^3 \tag{2.10}$$

Where P_v is wind power, V_v is wind speed, A is crossing surface and ρ is the air

density.

The mechanical power converted by wind turbines is less than that power:

$$P_v = \frac{1}{2}\rho A V^3 C_p \tag{2.11}$$

Where C_p is the power coefficient, a transformation ratio between kinetic energy of the wind and mechanical input power.

This coefficient is a function of pitch angle and the tip speed ration. The tip speed ratio, λ, is defined by:

$$\lambda = \frac{R\Omega_t}{V_v} \tag{2.12}$$

Where R is the radius of blades and Ω_t is the angular speed of the rotor.

The maximum value of C_p is given by the Betz limit:

$$C_p max = 0.593 \tag{2.13}$$

The mechanical torque is obtained by the relationship between torque, angular speed and power:

$$T_t = \frac{P_t}{\Omega_t} = \frac{\rho\pi R^2 V_v^3}{2\Omega_t} C_p = \frac{\rho\pi R^3 V_v^2}{2\lambda} C_p = \frac{\rho\pi R^3 V_v^2}{2} C_t \tag{2.14}$$

Where C_t is the torque coefficient. The relationship between coefficients of power and torque is as follows:

$$C_p(\lambda) = \lambda C_t(\lambda) \tag{2.15}$$

As stated above, the power coefficient C_p is very important to calculate the mechanical power from the wind source. The expression C_p is dependent on character-

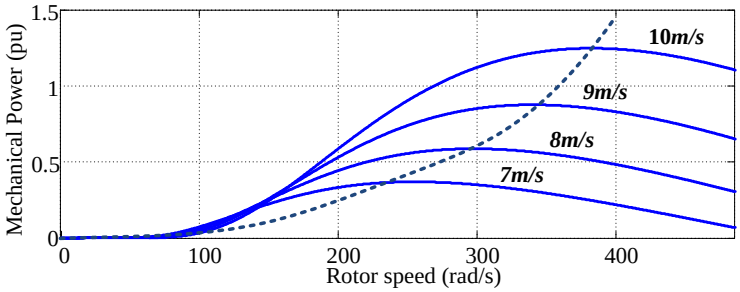

Figure 2.5: Wind characteristics

istics of blades and turbines. In practice, C_p is calculated by experimental measurements or computer-aided estimation. When the data of C_p is available, approximate functions are derived by using interpolation and polynomial regression.

In this thesis, two analytical expressions of C_p, which are popular in wind energy research, are introduced. The first expression is used in [5]:

$$C_p = k_1(\frac{k_2}{\lambda_i} - k_3\beta - k_4\beta^{k_5} - k_6) \times e^{k_7/\lambda_i} \tag{2.16}$$

$$\lambda_i = \frac{1}{\lambda + k_8} \tag{2.17}$$

The second expression, which is simpler, is applied in [28]:

$$C_p = \frac{1}{2}(\gamma - 5.6) \times e^{-0.17\gamma} \tag{2.18}$$

$$\gamma = \frac{V_v(mi/h)}{\omega_r(rad/s)} \tag{2.19}$$

The characteristics of second expression is shown in Fig. 2.5. This expression with the assumption of constant pitch angle is used in other chapters of this thesis.

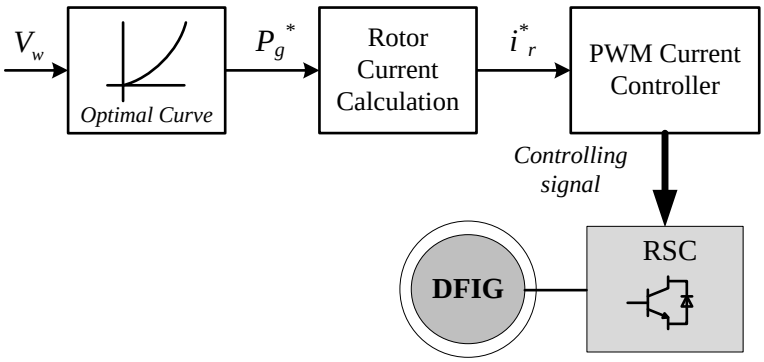

Figure 2.6: Optimal control diagram

2.2.2 Optimal Power Control

The optimal mechanical power can be obtained from the wind energy when the power coefficient comes maximal, as illustrated in Fig. 2.5. In this research, the optimal control method in [29] is adapted. Moreover, to make it simpler, the wind speed value is used in this research. The control diagram is illustrated in Fig. 2.6.

2.3 Wind System Topologies

Based on speed range of operation, there are two types of wind turbines: Fixed-speed and Variable-speed. Generators of FSWT are connected to the grid directly. Therefore, the speed, which is similar to the grid frequency, are not controllable and the wind variations will affect the power quality of the grid. On the other hand, VSWTs are equipped by power electronics converters. The converters can control the rotor speed and stabilize the wind power fluctuations. Therefore, the VSWTs can strongly improve the power quality compared to the FSWTs.

Three structures of wind turbines, which have been used popularly, are presented in this section:

1. Fixed-speed wind turbine with an induction generator

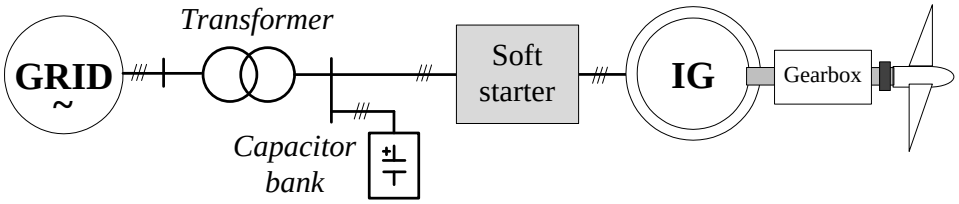

Figure 2.7: Diagram of Fixed-speed WT

2. Variable-speed wind turbine with synchronous generator
3. Variable-speed wind turbine with doubly-fed induction generator

2.3.1 Fixed-speed wind turbines

A structure of Fixed-speed wind turbines is illustrated in Fig. 2.7. The generator output is directly connected to the power grid. The rotor speed of this structure is handled by a gearbox. Because of lacks of power electronics interface and controller, reactive power is uncontrollable in this structure. FSWTs are main topology in the early stage of wind technology, but considered outdated today.

2.3.2 Variable-speed wind turbines with SG

In Variable-speed wind turbines, a power electronic converter is used to convert the generator power into usable power for transmission and distribution, as shown in Fig. 2.8. Synchronous generators, which can be winding rotor or permanent-magnet rotor, are mainly used in this structure. The power converter consists of AC/DC converter and DC/AC converter. These converters are commonly used and developed in many applications for energy conversion. Because of power electronic interface, this structure can control the active power and reactive power independently.

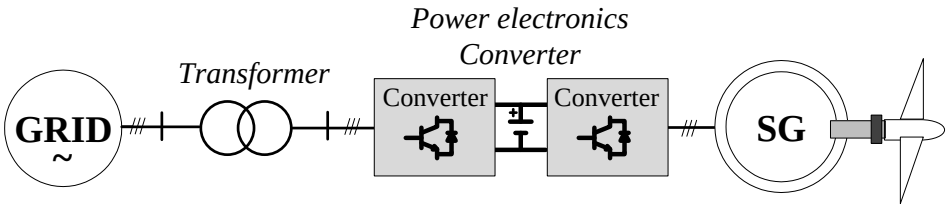

Figure 2.8: Diagram of Variable-speed WT using SG

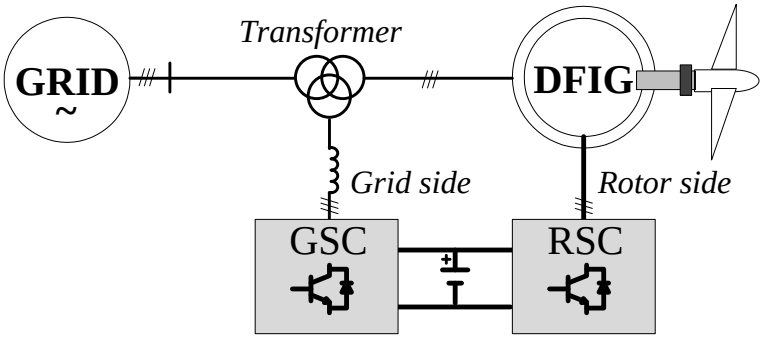

Figure 2.9: Diagram of Variable-speed WT using DFIG

2.3.3 Variable-speed wind turbines with DFIG

Fig. 2.9 demonstrates the variable-speed wind turbine based on DFIG. In this structure, the generator output is also directly connected to the grid power. In addition, the rotor of the generator is connected to the back-to-back converter. This full-quadrant converter can convert the power between the rotor and the grid bi-directionally [3].

Recently, this system has become popularly used generators for variable-speed wind turbines. There are two main advantages in this system. First, the range of operation speed is very broad from 30% under synchronous speed to 30% over synchronous speed. Second, the rating of power converter is very small compared to other systems. Because the converter handles only the rotor power, the rating is around $25 \sim 30\%$ of the generator rating.

2.4 Fundamental of DFIG

2.4.1 Equivalent circuits of DFIG

The differential equations representing the model of the DFIG are derived, using the space vector notation in the stationary (stator) reference frame, in this section. In space vector form, the relation of voltages, currents and fluxes are simply stated [5]:

$$\begin{aligned} \overrightarrow{v}_s &= R_s.\overrightarrow{i}_s + \frac{d}{dt}\overrightarrow{\psi}_s \\ \overrightarrow{v}_r &= R_r.\overrightarrow{i}_r + \frac{d}{dt}\overrightarrow{\psi}_r \end{aligned} \tag{2.20}$$

Where: $\overrightarrow{v}$, $\overrightarrow{i}$, $\overrightarrow{\psi}$ and R are voltage, current, flux and resistor respectively, subscript: s, r are stator and rotor.

In addition, the correlation between the fluxes and the currents, in space vector notation, is given by:

$$\begin{aligned} \overrightarrow{\psi}_s &= L_s\overrightarrow{i}_s + L_m\overrightarrow{i}_r \\ \overrightarrow{\psi}_r &= L_m\overrightarrow{i}_s + L_r\overrightarrow{i}_r \end{aligned} \tag{2.21}$$

Where L_s and L_r are the stator and rotor inductances, L_m is the magnetizing inductance, and they are related to the stator leakage inductance $L_{\sigma s}$ and the rotor leakage inductance $L_{\sigma r}$, according to the following expressions:

$$\begin{aligned} L_s &= L_{\sigma s} + L_m \\ L_r &= L_{\sigma r} + L_m \end{aligned} \tag{2.22}$$

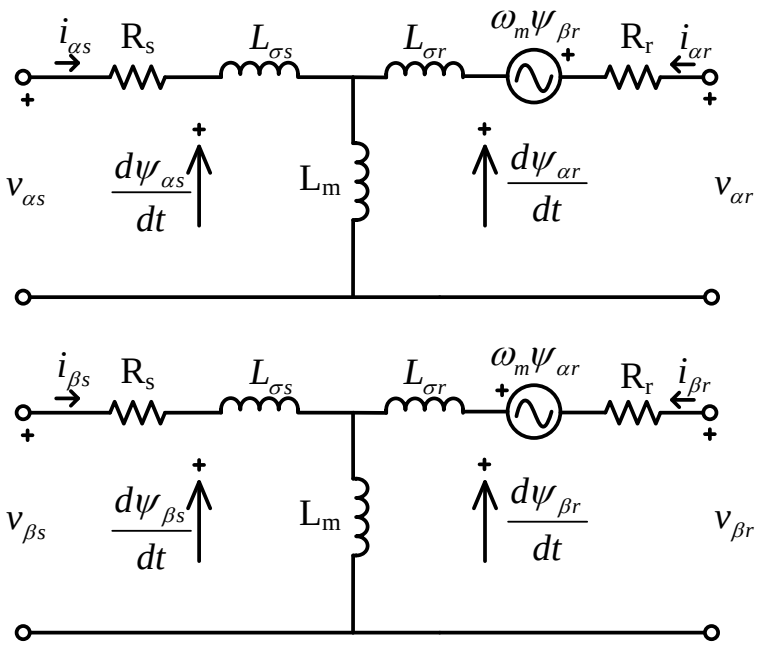

Figure 2.10: Equivalent circuits of DFIG model

All the equations above can be demonstrated in terms of equivalent circuits, as seen in Fig. 2.10.

Continuing with the model, the electric powers on the stator side and on the rotor side are calculated as follows:

$$\begin{aligned} P_s &= \frac{3}{2}\,\mathrm{Re}\left\{\overrightarrow{v_s}\cdot\overrightarrow{i_s^*}\right\} = \frac{3}{2}(v_{\alpha s}i_{\alpha s} + v_{\beta s}i_{\beta s}) \\ P_r &= \frac{3}{2}\,\mathrm{Re}\left\{\overrightarrow{v_r}\cdot\overrightarrow{i_r^*}\right\} = \frac{3}{2}(v_{\alpha r}i_{\alpha r} + v_{\beta r}i_{\beta r}) \\ Q_s &= \frac{3}{2}\,\mathrm{Im}\left\{\overrightarrow{v_s}\cdot\overrightarrow{i_s^*}\right\} = \frac{3}{2}(v_{\beta s}i_{\alpha s} - v_{\alpha s}i_{\beta s}) \\ Q_r &= \frac{3}{2}\,\mathrm{Im}\left\{\overrightarrow{v_r}\cdot\overrightarrow{i_r^*}\right\} = \frac{3}{2}(v_{\beta r}i_{\alpha r} - v_{\alpha r}i_{\beta r}) \end{aligned} \tag{2.23}$$

Where the superscript $*$ represents the complex conjugate of a space vector as was used in terms of phasors. Moreover, the electromagnetic torque can be found from:

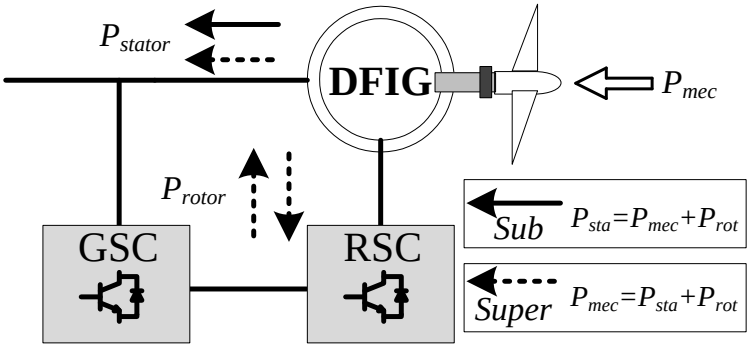

Figure 2.11: Power flow

$$T_{em} = \frac{3}{2} p \,\mathrm{Im}\left\{\overrightarrow{\psi_r} \cdot \overrightarrow{i_r^*}\right\} = \frac{3}{2} p(\psi_{\beta r} i_{\alpha r} - \psi_{\alpha r} i_{\beta r}) \tag{2.24}$$

2.4.2 Operation Modes of DFIG

One of advantages of DFIG wind turbines is long-range variable-speed operation, about $\pm 30\%$ of synchronous speed. Directions of mechanical and electrical powers of DFIG are alternative under variable-speed operations. Based on power flow, DFIG operations can be divided into 2 modes. In fact, DFIG can run under 4 different modes, 2 modes for generator and 2 modes for motor. However, in the research of this thesis, only 2 modes of generator are considered and analyzed.

Two modes of DFIG, namely supersynchronous mode and subsynchronous mode, are dependent on wind speed. When the wind speed is higher than the synchronous speed, the generator operates in supersynchronous mode. Otherwise, the generator operates in subsynchronous mode. The power flow of two modes is illustrated in Fig. 2.11.

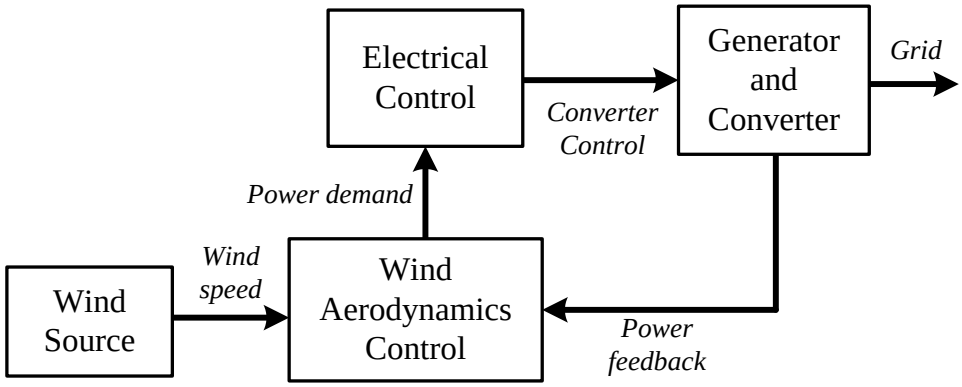

Figure 2.12: Diagram of Studied System in the Thesis

2.5 Modeling and Assumptions of Studied System

In previous section, the equivalent circuits and property of DFIG are explained in detail. A wind power system consists of not only the generator but also other mechanical and electrical parts. Descriptions of these parts in this thesis are presented in this section.

2.5.1 Dynamic Modeling and Assumptions

Dynamic modeling of the entire wind power system in this thesis is based on the report documents from General Electric (GE) - Power Systems Energy Consulting [30]. This document is suitable for analysis of WTs in cases of grid disturbances, faults. Moreover, the influence of wind speed fluctuation is also taken into accounts in this model.

The rating power of DFIG is modified and different from the report document. The document recommends two kinds of machines. The GE 1.5 and GE 3.6 machines have rated power outputs of 1.5MW and 3.6MW respectively. They are also connected to the bus of 575V and 4160V respectively. The DFIG rating in the thesis is modified based on other common research with 1MW power output and the bus of 670V [77,78].

The dynamic modeling of the studied system is illustrated in Fig. 2.12. There are four main model blocks in this system, namely Generator-Converter, Electrical Control, Wind Aerodynamic Control and Wind Source. They are described as follows:

Generator-Converter: DFIG is the main generator in this thesis. Basically, a structure of DFIG is a wound-rotor machine, which has the stator connected to the grid and the rotor connected to the power converter. Mathematical model of DFIG is presented in previous section. This model is fundamental and commonly-used for research of DFIG [5]. Back-to-back converter is employed to regulate output power of DFIG WTs. The 2-level converter (6 switches) is used for both grid-side and rotor-side converters. In addition, other structures in several chapters are explained in detail for specific research.

Electrical Control: Power control methods for DFIG are very important in this thesis. Typically, a controller is used to stabilize the output power of DFIG under various operation. There are several main control methods, which will be explained in Chapter 3. The control diagrams of the methods are also stated in that chapter. In some parts of the thesis, the influence of inertia is considered small enough during short-time validation of electrical control method. This assumption is common in research of electrical control for DFIG [10].

Wind Aerodynamic Control: The control model in this block is demonstrated in section 2.2 "Aerodynamic Power Conversion and Control". The main function is for optimal control according to wind characteristics. In this thesis, the pitch control is not taken into account, and the pitch angle is considered constant in power coefficient formula. The wind characteristic curve in the thesis is based on [5, 28, 29].

Wind Source: There are three conventional ways to simulate wind sources: Distri-

bution function, Park-scale model and Practical data. Park-scale model of wind is very necessary to analyze the flicker influence of WTs. The model in [25, 26] is adapted in this thesis.

2.5.2 Other Practical Aspects

Switching frequency is very important in controller of power converters. Very high switching frequency can become impractical, and low value can make poor quality of currents. In this thesis, the switching frequencies of GSC and RSC are 5kHz and 2kHz respectively. These values are popularly used in research of DFIG power converters [9–11]. In addition, hysteresis band, which is used in some chapters, is modified around 1% to 2%. They are based on the reliable range from 0.5% to 4%, which are used in [31] and [10] respectively.

Influence of parameter nonlinearity is considered in the simulation system, especially in Chapter 3. In chapter 3, a stability control method is proposed and analyzed. Therefore, the change of rotor resistance is taken into account. The proposed controller is tested during this change. The variation of rotor resistance is investigated for a new controller of DFIG in [10]. On the other hand, the change of magnetizing inductance L_m is not considered in this thesis. The magnetizing inductance can be affected in case of magnetic saturation. Nevertheless, saturation effect of DFIG is not in the topic of this thesis. The entire system is operated under rating power of DFIG. Moreover, saturation of WTs, which is not included in GE's dynamic model, is required a complicated mathematical model to analyze.

Chapter 3

Nonlinear Control of DFIG for Stability Enhancement

3.1 Introduction

Operation of DFIG WTs is very important under various situations. Power converters of DFIG play a key role to regulate the output powers of DFIG WTs. Therefore, stability control of power converters is a highly-concerned topic in DFIG research. In this chapter, a nonlinear method is proposed to enhance the stability of DFIG operation. The proposed control method can overcome issues of traditional controller, which are explained in next sections. Moreover, the proposed method is tested under severe case of voltage drops. According to simulation results, the operation of nonlinear control is better than the traditional control for Low Voltage Ride Through (LVRT).

3.2 Control Methods of DFIG

3.2.1 Vector Oriented Control

Under stator flux orientation, the relationship between the current and the fluxes can be written as [5]:

$$\begin{aligned} i_{ds}L_s + i_{dr}L_m &= \psi_s \\ i_{qs}L_s + i_{qr}L_m &= 0 \end{aligned} \tag{3.1}$$

The above equations can be stated in another way:

$$\begin{aligned} i_{ds} &= \frac{\psi_s}{L_s} - \frac{L_m}{L_s} i_{dr} \\ i_{qs} &= -\frac{L_m}{L_s} i_{qr} \end{aligned} \tag{3.2}$$

The stator resistance is much smaller than the stator inductance, so it is possible to remove the stator resistor in the stator voltage equation:

$$\begin{aligned} v_{ds} &= 0 \\ v_{qs} &= \hat{V}_g \approx \omega_s \psi_s \end{aligned} \tag{3.3}$$

Combining these above equations with the power equations:

$$\begin{aligned} P_s &= \frac{3}{2} v_{qs} i_{qs} \\ Q_s &= \frac{3}{2} v_{qs} i_{ds} \end{aligned} \tag{3.4}$$

$$\begin{aligned} P_s &= -\frac{3}{2}\hat{V}_g \frac{L_m}{L_s} i_{qr} \\ Q_s &= \frac{3}{2}\hat{V}_g \frac{\psi_s}{L_s} - \frac{3}{2}\hat{V}_g \frac{L_m}{L_s} i_{dr} = \frac{3}{2}\frac{\hat{V}_g^2}{\omega_s L_s} - \frac{3}{2}\hat{V}_g \frac{L_m}{L_s} i_{dr} \end{aligned} \tag{3.5}$$

The equation 3.5 clearly showed that dq components of rotor current can be used

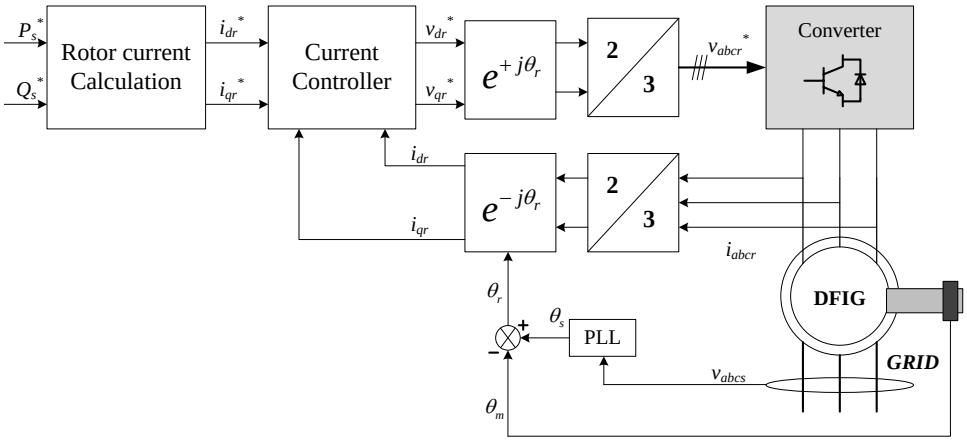

Figure 3.1: Vector control diagram

to control the stator power in the stator flux orientation. Power control scheme is demonstrated in Fig. 3.1. The block *Rotor current calculation* is based on eq. 3.5

3.2.2 Direct Power Control

The stator active and reactive power can be controlled via stator voltages and currents as equations in above subsection. In addition, they can be expressed in terms of stator and rotor fluxes [5]:

$$\begin{aligned} P_s &= \frac{3}{2}\frac{L_m}{\sigma L_s L_r}\omega_s \left|\vec{\psi}_s\right| \left|\vec{\psi}_r\right| \sin\delta \\ Q_s &= \frac{3}{2}\frac{\omega_s}{\sigma L_s} \left|\vec{\psi}_s\right| \left[\frac{L_m}{L_r}\left|\vec{\psi}_s\right| - \left|\vec{\psi}_r\right| \cos\delta\right] \end{aligned} \tag{3.6}$$

The above expressions show that the stator active and reactive powers are controllable by modifying the relative angle between the rotor and stator flux space vectors and their amplitudes. If the stator voltage is fixed, these equations will become

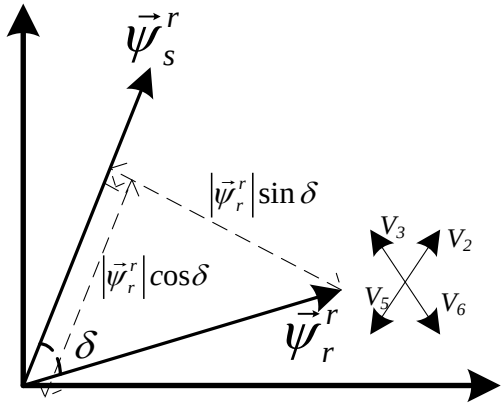

Figure 3.2: Flux diagram

simpler:

$$\begin{aligned} P_s &= K_1 \left|\vec{\psi}_r\right| \sin\delta \\ Q_s &= K_2 \left[K_3 - \left|\vec{\psi}_r\right| \cos\delta\right] \end{aligned} \tag{3.7}$$

And because the rotor flux can be controlled via the rotor voltage:

$$\begin{aligned} \vec{v}_r^r &\cong \frac{d\vec{\psi}_r^r}{dt} \\ \left|\vec{\psi}_r^r\right|_{fin} &\cong \left|\vec{\psi}_r^r\right|_{ini} + \int_0^h \vec{v}_r^r dt \\ \left|\vec{\psi}_r^r\right|_{fin} &\cong \left|\vec{\psi}_r^r\right|_{ini} + \vec{v}_r^r h \end{aligned} \tag{3.8}$$

Therefore, six space vectors of rotor voltages are employed to steer the rotor flux into an appropriate trajectory, as illustrated in Fig. 3.2.

The controlling scheme of direct power control includes hysteresis blocks and vector selection table to choose suitable voltages based on the errors of powers values, as seen in Fig. 3.3.

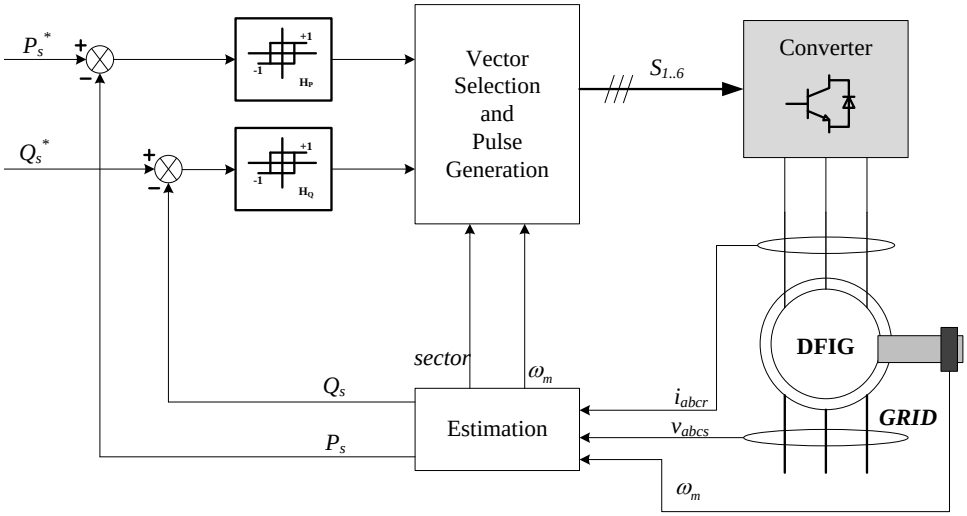

Figure 3.3: Direct power control

3.3 Nonlinear Control with dq-Hys

3.3.1 PI Control Design for DFIG

The relation between rotor quantities and stator flux is as follows:

$$\begin{aligned} v_{dr} &= R_r i_{dr} - \omega_r \sigma L_r i_{qr} + \sigma L_r \frac{d}{dt} i_{dr} + \frac{L_m}{L_s} \frac{d}{dt} \psi_{ds} \\ v_{qr} &= R_r i_{qr} + \omega_r \sigma L_r i_{dr} + \sigma L_r \frac{d}{dt} i_{qr} + \omega_r \frac{L_m}{L_s} \psi_{ds} \end{aligned} \tag{3.9}$$

This relation can be shown in the block diagram of Fig. 3.4.

The term $\omega_r \frac{L_m}{L_s} \psi_{ds}$ is considered as a disturbance when this block diagram is used to design a PI controller for DFIG. Therefore, if it is constant, the controller can compensate this component with ease. Otherwise, it can cause negative effects during transient periods.

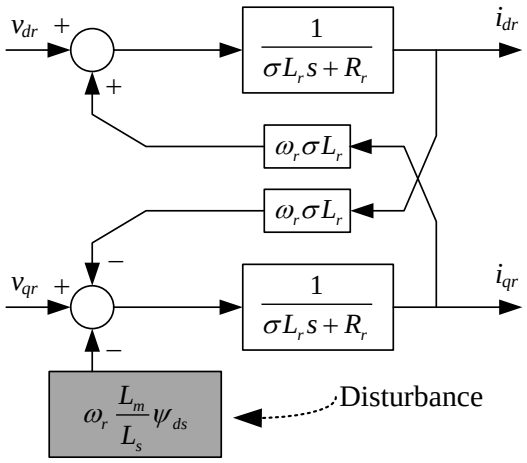

Figure 3.4: Plant of current control loop

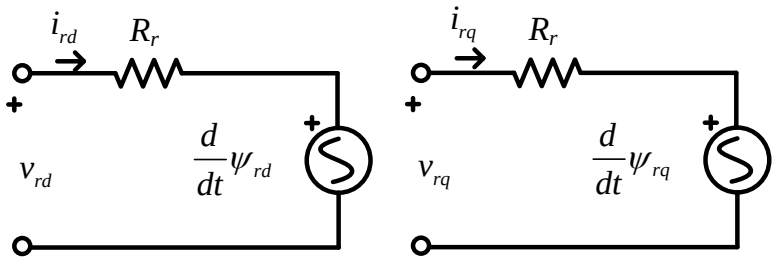

Figure 3.5: Equivalent circuits of rotor equations

3.3.2 Proposed Method

In this section, the hysteresis current controller for dq-components of the rotor currents is explained. Originally, the idea of this algorithm is proposed for induction motor control by Rodriguez *et al.* in [32]. In this research, the principle is established and employed for rotor side converter, which is 2-level inverter, of DFIG.

The equation of rotor variables is presented in eq. 2.20. From this space vector equation, dq components, in the rotor reference frame, can be expressed in eq. 3.10 and illustrated in terms of two equivalent circuits, as seen in Fig. 3.5.

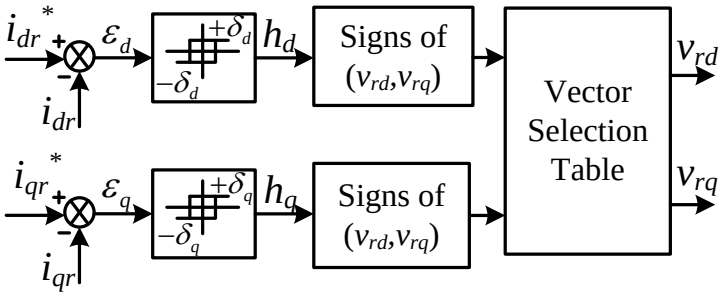

Figure 3.6: Control principle for dq-components

$$\begin{aligned} v_{rd} &= R_r.i_{rd} + \frac{d}{dt}\psi_{rd} \\ v_{rq} &= R_r.i_{rq} + \frac{d}{dt}\psi_{rq} \end{aligned} \tag{3.10}$$

The above equivalent circuits show that it is possible to increase or decrease (i_{rd}, i_{rq}) of every circuits by turning on and off the two sources (v_{rd}, v_{rq}) respectively. Firstly, the errors (ε_d, ε_q) of i_{rd} and i_{rq} are compared to the hysteresis band δ_d. Secondly, the signs of v_{rd} and v_{rq} are assigned by using the output values of the hysteresis blocks. In summary, the strategy is showed as follows:

+ $\varepsilon_d > +\delta_d$ then $h_d = 1$, increasing $i_{rd} \Rightarrow v_{rd} > 0$

+ $\varepsilon_d < -\delta_d$ then $h_d = 0$, decreasing $i_{rd} \Rightarrow v_{rd} < 0$

Fig. 3.6 states the specific steps of the proposed algorithm. The identical steps are established for q-components also.

In order to turn on or off the two sources (v_{rd}, v_{rq}), the space vector of output voltage of rotor side converter is considered, reliance on the position of d-axis of rotational reference frame which is aligned with stator flux in this research. Typically, the plane of space vectors of 2-level inverter is divided into 6 sectors, as seen in Fig. 3.7. The signs of (v_{rd}, v_{rq}) and the sector of d-axis are used to select the appropriate voltage vector.

For instance, it is assumed that d-axis is in sector I, as demonstrated in Fig. 3.7.

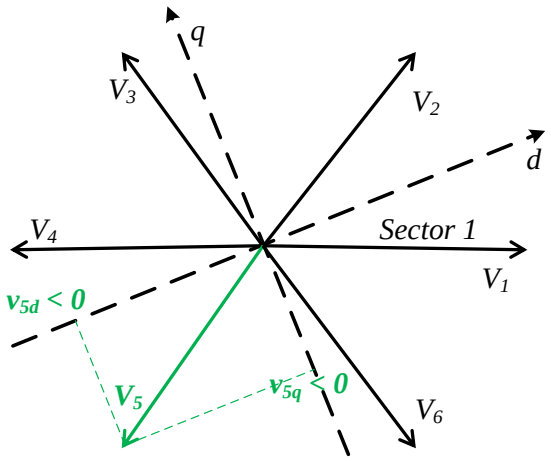

Figure 3.7: An example of vector selection

The hysteresis block outputs are $(h_d = 0, h_q = 0)$, which means decreasing (i_{rd}, i_{rq}). Therefore, the signs of the suitable voltage vectors dq-components are $(v_{rd} < 0)$ and $(v_{rq} < 0)$. V_5 is ultimately selected for accomplishing these conditions.

3.4 Simulation Study

The entire system of proposed method is implemented by using Matlab/Simulink. The simulation study is carried out to validate and analyze not only the dynamic response of the system under variations of powers, speed and machine parameter, but the ride-through capability during voltage disturbances as well. In addition, system parameters are shown in Table B.1. The sampling frequency of Simulink model is 50kHz. However, the maximum switching frequency of the proposed method is limited at 5kHz and 2kHz for GSC and RSC respectively. Also, the hysteresis band is set at 2% of the rated rotor currents.

The RSC plays a key role in this research to implement the proposed nonlinear control method. On the other hand, the GSC regulates the DC-link voltage and supplies stable powers for the RSC. The structure and control diagram of GSC are

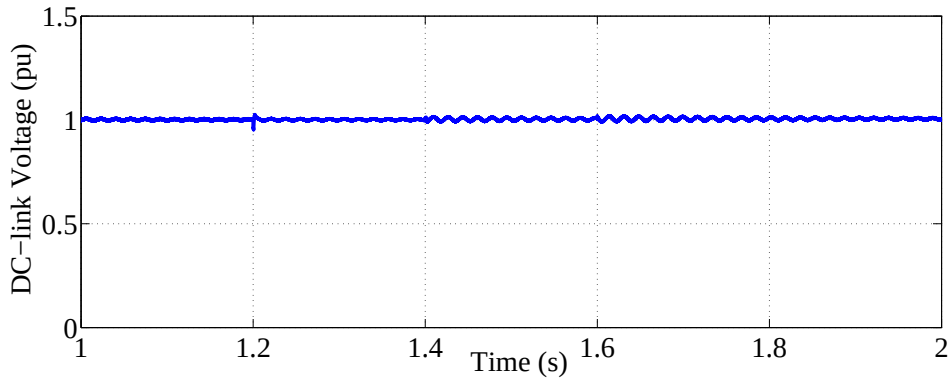

Figure 3.8: DC-link voltage

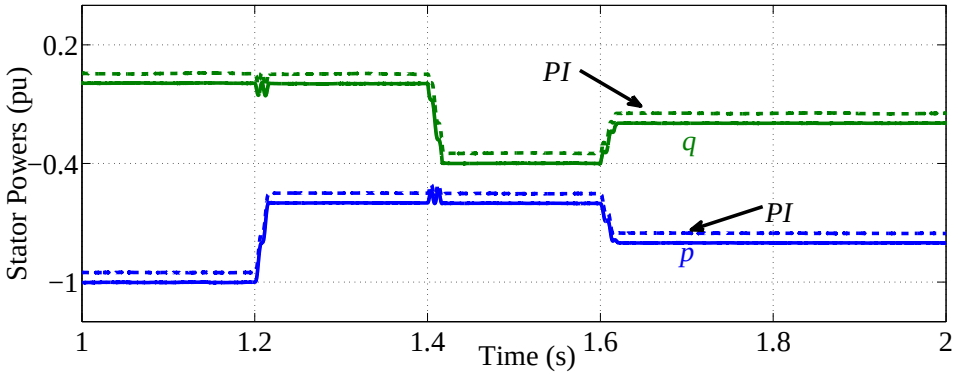

Figure 3.9: Stator powers: new method (solid) and PI (dash)

demonstrated in detail in [33]. The stator-voltage reference frame is employed in this research. In addition, the negative value of power indicates a direction of power from the generator to the grid, such as p = -1pu.

The first case study is to examine the performance of the system under step-changes of power demands. In this case study, the rotor speed is assumed constant. As seen in Fig. 3.9, the active and reactive power demands are changing from (-1pu, 0pu) into (-0.6pu, 0pu), (-0.6pu, -0.4pu) and (-0.8pu, -0.2pu) at 1.2s, 1.4s and 1.6s respectively. The responses of output powers are very quick without overshoots in both cases of the proposed controller and the PI controller.

The DC-link voltage, rotor currents, stator currents and dq-frame rotor currents

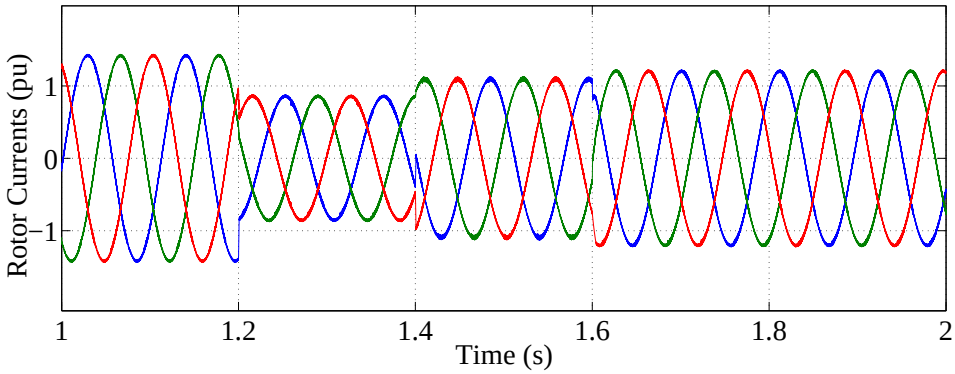

Figure 3.10: Rotor currents

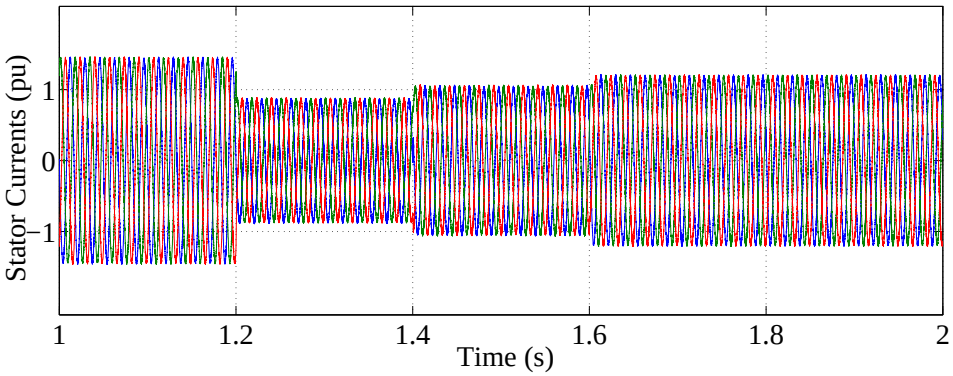

Figure 3.11: Stator currents

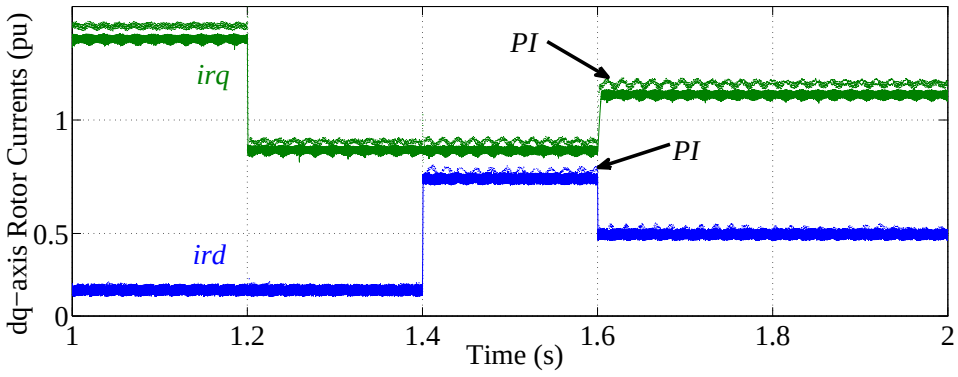

Figure 3.12: Rotor currents in dq-frame: new method (solid) and PI (dash)

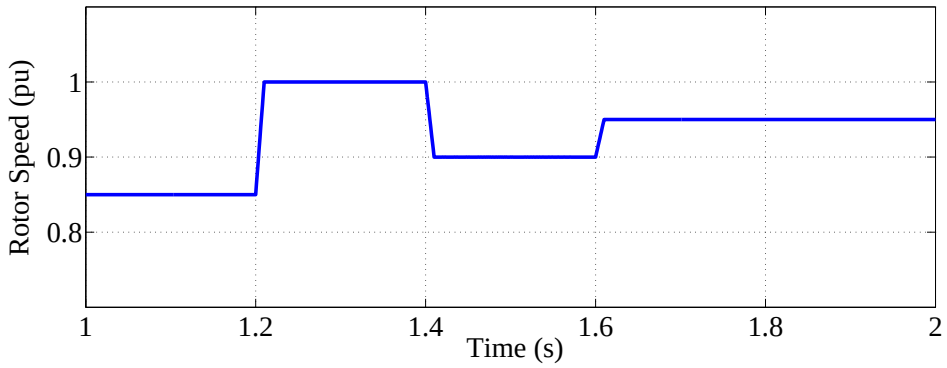

Figure 3.13: Rotor speed

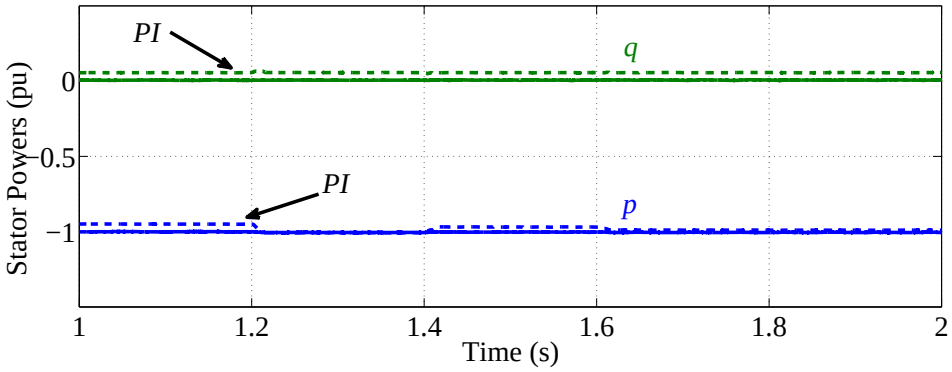

Figure 3.14: Stator Powers, 50% error of rotor resistance: new method (solid) and PI (dash)

are stated in Figs. 3.8, 3.10, 3.11 and 3.12 respectively. When the power demands change, the RSC attempts to control the rotor currents according to the relationship between stator powers and rotor currents of DFIGs. In Fig. 3.12, the responses of rotor currents are very fast. In terms of dq-frame, the rotor currents are kept constant and less oscillations than that of PI controllers.

The performance of the proposed method is evaluated in case of errors of machine parameters. In this simulation, the rotor resistance is increased 50% from the rated value. Note that the machine parameters sensitively impact the performance of a typical PI controller. The rotor speed is changed from 0.85pu to 1pu, 0.9pu and

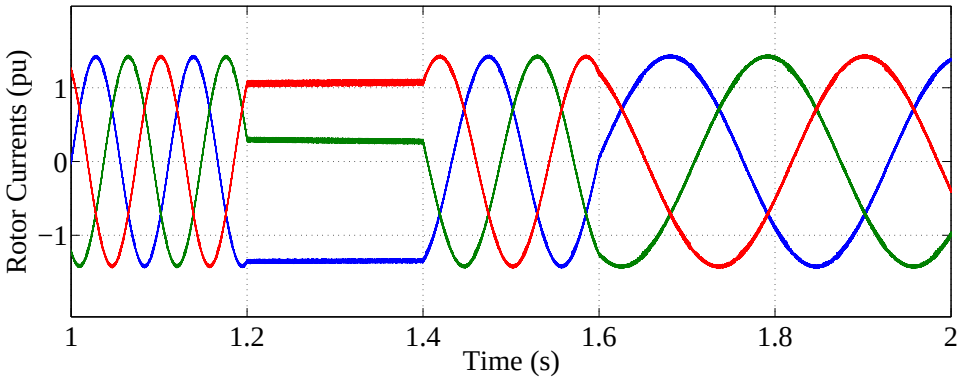

Figure 3.15: Rotor currents, 50% error of rotor resistance

0.95pu respectively. The rotor speed, stator powers and rotor currents are shown in Figs. 3.13, 3.14 and 3.15 respectively. The performance of the proposed system under machine parameter variations is very good. The results are mostly the same as those in the case of rated machine parameters. Moreover, the stator powers regulated by the PI method are not stable as shown in Fig. 3.14. The PI method cannot maintain the output powers constant under the variations of machine parameters.

3.5 LVRT under Symmetrical Dips

3.5.1 Electromagnetic Force on the Rotor Side

The electromagnetic force (emf) is one of the most important variables, since it acts as a perturbation in the control loops and it could saturate the converter. The electromagnetic force induced in the rotor windings varies considerably under grid disturbances. This is the cause of the problematic behavior of DFIGs under perturbations. The rotor voltage expression is [5]:

$$\overrightarrow{v}_r = R_r . \overrightarrow{i}_r + \frac{d}{dt} \overrightarrow{\psi}_r \tag{3.11}$$

A slight difference between rotor flux and stator flux is due to leakage inductances:

$$\vec{\psi}_r^r = \frac{L_m}{L_s}\vec{\psi}_s^r + \sigma L_r \vec{i}_r^r \tag{3.12}$$

Combining these two equations above:

$$\overrightarrow{v}_r^r = \frac{L_m}{L_s}\frac{d}{dt}\overrightarrow{\psi}_s^r + (R_r + \sigma L_r \frac{d}{dt})\overrightarrow{i}_r^r \tag{3.13}$$

The rotor voltage might be divided into two terms. The first term corresponds to the emf induced by the stator flux in the rotor. In other words, it is the voltage in the rotor open-circuit terminals (when $i_r = 0$):

$$\vec{e}_r^r = \frac{L_m}{L_s}\frac{d}{dt}\overrightarrow{\psi}_s^r \tag{3.14}$$

During normal operation, the electrical grid is a source of three balanced voltages of constant amplitude and frequency:

$$\begin{aligned} v_a &= \hat{V}_g \cos(\omega_s t + \varphi) \\ v_b &= \hat{V}_g \cos(\omega_s t + \varphi - \frac{2\pi}{3}) \\ v_c &= \hat{V}_g \cos(\omega_s t + \varphi - \frac{4\pi}{3}) \end{aligned} \tag{3.15}$$

The voltage drop in the stator resistance, which is significantly smaller than the total value, can be neglected. At steady state, the space vector of the stator flux is a rotating vector of constant amplitude, proportional to the grid voltage and synchronous speed:

$$\vec{\psi}_s^s = \sqrt{2}\underline{\psi_s} e^{j\omega_s t} = \frac{\hat{V}_g e^{j\varphi}}{j\omega_s} e^{j\omega_s t} \tag{3.16}$$

The variable flux will thus induce an emf proportional to the slip frequency:

$$\vec{e_r^r} = \frac{L_m}{L_s}\frac{d}{dt}\vec{\psi_s^r} = j\omega_r\frac{L_m}{L_s}\vec{\psi_s^r} \tag{3.17}$$

The amplitude of this emf can be expressed as follows:

$$\left|\hat{E}_r\right| = \omega_r\frac{L_m}{L_s}\frac{\hat{V}_g}{\omega_s} = \hat{V}_g\frac{L_m}{L_s}s \tag{3.18}$$

3.5.2 Stator Flux under Disturbances

Generally, grid faults are partial voltage dips. That is the stator voltage drops below its rated voltage but remains above zero. Therefore, the voltage dips analyzed in this section are expressed [34]:

$$\vec{v_s^s} = \begin{cases} \hat{V}_{pre}e^{j\omega_s t} & for\ t < 0 \\ (1-p)\hat{V}_{pre}e^{j\omega_s t} & for\ t \geqslant 0 \end{cases} \tag{3.19}$$

In steady state, the flux is proportional to the stator voltage:

$$\vec{\psi_s^s}(steady\,state) = \begin{cases} \dfrac{\hat{V}_{pre}e^{j\omega_s t}}{j\omega_s} & for\ t < 0 \\ \dfrac{(1-p)\hat{V}_{pre}e^{j\omega_s t}}{j\omega_s} & for\ t \geqslant 0 \end{cases} \tag{3.20}$$

However, the flux does not change instantaneously because it is a state variable. The transient behavior of stator flux can be described in terms of roots of differential equations:

$$\frac{d}{dt}\vec{\psi_s^s} = \vec{v_s^s} - \frac{R_s}{L_s}\vec{\psi_s^s} \tag{3.21}$$

The root of eq. 3.21 includes two components:

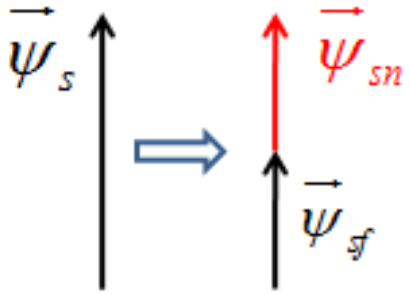

Figure 3.16: Flux evolution under voltage dips

+ The homogeneous solution (natural flux) is the transient or the natural response of the equation. It depends on the initial conditions of the total solution.

+ The particular solution (forced flux) is the steady state response. This solution is proportional to the input of the equation; that is, to the stator voltage. The total flux is the sum of both of them:

$$\vec{\psi}_s^s = \frac{\hat{V}_{fault}}{j\omega_s} e^{j\omega_s t} + \vec{\Psi}_{n0} e^{-t/\tau_s} = \vec{\psi}_{sf} + \vec{\psi}_{sn} \tag{3.22}$$

In eq. 3.22, the first term is forced flux, which is induced by symmetrical voltages after fault, and the second term is natural flux, which appears after fault to prevent discontinuity of stator flux. The evolution of stator flux is demonstrated in Fig. 3.16.

The total emf induced on the rotor side results from the two components of stator flux:

$$\vec{e}_r^r = \frac{L_m}{L_s} \widehat{V}_{pre}(s(1-p)e^{j\omega_r t} - (1-s)pe^{-j\omega_m t} e^{j\omega_r t}) \tag{3.23}$$

The first one is generated by the new grid voltage and its amplitude is small as it is proportional to the slip. Its frequency is the difference between the synchronous and the rotor frequencies; therefore, it usually achieves a few hertz. The second terms

a transient voltage caused by the natural flux. During the dip, high voltages are induced in the rotor mainly due to the natural flux. The maximum is reached during the first instants of the dip, when the natural flux is the highest.

3.5.3 Demagnetizing Current Control

The demagnetizing current control is a recently developed technique to protect the DFIG against voltage dips [35, 36]. As seen before, voltage dips, unless very shallow, cause saturation of the rotor converter and hence loss of the rotor current control. This technique avoids saturation of the converter by introducing an additional current into the rotor that minimizes its voltage.

In a total three-phase dip, the stator voltage becomes zero and the only flux remaining in the machine is the natural flux that induces a high emf in the rotor converter. If nothing is done, the rotor voltage will be very similar to the emf induced and the converter will saturate as a result. However, by introducing a specific current into the rotor, it is possible to reduce the flux and hence to decrease the rotor voltage. Restating the expression of the rotor flux:

$$\vec{\psi}_r = \frac{L_m}{L_s}\vec{\psi}_s + \sigma L_r \vec{i}_r \tag{3.24}$$

From this equation, it is clear that the rotor flux can be reduced by introducing into the rotor a current opposite to the stator flux:

$$\vec{i}_r = -K_d \vec{\psi}_s \tag{3.25}$$

In this case, the rotor flux will be:

$$\vec{\psi}_r = (\frac{L_m}{L_s} - \sigma L_r K_d)\vec{\psi}_s \tag{3.26}$$

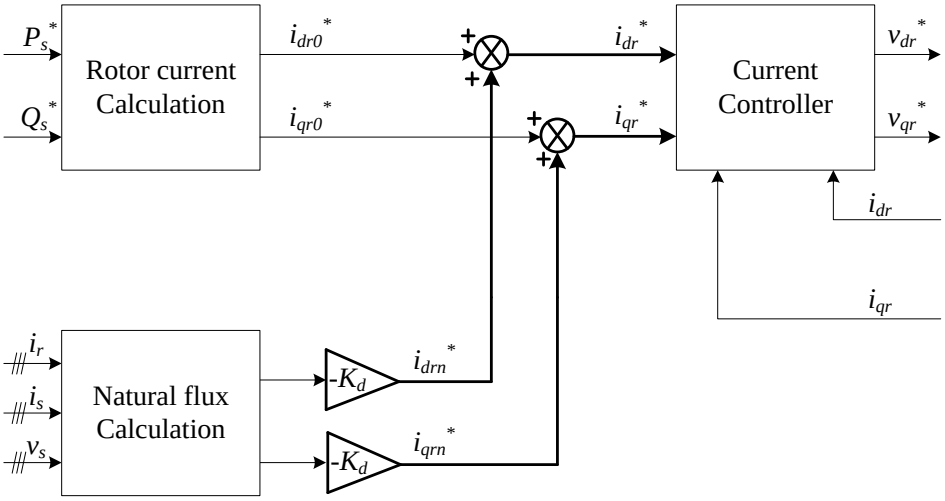

Figure 3.17: Demagnetizing Current Control

That can be zero by adjusting the gain K_d.

The controlling scheme is expressed in Fig. 3.17. The natural flux is independently calculated to be converted into demagnetizing currents, which are added to the original current reference.

The injection of a current opposite to the magnetic flux to reduce the voltage is a well-known technique mostly applied to brushless electrical drives. The difference with the control described here is that now the technique is solely applied to the natural and negative fluxes and not to the positive flux, because the positive flux does not induce an emf. With this method, it is possible to completely cancel the natural and negative fluxes, so that only positive flux remains, which does not cause saturation of the rotor converter.

3.5.4 LVRT using Proposed Method

In next case study, the systems capability of low voltage ride-through (LVRT) is investigated. Grid voltage dips are very sensitive to DFIG WTs, which are connected to the grid directly. When the voltage dips occur, they can cause oscillations of the

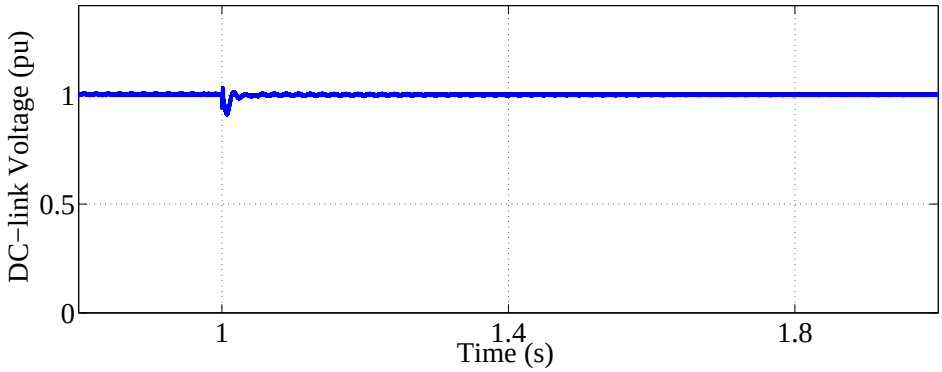

Figure 3.18: DC-link voltage during dips

stator flux, as explained in previous sections. These oscillations can make the RSC saturated and incapable of current control. In addition, in order to fulfill the new grid code, DFIG WTs are required to remain the connection to the grid, inject reactive power and halt the active power generation as well [37]. These response requirements of the new grid code help a power grid recover faster.

In the LVRT case study, the simulation model of DFIG WTs is operated during the grid dips of 50% its nominal values, and the wind speed is assumed constant during conducting. Before $t_0 = 1$s, the system is under normal operation. After that time, the grid voltage drops out to 50% the rating value, as seen in Fig. 3.19. The DC voltage is stated in Fig. 3.18. In this research, to safely maintain the connection of DFIG WTs to the grid under voltage dips, a demagnetizing method, as proposed in [38], is utilized. This method can diminish the oscillations of stator flux during voltage dips.

The magnitude of stator flux is demonstrated in Fig. 3.20. When employing the demagnetizing method, the proposed system can damp the oscillations within 0.05s. The results of PI controller, which has longer response time, are also shown in Fig. 3.20. These results confirm that the demagnetizing method during voltage dips can be implemented efficiently using the proposed nonlinear control. As demonstrated in

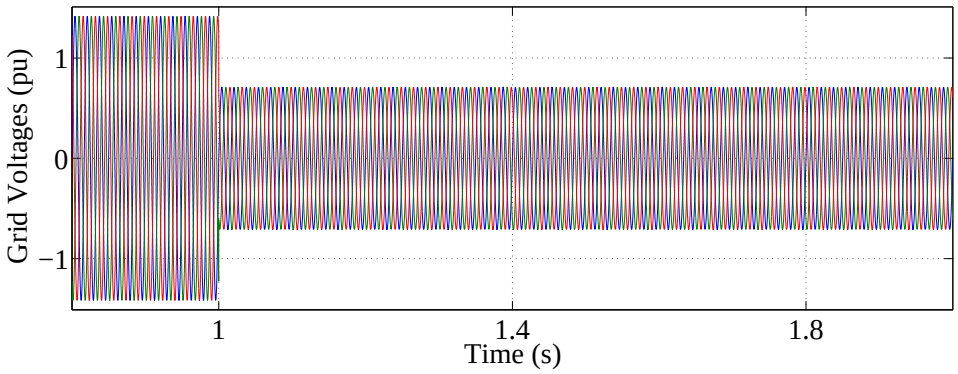

Figure 3.19: Grid voltage during dips

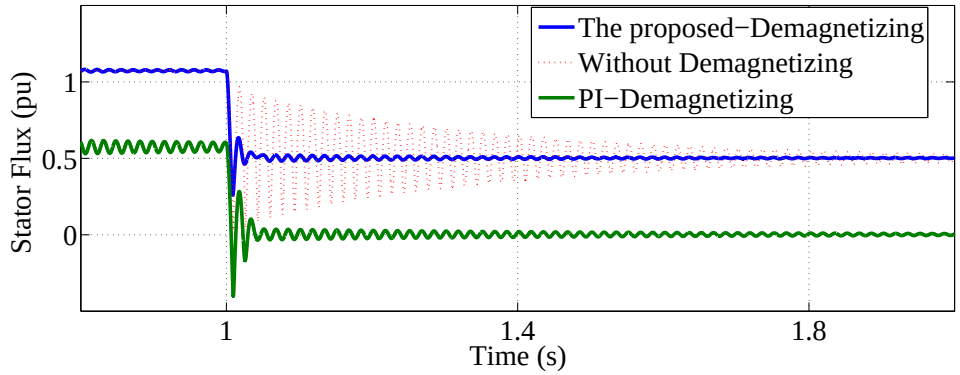

Figure 3.20: Stator flux magnitude during dips

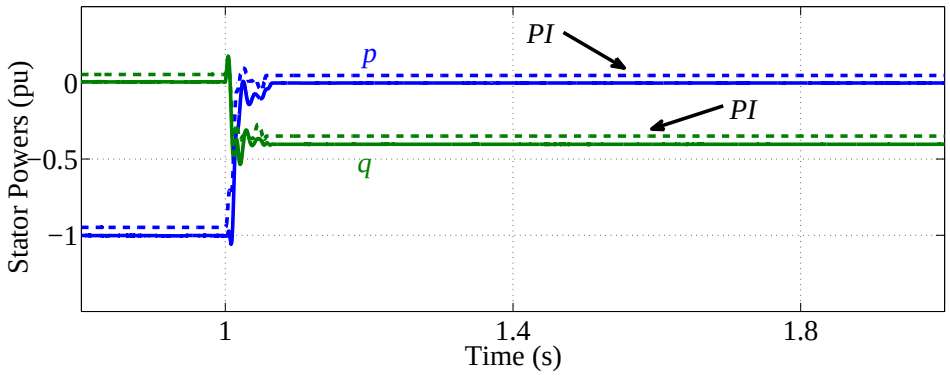

Figure 3.21: Stator powers during dips: new method (solid) and PI (dash)

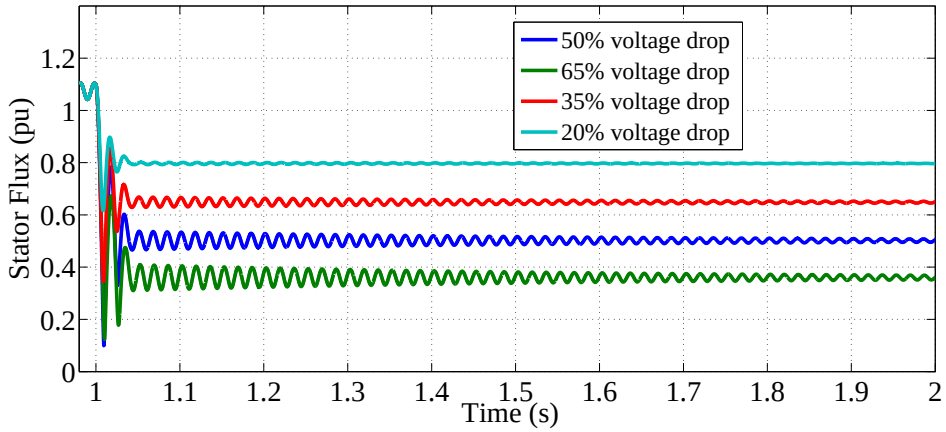

Figure 3.22: Stator flux - various cases of dips: PI controller

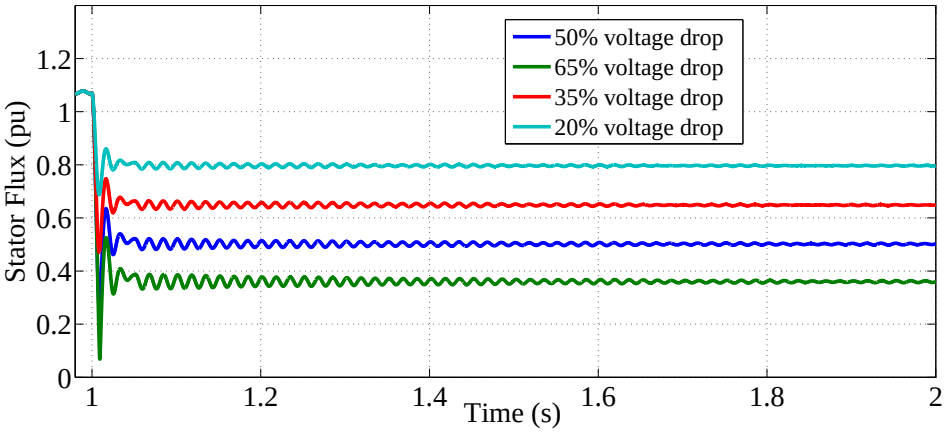

Figure 3.23: Stator flux - various cases of dips: new method

Fig. 3.21, after voltage dips, the system can respond very fast by turning the active power into zero and injecting the reactive power 0.4pu into the grid.

Various cases of voltage disturbances are conducted to validate the demagnetizing ability of the proposed method and the PI method. As seen in Figs. 3.22 and 3.23, the oscillations are eliminated within approximately 0.05s and 0.1s for the new controller and the PI controller respectively in all cases. Under voltage disturbances, the proposed method performs better that the traditional PI. Pay attention that the higher voltage dips are, the more initial oscillations.

3.6 Summary and Discussion

In this research, the new space-vector based nonlinear controller is proposed for the power converter of DFIG WTs. This algorithm can control the rotor currents based on the two errors of current components in dq-reference-frame directly. The proposed method is not only validated on power control for DFIG under variations of power demands, rotor speeds and machine parameters, but it also has the capability of low voltage ride through. The simulation results show that it has a very fast dynamic response with voltage disturbances in various cases. The results also confirm the effectiveness of the proposed method under disturbances and variations of machine parameters, compared to the traditional PI controller. In summary, advantages and disadvantages of the proposed method are stated as follows:

Advantages:

+ The proposed method can overcome the issue of parameter influence of traditional VOC. Under change of 50% of rotor resistance, the nonlinear method's output is stable, while the output power of VOC varies about 10%.

+ The strategy of this nonlinear current control can replace the PI-regulators without changing basic structure of VOC. Therefore, it is convenient for researchers to utilize the proposed method for their own schemes of vector control.

+ Capability of LVRT is better than traditional VOC. The oscillations of stator flux are eliminated within approximately 0.05s by the proposed method and 0.1s by the traditional method. Moreover, overshoot of stator flux under 50% disturbances are 0.2pu for the proposed method and 0.4pu for the traditional one.

Disadvantages:

+ Because of vector selection principle, the nonlinear control has the same issue as DPC strategy: inconstant switching frequency. The effect of this advantage is analyzed in literature, and it is acceptable for application of DPC to DFIG control

Table 3.1: Comparisons between VOC, DPC and proposed method

	VOC	Nonlinear	DPC
Change of rotor resistor	unstable	stable	stable
Oscillation time of Φ_s	0.1s	0.05s	no data
Overshoot of Φ_s	0.4pu	0.2pu	no data
Switching frequency	constant	unconstant	unconstant

[10, 11, 31]. However, this advantage is still needed to be improve in future.

Comparison between VOC, DPC and proposed method is demonstrated in Table 3.1. In future, the improvements for this method to overcome the general case of disturbances, which is not only symmetrical voltage dips, will be considered.

Chapter 4

Self-Compensating DFIG: an Approach of Low-Cost Structures

4.1 Motivation

In previous chapter, stability control is proposed and analyzed in detail. This control method can tackle issues of traditional controller. In addition to control methods, structures of power converter are an important topic of research on DFIG WTs. The number of installed DFIG WTs is tremendously increased during last decades. This trend makes cost of installation is very competitive in the market. Therefore, low-cost structures of power converters in DFIG system are studied in the two next chapters. The low-cost method for traditional DFIG system is introduced in chapter 4, and the one for hybrid Photovoltaic-DFIG system is presented in chapter 5. A simplified structure is introduced and analyzed in this chapter. Also, a method of Self-compensating DFIG is proposed to maintain the power quality of the simplified structure. In addition, advantages and disadvantages of proposed structure and other structures, which are proposed for cost-reducing purpose in literature, are reviewed

and discussed.

4.2 Instantaneous Power Theory

In order to analyze the power quality influence, the instantaneous power theory is used in this paper. The instantaneous powers, which include the instantaneous real power p and the instantaneous imaginary power q, are defined in eq. 4.1 [40].

$$\begin{bmatrix} p \\ q \end{bmatrix} = \begin{bmatrix} v_\alpha & v_\beta \\ v_\beta & -v_\alpha \end{bmatrix} \begin{bmatrix} i_\alpha \\ i_\beta \end{bmatrix} \tag{4.1}$$

Where v and i are instantaneous voltage and current, subscripts α and β are components in α-axis and β-axis respectively.

Otherwise, the instantaneous currents can be calculated as follows:

$$\begin{bmatrix} i_\alpha \\ i_\beta \end{bmatrix} = \frac{1}{v_\alpha^2 + v_\beta^2} \begin{bmatrix} v_\alpha & v_\beta \\ v_\beta & -v_\alpha \end{bmatrix} \begin{bmatrix} p \\ q \end{bmatrix} \tag{4.2}$$

Equation 4.2 is very important to calculate the compensating currents for a power system.

4.3 Low-Cost Structures for DFIG System

A typical grid-tied DFIG system is shown in Fig. 4.1(a). The back-to-back converter is mainly used in this structure. It includes two converters: Rotor Side Converter (RSC), which handles rotor currents to control the output powers, and Grid Side Converter (GSC), which handles grid-side currents to control the DC link voltage and the power factor at Point of Common Coupling (PCC) [41]. Hence, every converter needs a respective controller and associated circuits. These circuits increase not

only the cost but also maintenance services. In literature, there are several converters proposed to replace the back-to-back converter, such as Matrix converter or 9-switch converter [42, 43]. The matrix converter has smaller size compared to the traditional back-to-back due to elimination of DC capacitor [42]. In addition, the 9-switch converter has fewer switches than the back-to-back [43]. However, control methods for these converters are very complicated and the power quality is still required to improve. Therefore, in this research, a simple approach of a low-cost structure is proposed and analyzed.

In order to simplify the traditional structure, the GSC is replaced by two simple AC/DC converter: 6-diode rectifier (6DR) and single-switch rectifier (SSR), as seen in Fig. 4.1(b). The 6DR is cheaper and more durable than the fully-controlled GSC. In addition, the 6DR can work without a controller. Another simplified structure proposed is single-switch rectifier (SSR). The SSR can control the DC-link voltage with a simple controller for only one switch [44–46]. These converters are really simpler and cheaper compared with the GSC. Using them, associated circuits of GSC, such as protection and heat-sink circuits, can be removed.

4.3.1 Simplified Structures to Replace GSC

6-diode rectifier is a very classical and simple AC/DC converter. It can rectify the input AC voltage into DC voltage without a controller. However, due to passive components, 6DR cannot control the DC-link value and distorts input AC currents, as illustrated in Fig. 4.2.

On the other hand, single-switch rectifier is a simplified structure proposed to convert AC voltages into a controllable DC voltage. The SSR consists of only one switch and 7 diodes. The SSR is capable of controlling DC voltage, but it cannot maintain sinusoidal currents on AC side, as stated in Fig. 4.2. A control diagram of

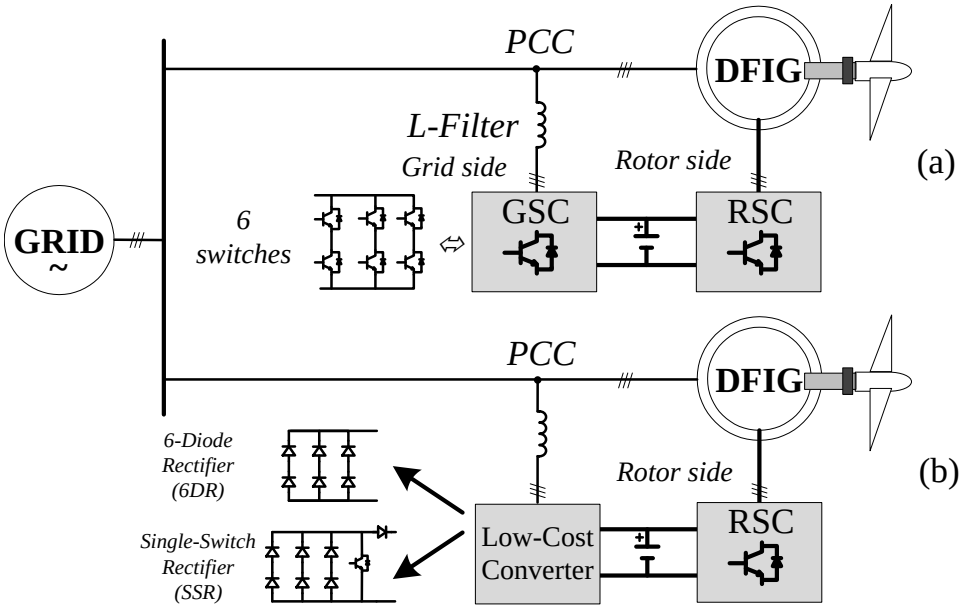

Figure 4.1: Diagram of DFIG system: (a) Traditional system (b) Low-cost system

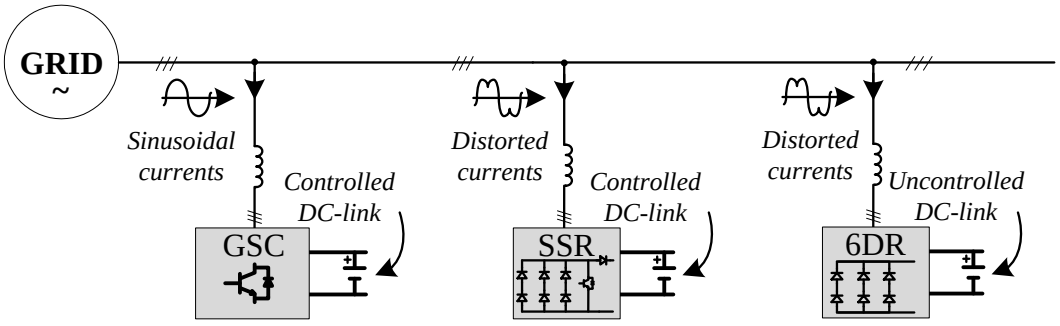

Figure 4.2: Comparisons of GSC, SSR and 6DR

the SSR [44] is demonstrated in Fig. 4.3. The main principle is that the switch is controlled to increase the DC current i_{dc} to boost the DC voltage and vice versa. In several papers, cascaded passive filters are designed to improve the AC side quality of SSR [45, 46]. They are very bulky, complicated and not cost-effective. In order to keep the proposed structure simple, an L-filter is used in this research.

As mentioned before, the two simplified converters are not capable to maintain

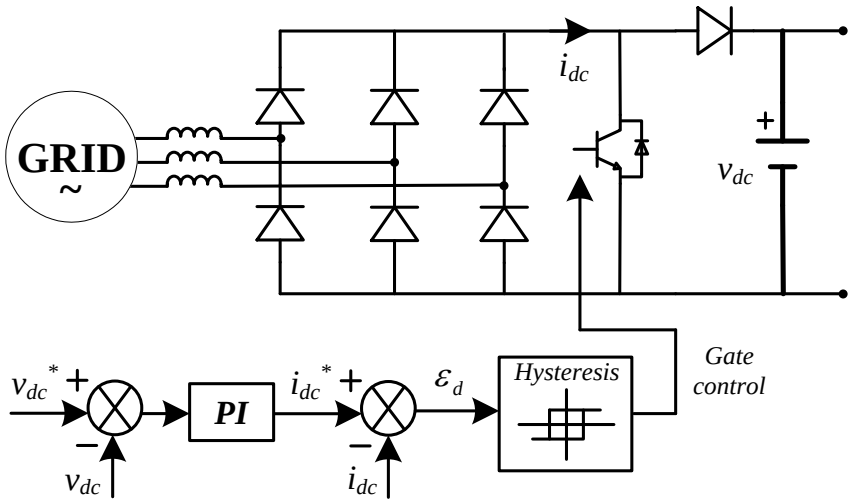

Figure 4.3: Structure and control diagram of SSR

the AC currents. These distorted currents on AC side can influence the power quality. The influence is illustrated in details in the next subsection.

4.3.2 Power Quality Influence of 6DR and SSR

The instantaneous currents of 6DR and SSR are shown in Figs. 4.4 and 4.4 respectively. These rectified currents are not sinusoidal waveforms, so they affect not only the power factor but also the power quality. The instantaneous voltages and currents of the two converters are used to analyze the instantaneous powers.

The instantaneous powers of 6DR and SSR are demonstrated in Figs. 4.6 and 4.7. It is obvious that every power superposes two power components, which are average and oscillating ones, in both cases of 6DR and SSR. These components can be expressed as

$$\begin{cases} p = \bar{p} + \tilde{p} \\ q = \bar{q} + \tilde{q} \end{cases} \tag{4.3}$$

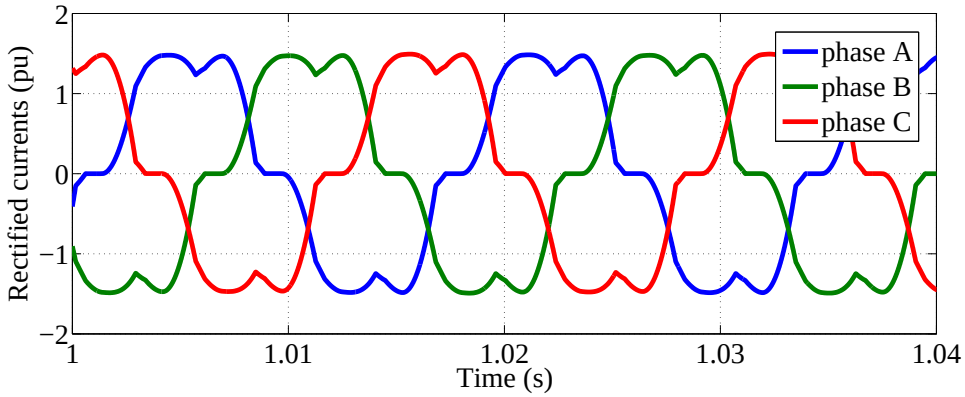

Figure 4.4: AC currents of 6DR

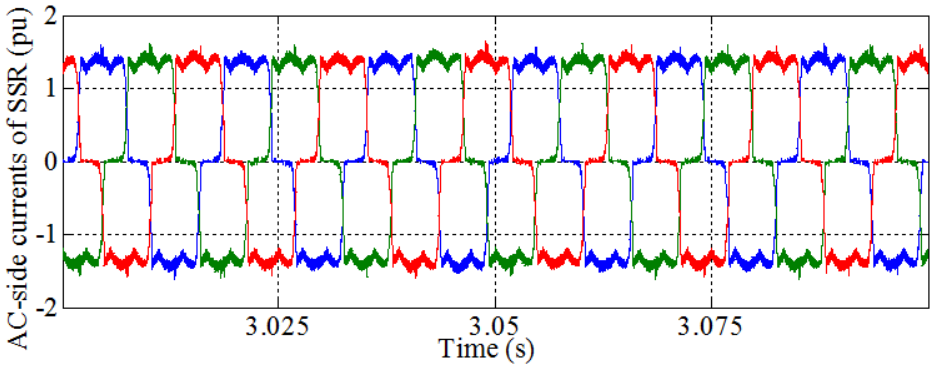

Figure 4.5: AC currents of SSR

where $\bar{p}$, $\tilde{p}$ and $\bar{q}$, $\tilde{q}$ represent the average and oscillating terms of p and the average and oscillating terms of q respectively. The oscillating real and imaginary powers are related to the presence of harmonics in the power grid.

4.4 Self-Compensating Method

As explained in previous section, the oscillating powers of the simplified converters strongly degrade the power quality. It is inevitable to remove these powers for adoption of the simplified diagram of DFIG. The SC-DFIG method is proposed to

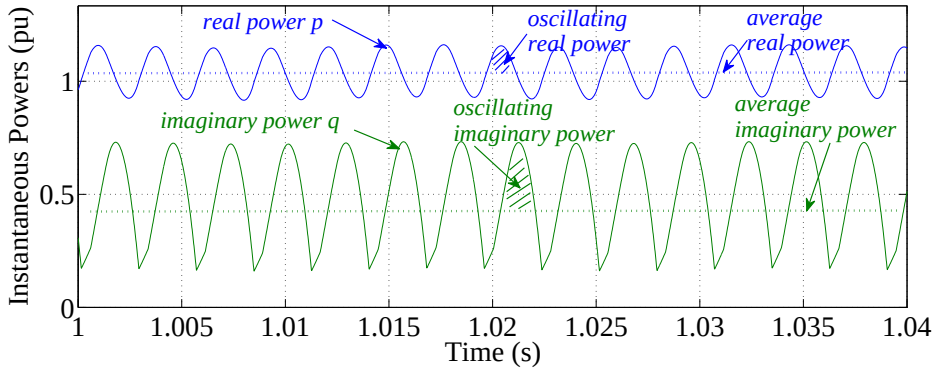

Figure 4.6: Instantaneous powers of 6DR

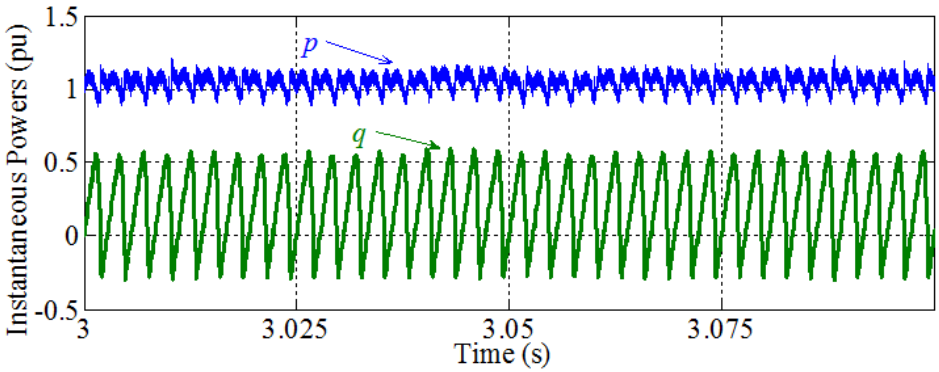

Figure 4.7: Instantaneous powers of SSR

eliminate the oscillating powers by controlling DFIG to compensate them.

As seen in Fig. 4.8, in addition to the conventional reference stator power (p_s, q_s), the DFIG also injects additional oscillating powers. The oscillating powers injected by the DFIG are to compensate the oscillating ones injected by the simplified converter. In other words, they are similar in terms of absolute value and different in terms of sign. In addition to the oscillating powers, the average imaginary power can also be compensated by DFIG to maintain the unity power factor. As a result, the grid powers (p_{grid}, q_{grid}) are shown in eq. 4.4 after compensating. The oscillating components are

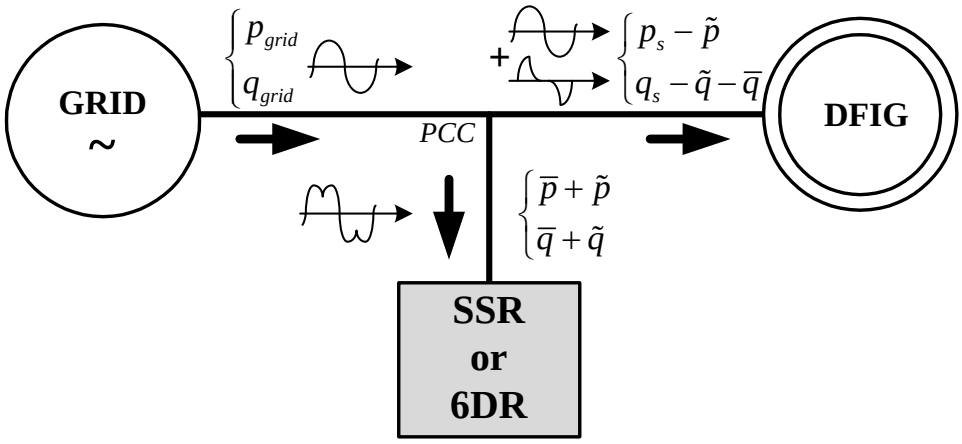

Figure 4.8: Power flow of SC-DFIG method

obviously eliminated from the grid powers.

$$\begin{cases} p_{grid} = (p_s - \tilde{p}) + (\bar{p} + \tilde{p}) = p_s + \bar{p} \\ q_{grid} = (q_s - \tilde{q} - \bar{q}) + (\bar{q} + \tilde{q}) = q_s \end{cases} \tag{4.4}$$

The entire schematic diagram of proposed method is stated in Fig. 4.9. This diagram is intentionally illustrated for SSR, but it is completely similar to the one of 6DR. The compensation method in this diagram is based on the method of Active power filter, which uses a power electronic converter, a transformer and a filter (inductor) to compensate high-order harmonic currents of the grid power [40]. The structure of active power filter (converter-transformer-grid) is relatively similar to the structure of RSC-DFIG-grid in forms of equivalent circuits. The controller consists of four main components namely: Instantaneous power calculations, Compensating power selection (Low pass filter), Reference rotor current calculations and PWM current controller. The functions of these components are discussed as follows.

1. Instantaneous power calculations: the grid voltages v_{grid} and the SSRs currents i_{rect} are used to calculate the instantaneous powers (p_{rect}, q_{rect}) which the SSR consumes by using eq. 4.1. These powers, as analyzed before, include the

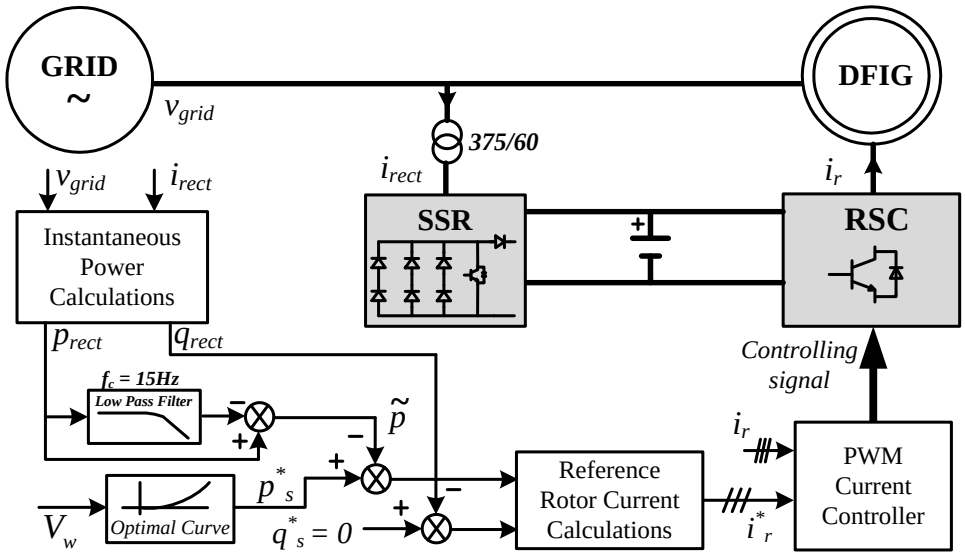

Figure 4.9: Schematic diagram of the proposed system

oscillating powers which must be eliminated.

2. Compensating power selection: the specific compensating powers are selected using a low pass filter. As discussed before, the oscillating real power and the entire imaginary power are specified to be eliminated. Subsequently, the typical command powers (p_s^*, q_s^*) are adjusted to take into account the compensating powers.

3. Reference rotor current calculations: From eq. 4.2, this component supervises the reference rotor currents i_r^* which are based on the command powers in previous steps.

4. PWM current controller: a typical hysteresis current controller is utilized to handle the RSC. The dynamic response of this controller for current compensation is validated in [40]. The primary function of the RSC is to maintain the rotor currents ir following the references.

4.5 Evaluation of SC-DFIG Structures

The control strategy of low-cost DFIG system is validated using Matlab/Simulink. The sampling time of simulink model is 1e-5s, and the switching frequency of the current controllers is 5kHz with the hysteresis band 1.5%. The simulations are carried out for three case studies to investigate:

1. Feasibility of the proposed system
2. Performance under changes of power demands and wind speed
3. Comparisons between SSR and back-to-back converter

In the case studies, the proposed system is controlled under unity power factor operation mode. This operation mode maintains the reactive power injected to the grid equal zero and generates a stable active power in accordance with active power demand. The results of both 6DR and SSR systems are shown in case studies 1 and 2. The parameters of the system are shown in Table B.1.

4.5.1 Feasibility of the SC-DFIG System

This case study is conducted to assess the compensating and DC-link controlling capability of the proposed system. In addition, because of short-time simulation, the wind speed is assumed constant at 0.9pu in this case study. At the beginning, the low-cost DFIG system is operated under the traditional control mode which generates only the stable command powers. The systems are switched to the compensating mode injecting additional oscillating powers at the given time, which is 1.5s for 6DR-struture and 2s for SSR-structure. In this paper, the negative value of power indicates a direction of power from the generator to the grid, such as p = -1pu. The analysis of results for both structures is stated as follows.

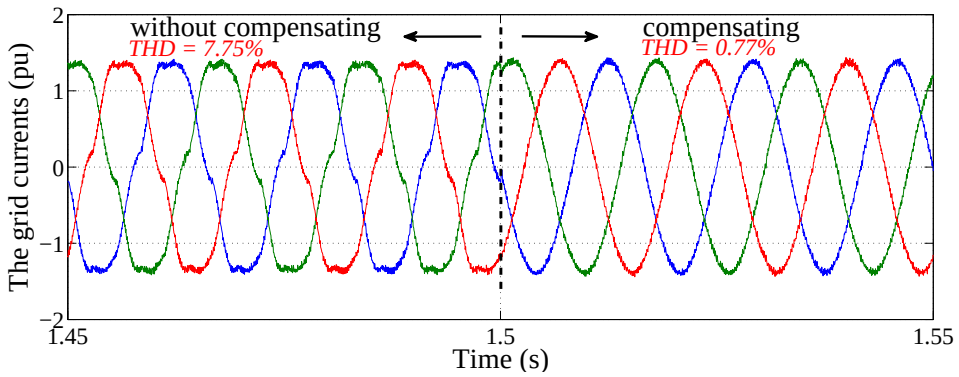

Figure 4.10: Grid currents after compensating of 6DR

in case of 6DR: Fig. 4.10 shows three-phase currents of power grid, which are distorted before 1.5s. When the compensating mode is turned on, these currents become sinusoidal shapes. Consequently, the total harmonic distortion (THD) of grid currents is significantly diminished from 7.75% (without compensating) down to 0.77% (compensating). In addition, the compensating algorithm does not change the magnitude of grid currents, but eliminating their high order harmonics. Instantaneous grid powers are demonstrated in Fig. 4.11 to evaluate the power quality. The distorted grid currents do not only cause oscillations of powers, but they also inject the instantaneous imaginary power of 0.2pu. After 1.5s, the instantaneous imaginary power is decreased to nearly zero. Moreover, the two powers become more stable after the compensating algorithm is conducted. Therefore, the power quality is improved remarkably. The rotor currents are illustrated in Fig. 4.12. After the compensating mode is enabled, the rotor currents change from sinusoidal shape into harmonic-containing shape. These high-order harmonics on the rotor side are to generate the compensating powers on the stator side.

in case of SSR: Fig. 4.13 shows three-phase currents of power grid, which become sinusoidal shapes after 2s. Similar to previous case, the THD index of grid

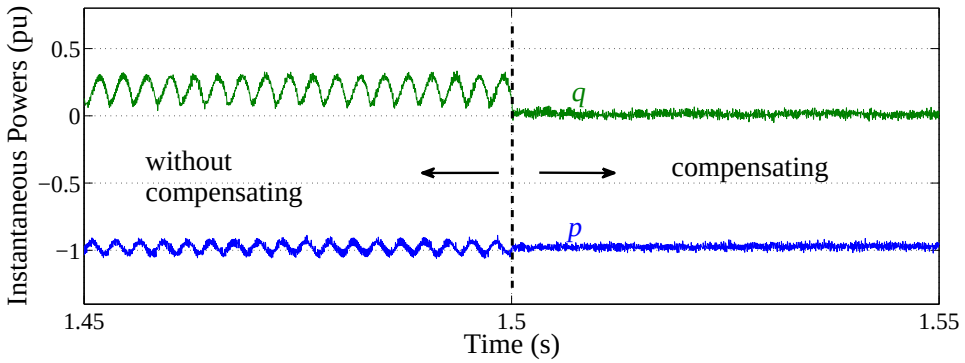

Figure 4.11: Instantaneous powers after compensating of 6DR

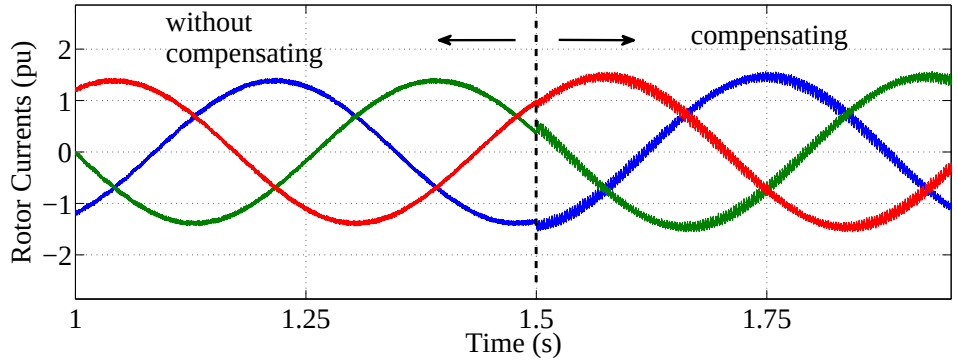

Figure 4.12: Rotor currents after compensating of 6DR

currents is decreased from 6.97% (without compensating) down to 0.89% (compensating). Instantaneous grid powers are shown in Fig. 4.14. After 2s, the two powers also become more stable because of the compensating method. The rotor currents and the electromagnetic torque are illustrated in Figs. 4.15 and 4.16 respectively. Notice that the compensating method slightly affects the generators torque, because the oscillating real power of SSR is much smaller than p_s and the compensating reactive power q_{rect} does not influence the torque.

Capability of DC-link voltage control of SSR structure is demonstrated in Fig. 4.17. The DC voltage is changed from 0.8pu to 1pu at 2.5s and from 1pu to 0.9pu at 3s. The response is very fast.

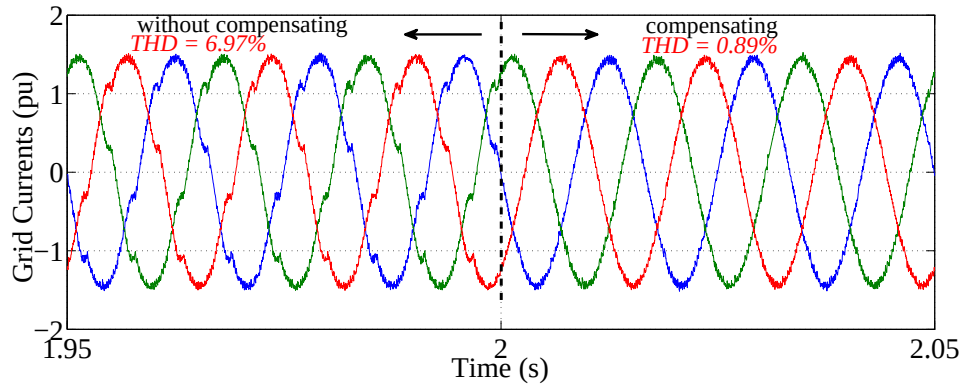

Figure 4.13: Grid currents after compensating of SSR

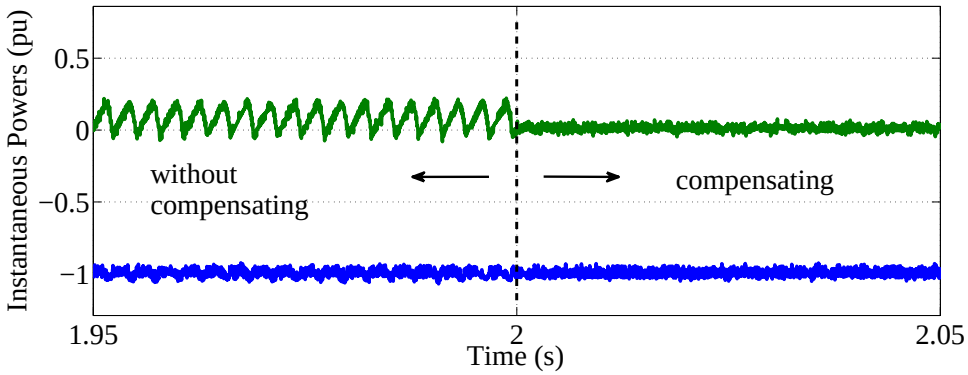

Figure 4.14: Instantaneous powers after compensating of SSR

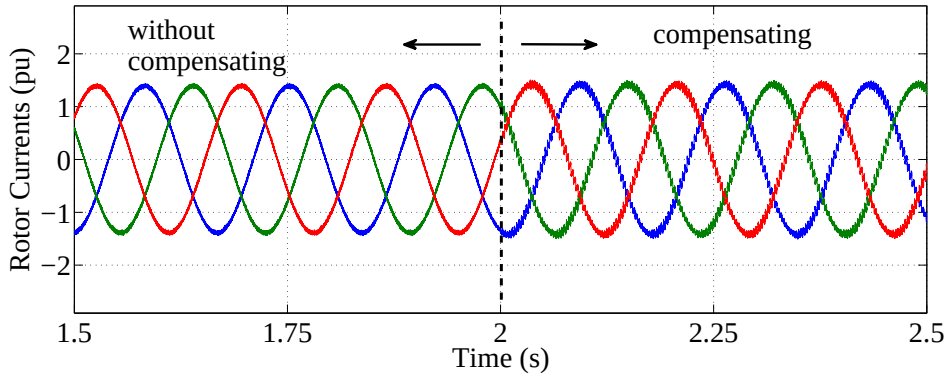

Figure 4.15: Rotor currents after compensating of SSR

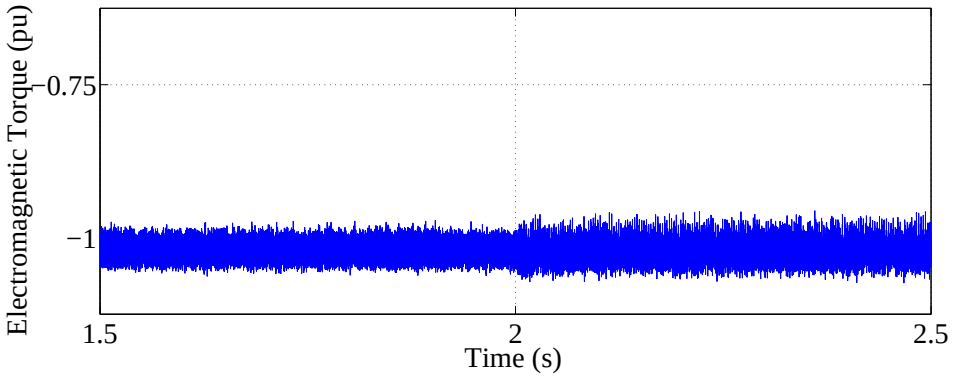

Figure 4.16: Electromagnetic torque after compensating of SSR

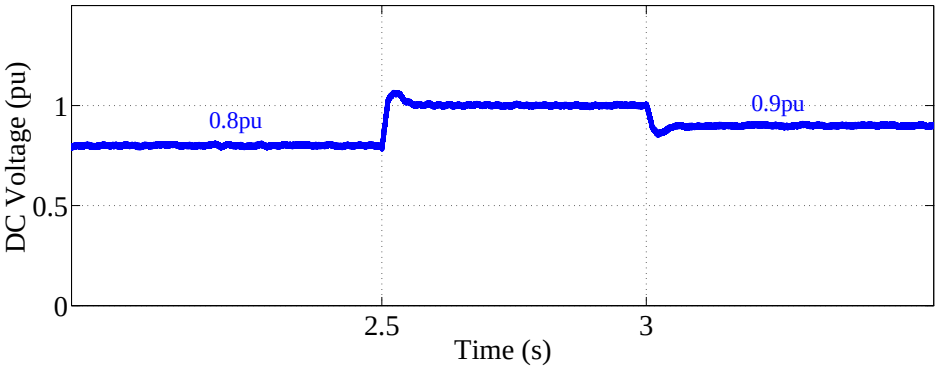

Figure 4.17: Controllable DC voltage of SSR

4.5.2 Performance under changes of power demands and wind speed

In this case study, the DFIG is controlled under various active power steps to evaluate dynamic responses of the proposed system. As seen in Fig. 4.18, the active power is controlled to change from -1pu to -1.1pu at 2.5s and from -1.1pu to -0.9pu at 3s. The responses of the output power are very fast. The reactive power is still kept at zero level under these changes. The DC-link voltage is kept stable by SSR, as illustrated in Fig. 4.19. The DC voltage of the SC-DFIG with 6DR is also shown in Fig. 4.19. The DC-link uncontrollability of 6DR is improved using SSR.

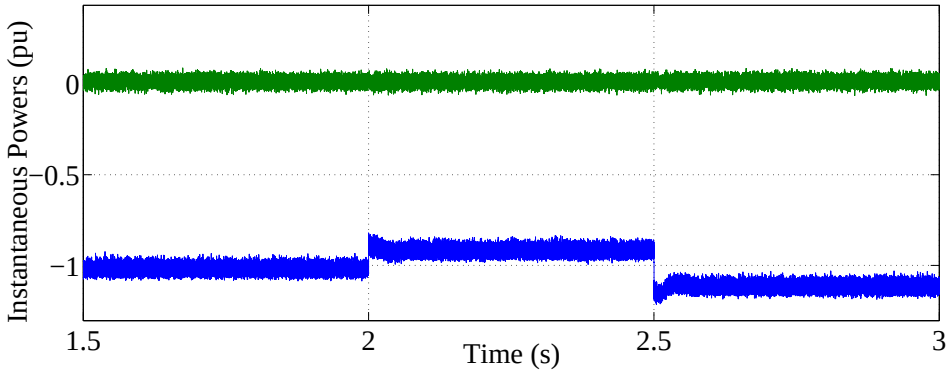

Figure 4.18: Step-changing of output powers

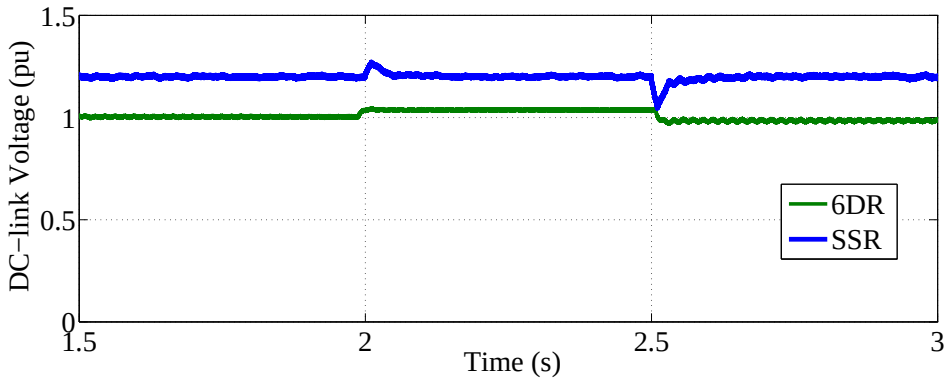

Figure 4.19: DC voltages of SSR and 6DR under power changes

Slope-changing of wind speed is also conducted in this case study. When the wind speed changes, the active power demand is controlled according to the optimal power method in Fig. 2.6. As illustrated in Fig. 4.20, the wind speed is decreased from 0.95pu to 0.85pu during the interval from 2.5s to 3.5s, and increased from 0.85pu to 0.95pu from 3.5s to 4.5s. The output active power is smoothly generated in respect with wind speed, as seen in Fig. 4.21. The rotor speed is also shown in Fig. 4.20 to illustrate the behavior of the rotor under the optimal control. Moreover, the DC voltage is maintained unchanged in this case, as illustrated in Fig. 4.22. In contrast, the DC voltage of the 6DR system is strongly varied. The constant DC voltage

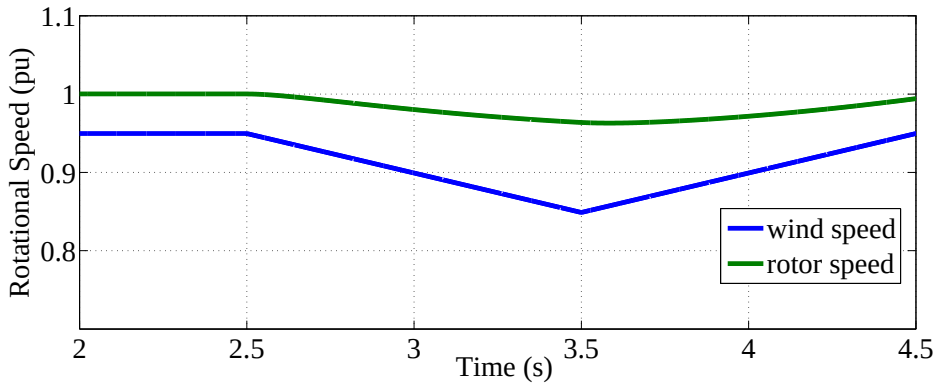

Figure 4.20: Wind speed variations

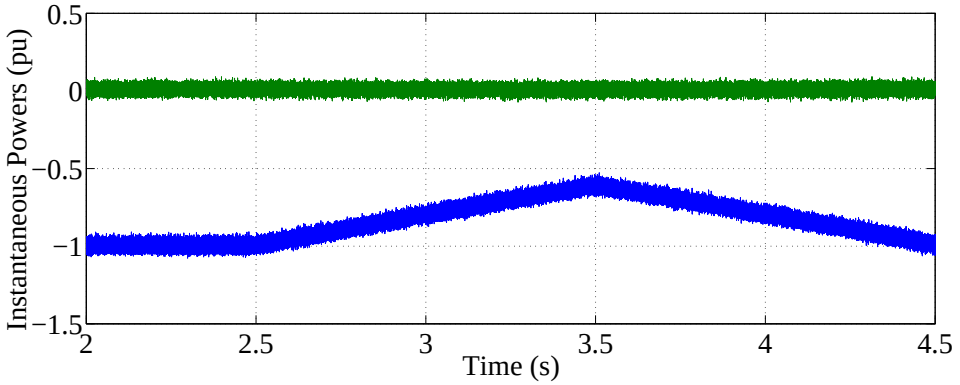

Figure 4.21: Output Powers under wind speed changes

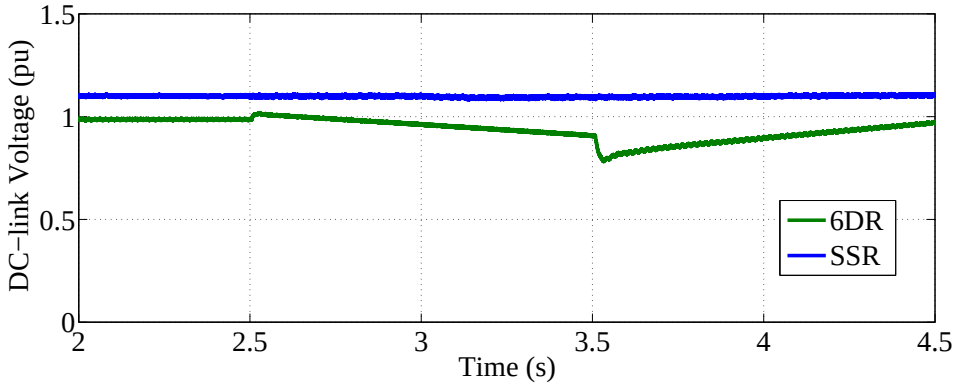

Figure 4.22: DC voltages of SSR and 6DR under wind speed changes

confirms the capability of DC-link control in the low-cost system equipped SSR.

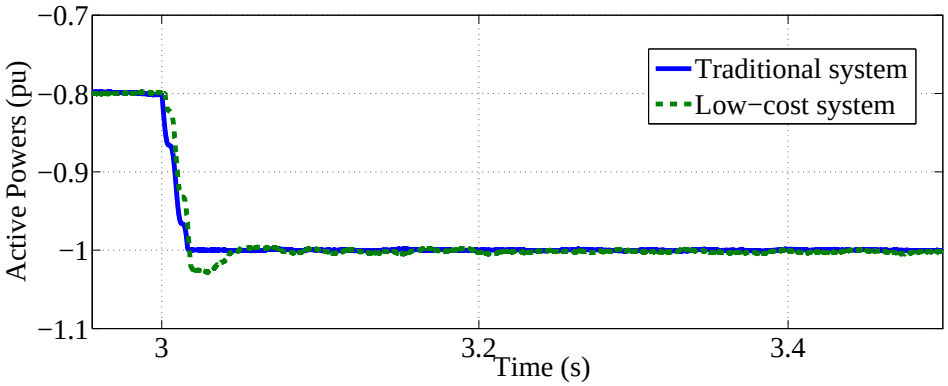

Figure 4.23: Comparisons of active power responses

4.5.3 Comparisons between SSR and back-to-back converter

Responses and THD index of the traditional DFIG system, which uses a back-to-back converter, are analyzed along side with results of the SC-DFIG system based on SSR. Fig. 4.23 illustrates the responses of generated power during step-changing of power demand from -0.8pu to -1pu. Note that conventional active powers are used in this case, not instantaneous powers. The response time of the traditional system and the proposed system is about 15ms and 45ms respectively.

THD index of the two systems are shown in Figs. 4.24 and 4.25 under various power demands and wind speed respectively. The traditional system has better index than the low-cost system. However, the THD index of the proposed system is still less than 4%, which is an IEEE standard limit for grid connection of distributed sources [39]. In Fig. 4.26, the analysis of harmonics under 20th-order is illustrated for three cases: the SC-DFIG system based on SSR without compensating, the proposed system based on SSR with compensating and the traditional system based on back-to-back converter.

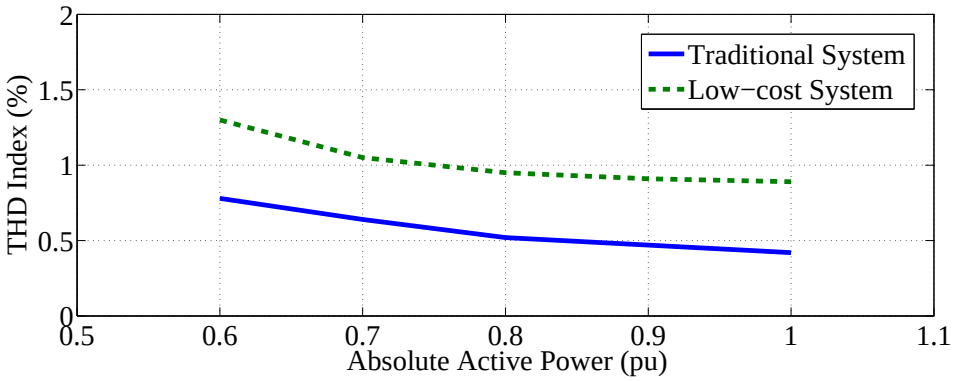

Figure 4.24: Comparisons of THD index in respect with output power

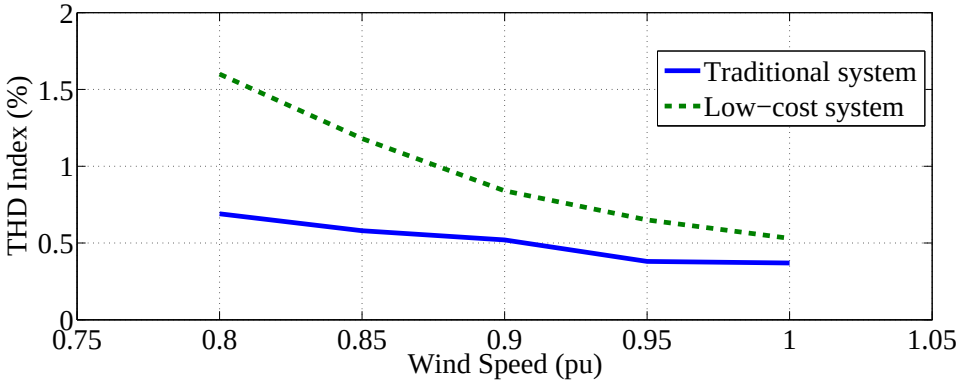

Figure 4.25: Comparisons of THD index in respect with wind speed

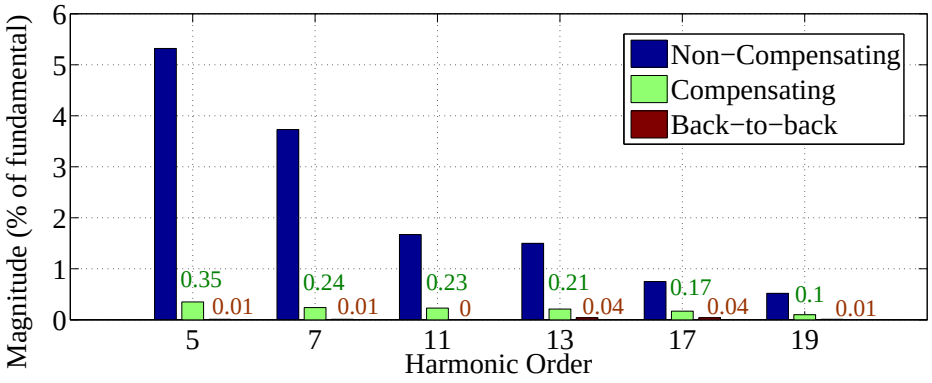

Figure 4.26: Comparisons of barchart of harmonics under 20th-order

Table 4.1: Comparisons of simplified structures

	B2B	Matrix	9-switch	Low-cost structure
Number of switches	12 (100%)	9 (75%)	9 (75%)	7 (58%)
Control structure	2 traditional dq-frame	complicated	complicated	1 dq-frame and simple for 1 switch
DC-link control	yes	no DC-link	yes	yes
Wind speed range	$\omega_s + 30$ to $\omega_s - 30\%$	$\omega_s + 30$ to $\omega_s - 30\%$	$\omega_s + 30$ to $\omega_s - 30\%$	ω_s to $\omega_s - 30\%$

4.6 Summary and Discussion

In this research, the low-cost DFIG system is proposed and analyzed. In this system, the complicated GSC is replaced by the 6-switch rectifier and the single-switch rectifier, which are simpler and cheaper. The high-order currents of the simplified converters are compensated by the DFIG, so the DFIG can generate stable powers to the grid at the PCC without the conventional GSC. The SC-DFIG is designed to work in sub-synchronous mode only. In the sub-synchronous mode, the simplified converter is required to supply about $0 \sim 30\%$ power of the generator rating. This slip power is completely similar to what the back-to-back converter handles under the sub-synchronous mode. So SC-DFIG system needs the same rating-power converter as the traditional B2B. Table 4.1 illustrates properties of the proposed low-cost structure along with other simplified structures. Features and drawbacks of this structure are stated in detail in the following:

Advantages:

+ The low-cost structures reduce the number of switches in DFIG power converter, 7 switches using SSR and 6 switches using 6DR (respectively 58% and 50% compared to switch number of traditional back-to-back converter)

+ Control diagram is simpler than traditional B2B's diagram. It takes 2 dq-frame

controllers for B2B and only 1 dq-frame controller for low-cost structure with basic control for 1 switch of SSR.

+ DC-link voltage is also maintained stable although the GSC is eliminated

Disadvantages:

+ THD index of low-cost structure is higher than the one of B2B. In operation at power of 0.8pu, THD index is 0.9% using low-cost structure and 0.5% using B2B. In operation at wind speed of 0.85pu, THD index is 1.2% using low-cost structure and 0.6% using B2B. However, they are still less than 4% in compliance with IEEE standard limit for drid connection of distributed sources.

+ The proposed system can operate in a range of wind speed from ω_s to $\omega_s - 30\%$.

By utilizing the SC-DFIG system, it is possible to remove many peripheral circuits of GSC which increase the cost of installations and maintenance services. Overall, this system is a promising method for low-cost DFIG wind turbine systems, especially in rural or remote areas.

Chapter 5

Hybrid Photovoltaic-DFIG System with Sensorless Control

5.1 Introduction

As mentioned in chapter 4, study of low-cost structures is focused in chapters 4 and 5. In last chapter, the low-cost method for power converters in traditional DFIG system is presented using the simplified power converter. In this chapter, a cost-efficient method for power converters in hybrid PV-DFIG system is proposed. Typically, the hybrid PV-DFIG system is developed to reduce the cost of two separate PV and DFIG systems in literature. In order to go a step further, the proposed method in this chapter can reduce the number of PV sensors. The current and voltage sensors are conventionally used to measure the PV power for Maximum power point tracking (MPPT). The proposed method can track the maximum power of PV system without current sensor. This sensorless MPPT method, which will be explained in detail in next sections, can efficiently reduce the cost of the hybrid PV-DFIG system.

5.2 Overview of PV-DFIG System

5.2.1 Overview

With rising concerns about shortage of conventional energy sources such as oil, coal or natural gas, wind and photovoltaic powers become more attractive and sustainable alternative for future. They have recently been two most promising sources. During the past several decades, the world has witnessed the novel developments of power electronics and semi-conductor technology. Those play an important role to reduce the cost of PV and make the energy conversion of PV more efficient than ever before. The improvements of power electronics also boost the wind industry to become more practical.

As mentioned in previous chapters, traditional structure of DFIG WTs is shown in Fig. 5.1. A back-to-back converter including a Rotor Side Converter (RSC) and a Grid Side Converter (GSC) is employed in this structure. Fig. 5.2 illustrates a typical grid-tied configuration of PV system. In this configuration, a DC/DC converter is used maximum power point tracking (MPPT) method of PV system. Moreover, an inverter is employed to convert the DC power into the AC power. To combine these configurations, the inverter of PV system is eliminated and the DC/DC converter output is directly connected to the DC-link of back-to-back converter in the hybrid system, as demonstrated in Fig. 5.3.

The combination of DFIG and PV systems is introduced and analyzed in literature [53–58]. In [53], energy management method of PV-DFIG system is presented. This system also includes the battery storage for energy back-up. Efficient control methods are proposed for this hybrid system as well. For example, Khemiri *et al.* introduce the backstepping control strategy for DFIG in the hybrid system [54]. In [55], Zarei *et al.* present the predictive DPC method for DFIG and an analytical method for MPPT

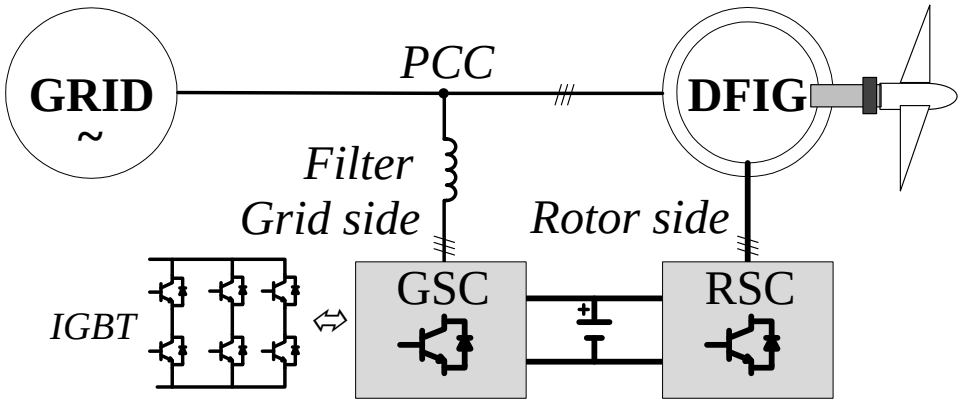

Figure 5.1: Typical structure of DFIG WTs

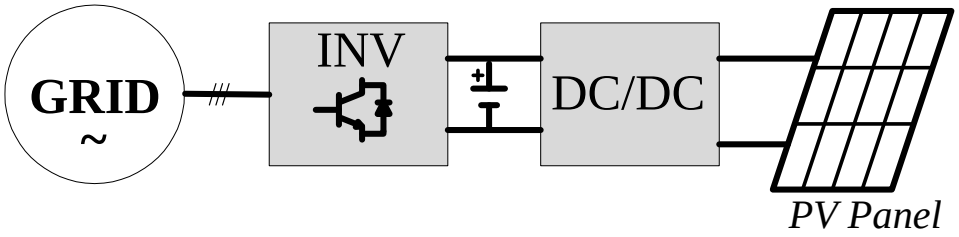

Figure 5.2: Typical structure of grid-tied PV system

of PV. Using the GSC of the hybrid system as an active power filter for harmonic compensation is reported in [56]. A multilevel neutral point clamped inverter is proposed for this hybrid system [57]. Moreover, the integration of hydropower plant into the hybrid PV-DFIG system is presented in [58].

The basic advantage of the hybrid PV-DFIG system is to reduce the cost of the traditional systems. A low-cost system is very competitive in the market of renewable energy, especially in rural area. Therefore, to go further for cost derease, a sensorless maximum power point tracking (MPPT) method is proposed for the PV source of the hybrid system. The main idea of this approach is using output powers to estimate the input power. In operation, the powers from GSC and RSC can be applied to estimate the PV power due to balance of DC-link in the hybrid system. A detailed estimation

algorithm is presented in next sections. In our previous research [47], this sensorless MPPT approach is introduced and successfully applied for a stand-alone PV system. Employing this approach for the combined system can decrease the cost compared to the hybrid system with a traditional MPPT method. Using less numbers of required power converters and less numbers of required sensors makes the cost of the hybrid system much cheaper.

5.2.2 Studied System

The proposed system studied in this research is illustrated in Fig. 5.3. In this structure, the DC output of DC/DC converter is directly connected to the DC-link of the back-to-back converter. Therefore, the inverter of PV system is eliminated. That can reduce the cost of the entire system. In this research, the DC/DC converter is Buck-Boost (BB) converter, which has very stable operation and fast-response. The BB converter can maintain the maximum power generation from PV system. This maximum power is supplied to the DC-link voltage. Then the RSC and GSC can convert that DC power into AC power which is fed to the rotor or the grid. The coordination of these converters to handle the power flow is investigated and explained in details in simulation study.

As mentioned above, the combined system can work without the inverter of PV system. Hence it is cost-effective compared to two separate configurations, as shown in Figs. 5.1 and 5.2. Also, all associated circuits of the inverter, such as heat-sink and protection circuits, are removed. That can decrease the cost of maintenance services. Moreover, a sensorless control method is proposed for the hybrid system. This method can reduce the numbers of sensors of PV system, so the cost of the hybrid system can be decreased more. The sensorless method is presented in next sections in detail. Parameters of the proposed system are shown in Tables B.1 and B.3.

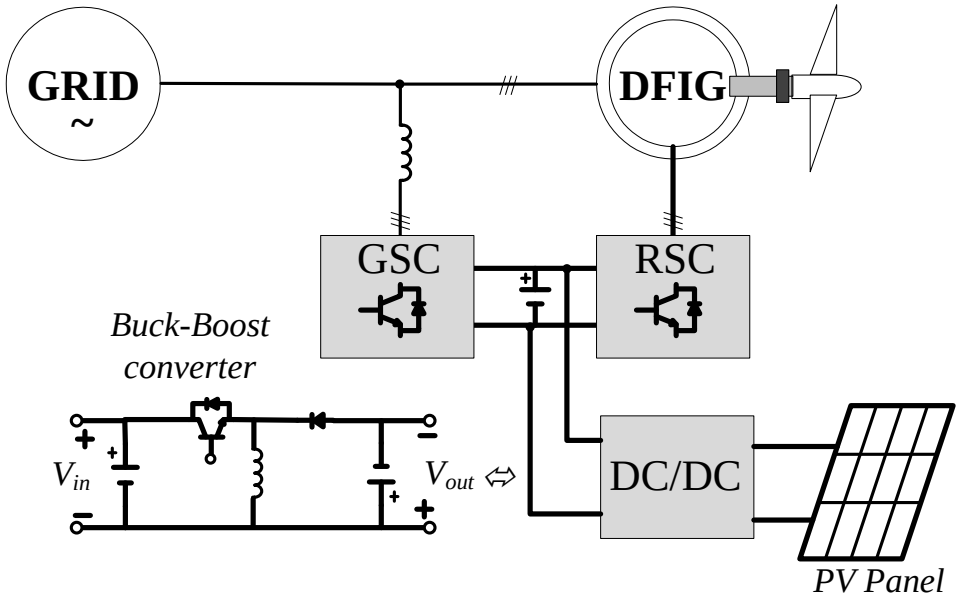

Figure 5.3: Studied system

5.3 PV Modeling and Control

5.3.1 Modeling of PV

An equivalent circuit of a PV module is shown in Fig. 5.4. This circuit consists of a current source in parallel with a diode. The diode and the output resistor mainly determine the characteristics of the PV module. The mathematical relationship between PV current and voltage can be written as [48]:

$$I_{pv} = I_L - I_D \left[\exp\left(\frac{qV_{pv} + qIR_S}{AKT}\right) - 1 \right] \tag{5.1}$$

where I_{pv} and V_{pv} are PV current and voltage respectively, I_D is the diode saturation current, q is the electron charge, A is the material factor of diode, K is the Boltzmann constant, R_S is the series resistor, and T is the absolute temperature.

Environmental conditions, such as temperature and irradiation, strongly affect

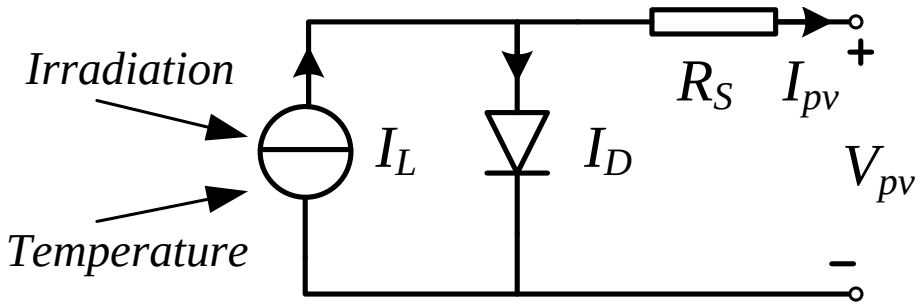

Figure 5.4: Equivalent circuit of PV

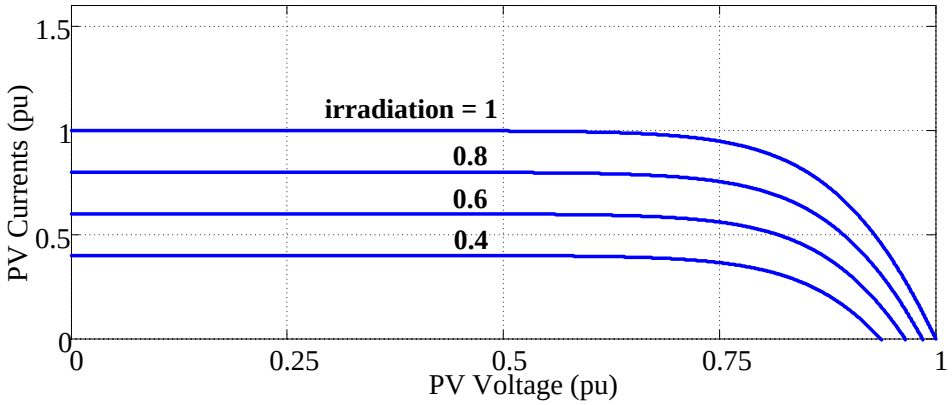

Figure 5.5: Characteristics of PV

the characteristic of the PV module. Therefore, a maximum power point tracking method is required to remain the maximum output power of the PV module. Typical IV-curves of PV are demonstrated in Fig. 5.5.

5.3.2 MPPT Control of PV

The aforementioned issue of PV is that its output power is strongly dependent on environmental conditions and load power. Therefore, a DC/DC converter is typically used to remain the available maximum power of PV regardless of changes from scenario. Researchers have been proposed various structures and methods for MPPT control during the past decades [49–51].

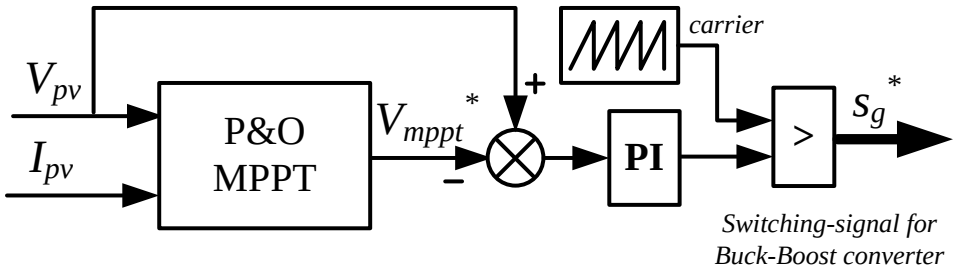

Figure 5.6: Control diagram of Buck-Boost Converter

In this research, a Buck-Boost (BB) converter is employed to maintain the maximum power of PV system as shown in Fig. 5.3. Fig. 5.6 demonstrates the control diagram for BB converter. The P&O MPPT component is very important in this diagram. Based on the instantaneous current and voltage of PV system, this component can point out a relevant reference voltage. In addition, the reference voltage will be gradually modified to track the maximum power point by this component. Hence, the BB converter is controlled to maintain the voltage of PV system similar to the reference voltage.

The P&O MPPT algorithm is illustrated in Fig. 5.7. This algorithm is used in this research because of the simple yet robust advantage [52].

5.4 Sensorless MPPT for Hybrid PV-DFIG

In order to track the maximum power point of PV, the information of PV voltage and current is monitored. Therefore, current and voltage sensors are used to calculate the PV power Ppv, as seen in Fig. 5.6. In this research, a new method is proposed to track the MPP of PV without monitoring the PV power. In the hybrid PV-DFIG system, the DC output of PV is connected to the DC-link of the DFIG converter. Hence, due to balance of DC-link, exchanged powers are conserved, and the GSC and RSC powers can be applied to estimate the PV power. In the other words, the PV

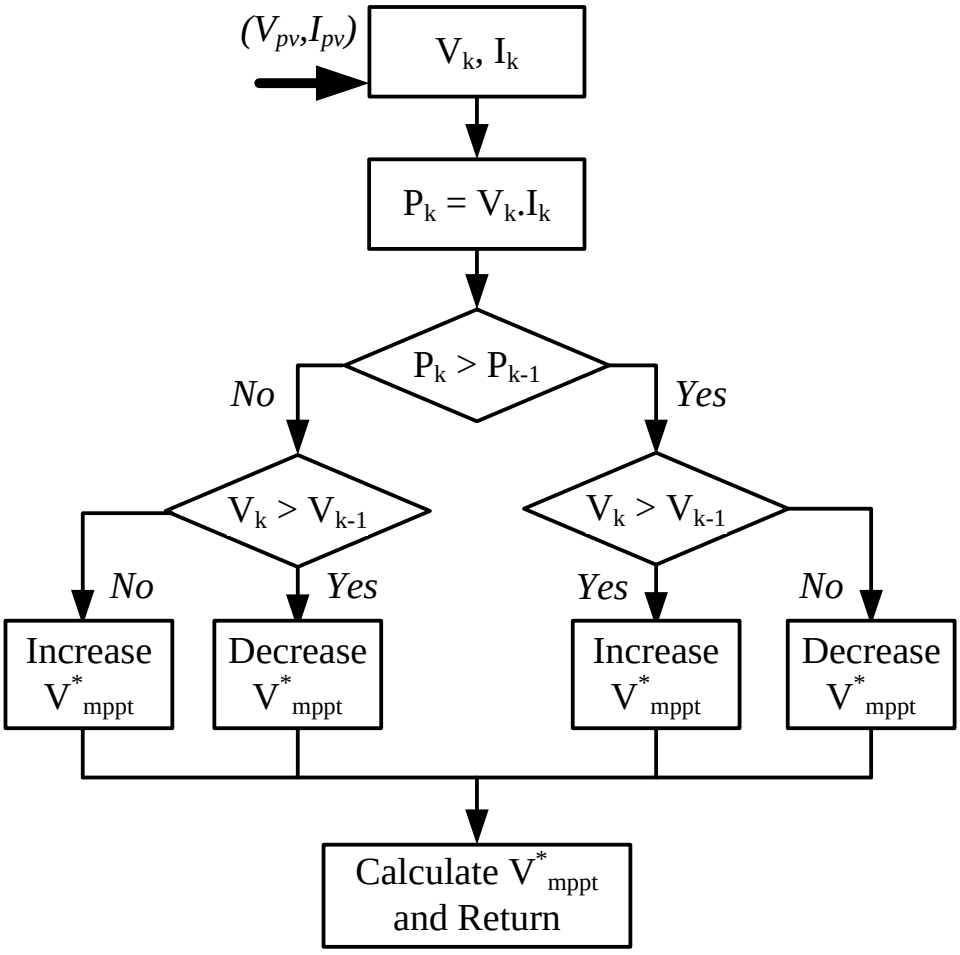

Figure 5.7: P&O MPPT algorithm

power is measured using only available sensors of DFIG system. The power flow of PV, GSC and RSC is illustrated in Fig. 5.8.

The power of GSC P_{GSC} can be calculated as eq. 5.2. However, the power of RSC P_{RSC} is indirectly calculated using the current i_{RSC}, which is noted in Fig. 5.8. The value of i_{RSC} is derived as eq. 5.3. The method to estimate P_{RSC} is shown in Fig. 5.9.

$$P_{GSC} = i_{ga} \times v_{ga} + i_{gb} \times v_{gb} + i_{gc} \times v_{gc} \tag{5.2}$$

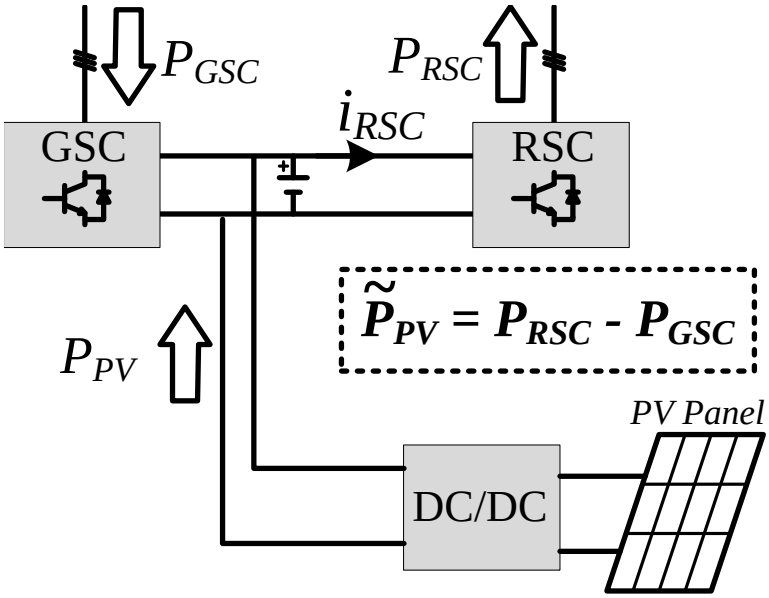

Figure 5.8: Estimation of PV power using RSC and GSC powers

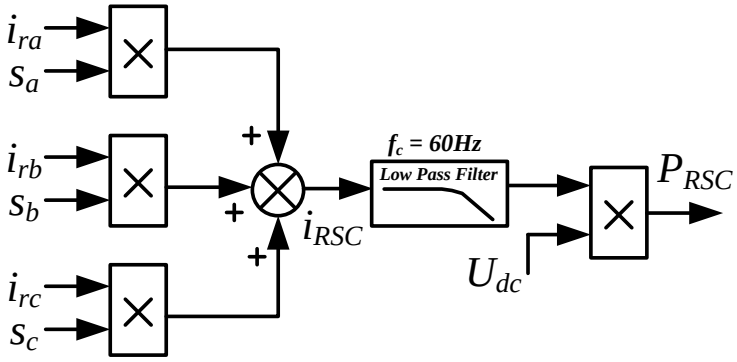

Figure 5.9: RSC power calculation

$$i_{RSC} = i_{ra} \times s_a + i_{rb} \times s_b + i_{rc} \times s_c \tag{5.3}$$

where subscripts g, r, a, b and c are grid side, rotor side, phase a, phase b and phase c respectively. s_a, s_b and s_c are switching values of phase a, b and c on rotor side respectively (s = 0 when switch opens, s = 1 when switch closes).

The sensorless MPPT diagram is demonstrated in Fig. 5.10. The P&O MPPT

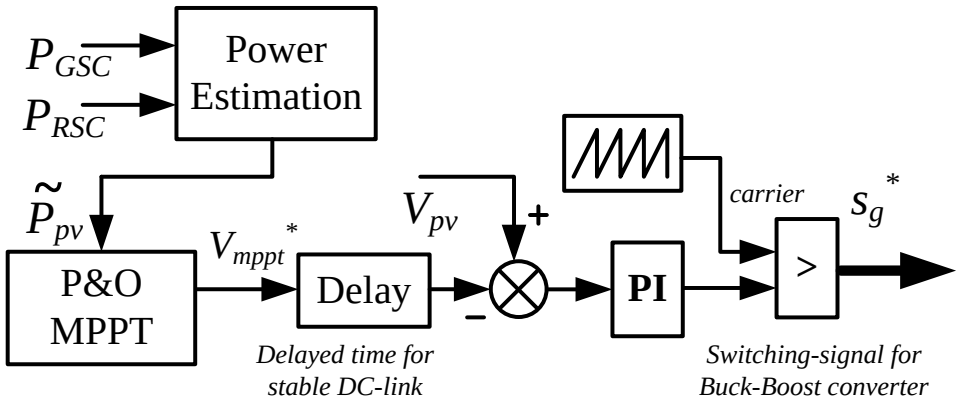

Figure 5.10: Control diagram of sensorless MPPT method

block receives the estimated value of PV power to track optimal voltage. Note that the Delay block is used to keep the reference voltage fixed until the DC-link becomes stable. The conventional hybrid PV-DFIG can eliminate the Inverter and its sensors. Moreover, the sensorless PV-DFIG can eliminate the PV current sensor.

5.5 Simulation Study and Discussion

In this section, the proposed MPPT method is analyzed. The estimated and measured powers of PV system are compared in detail. Then, the coordination control capability of three converters is investigated. One of benefits of DFIG is that it can work under subsynchronous mode, when the wind speed is lower than synchronous speed, and supersynchronous mode, when the wind speed is higher than synchronous speed. The power flow of converters during these modes are varied, as shown in Fig. 5.11.

5.5.1 Feasibility of the Sensorless MPPT Method

This case study is conducted to investigate the proposed MPPT method under changes of irradiation. As seen in Fig. 5.12, the irradiation is changed from 1pu to 0.6pu at

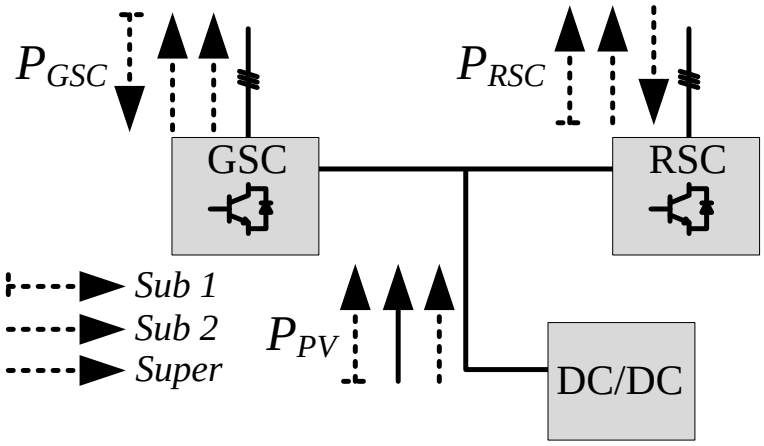

Figure 5.11: Power flow under various modes

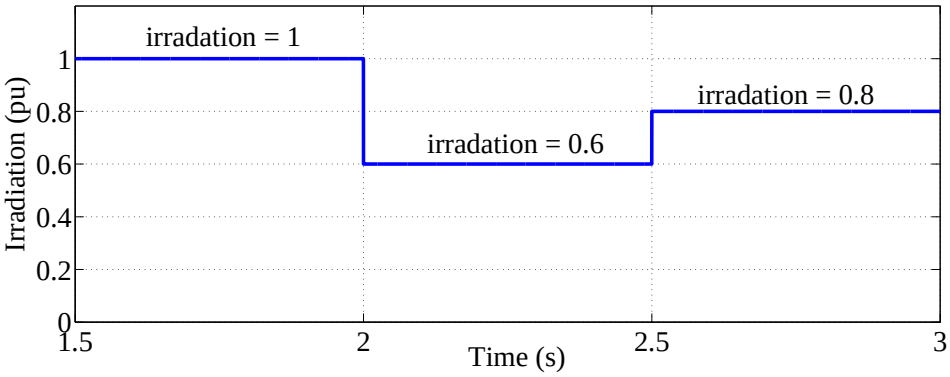

Figure 5.12: Irradiation

t = 2s and from 0.6pu to 0.8pu at t = 2.5s. The output power of the PV system is remained at the maximum power points under irradiation variations, as illustrated in Fig. 5.13. Fig. 5.14 shows the DC-link voltage which is stable at 1pu.

The estimated and measured PV powers are demonstrated in Figs. 5.15 and 5.16. The estimated one is approximately equal to the measured one during changes. However, it takes about 30ms for responses of the estimated power to become stable, as seen in Fig. 5.15. The main reason is that the estimated power is based on AC components, which have a period of 1/60s. The power-voltage curve of the estimated one is shown in Fig. 5.16.

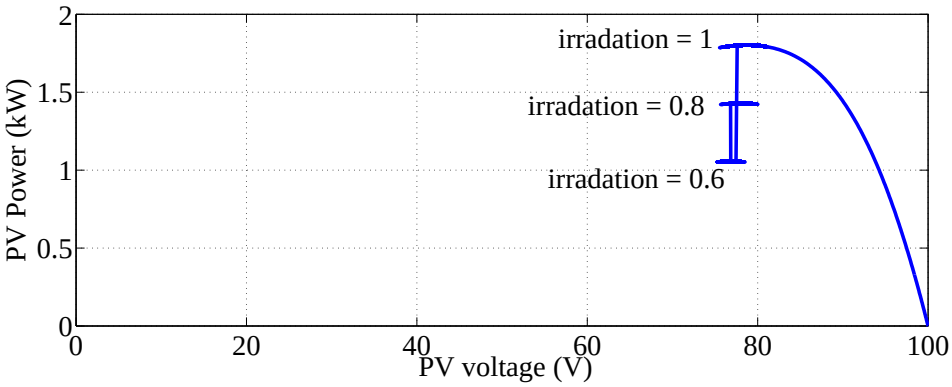

Figure 5.13: Power-Voltage curves

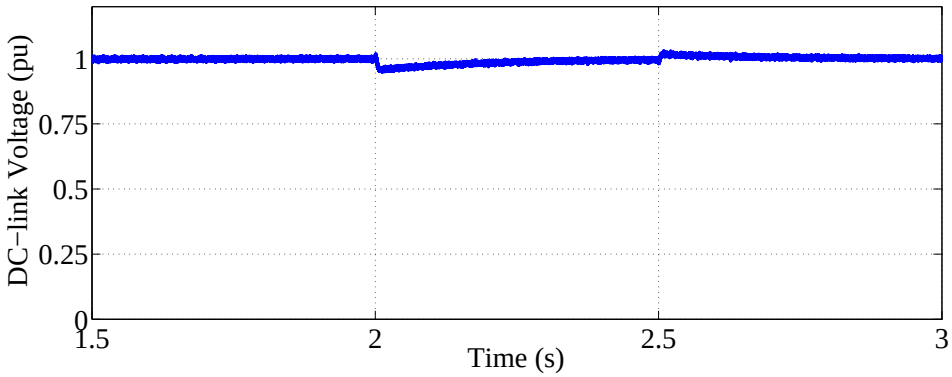

Figure 5.14: DC-link voltage

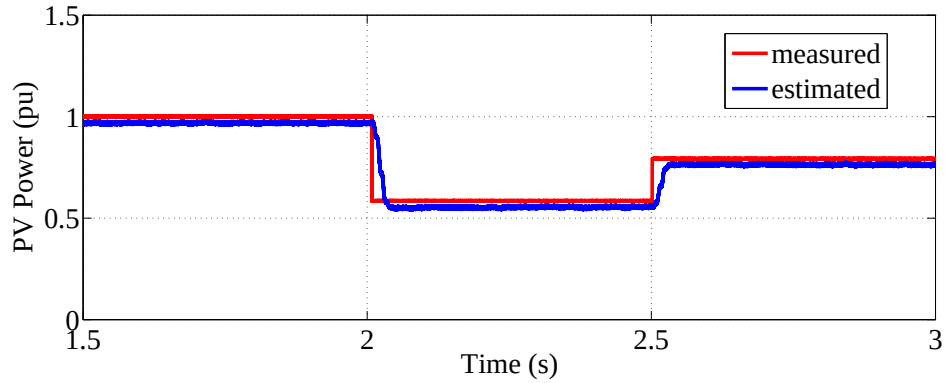

Figure 5.15: Response of estimated power

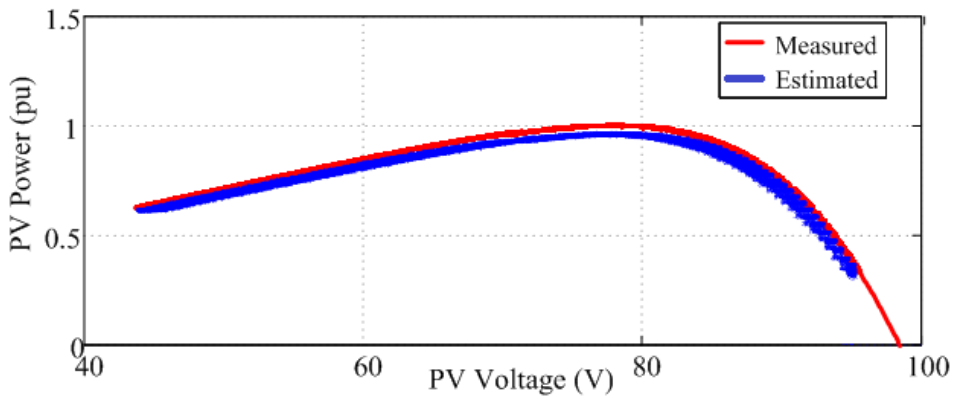

Figure 5.16: Estimated and measured power

5.5.2 Dynamic Response of the Entire System

In this case study, coordinating operations of the system converters are analyzed under different modes. As mentioned before, during various modes of DFIG system, power flow of every converters is interchangeable. Therefore, the converters of the entire system must be able to work harmoniously in various scenarios. Regardless of changes of environmental conditions and control references, the relations of powers must be balanced according to the following equations:

Subsynchronous mode 1: $|P_{RSC}| = |P_{GSC}| + |P_{PV}|$

Subsynchronous mode 2: $|P_{PV}| = |P_{GSC}| + |P_{RSC}|$

Supersynchronous mode: $|P_{GSC}| = |P_{PV}| + |P_{RSC}|$

Figs. 5.17 and 5.18 illustrate the operation under subsynchronous mode 1. In this mode, the RSC converter receives the power from GSC converter and PV system. In addition, the irradiation changes from 1pu to 0.6pu at 2.5s, so the PV power decreases. The RSC power is maintained constant during changes, as seen in Fig. 5.17. GSC currents are changed rapidly to compensate the power decrease of PV, as shown in Fig. 5.18.

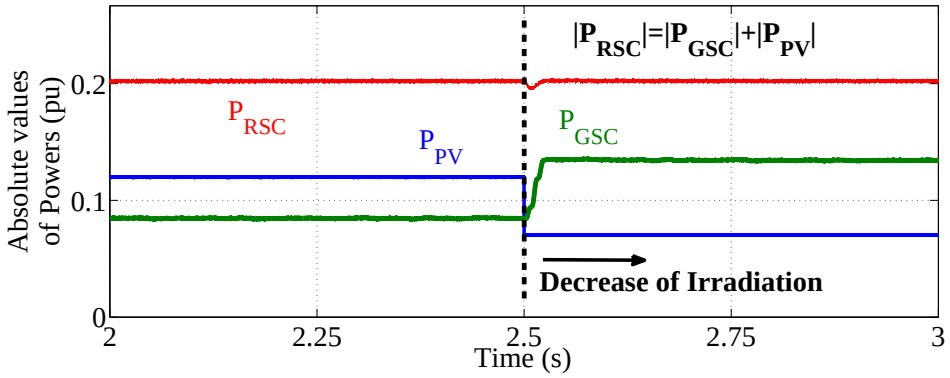

Figure 5.17: Converter powers, subsynchronous mode 1

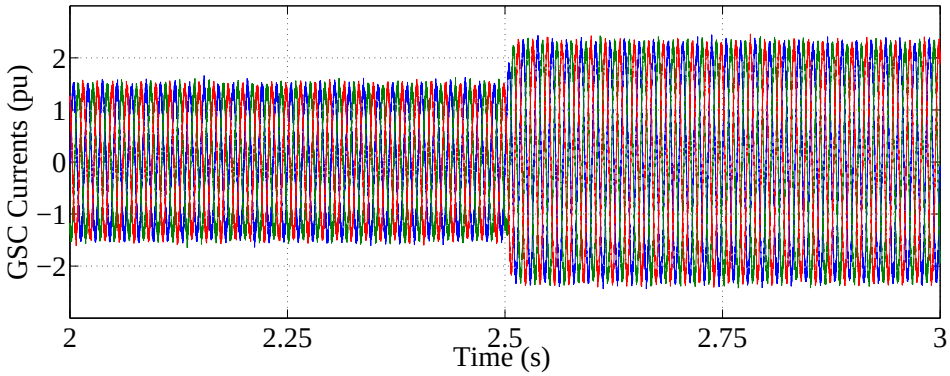

Figure 5.18: GSC currents, subsynchronous mode 1

Responses of subsynchronous mode 2 are shown in Figs. 5.19 and 5.20. In this mode, the PV power is supplied to both RSC and GSC converters, as shown in Fig. 5.19. It means that the PV system can feed enough power for rotor side of DFIG, and the residue power is injected into the grid via GSC. Also, the DC-link control capability is validated in this mode. Fig. 5.20 illustrates the DC voltage increases from 1pu to 1.2pu at t = 2.5s.

Finally, the operations of supersynchronous mode are conducted. As seen in Fig. 5.21, the GSC handles and injects powers from the RSC and the PV system into the grid during this mode. At t = 2.5s, the inverted rotor power is increased because of

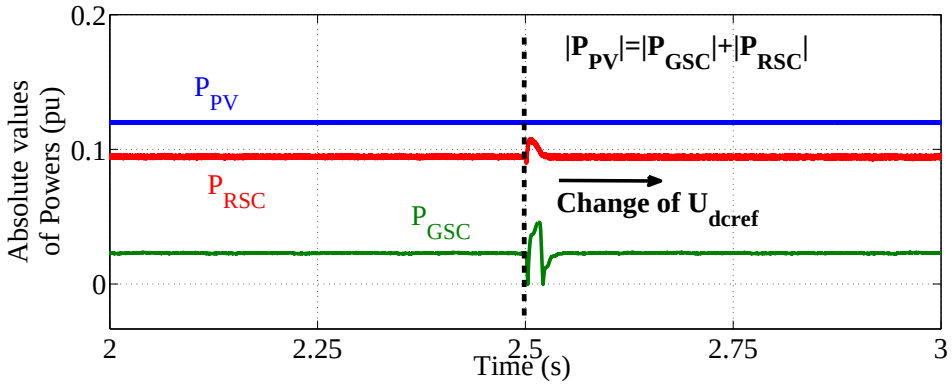

Figure 5.19: Converter powers, subsynchronous mode 2

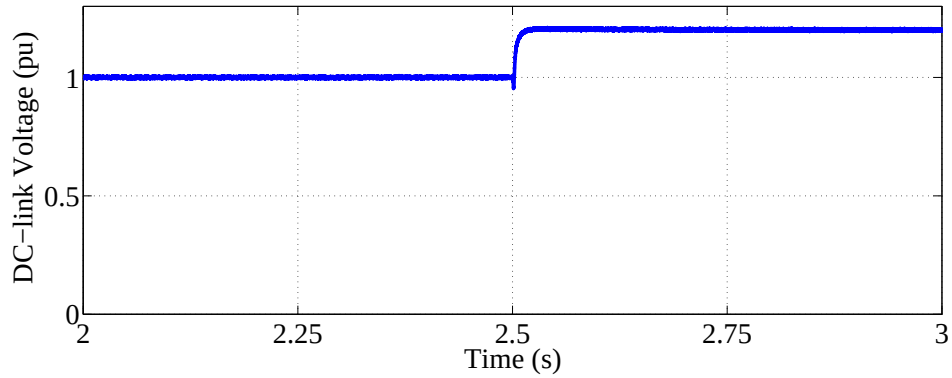

Figure 5.20: DC voltage, subsynchronous mode 2

the mechanical power is increased from 1.1pu to 1.15pu. All converters can work very stable and the DC voltage is remained constant during changes of mechanical input power, as shown in Fig. 5.22.

5.5.3 Discussions on Advantages

Employing the sensorless hybrid system, the cost is decreased because of elimination of the inverter of PV system. It can make higher efficiency due to less power loss. These advantages are discussed in detail as follows:

Reducing cost of system The cost of the hybrid system is reduced because the

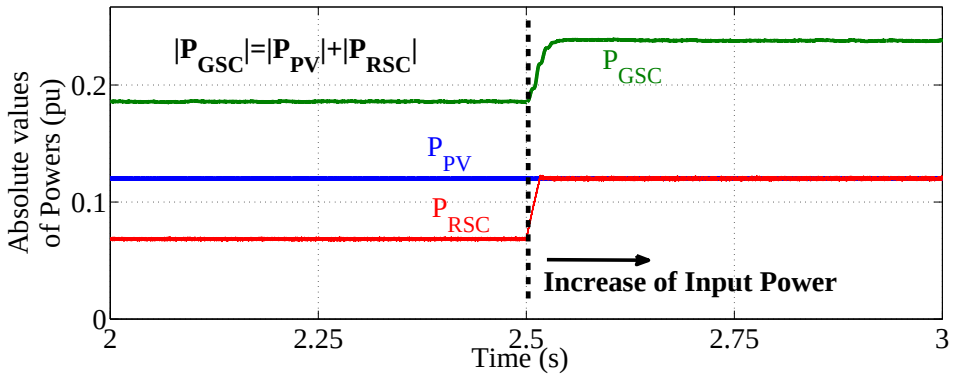

Figure 5.21: Converter powers, supersynchronous mode

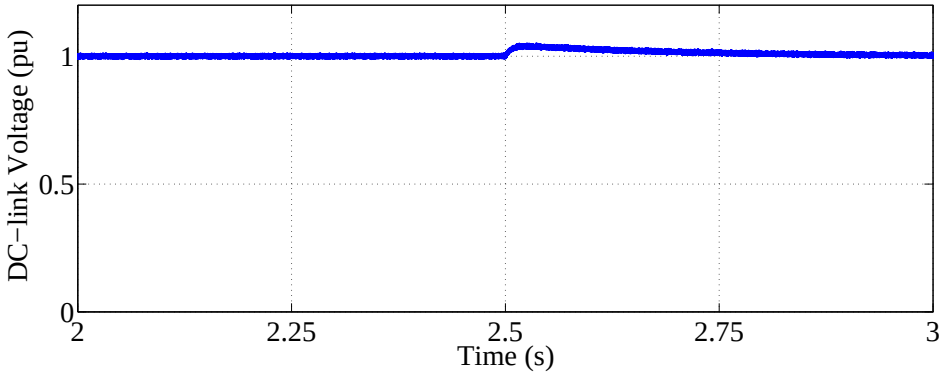

Figure 5.22: DC voltage, supersynchronous mode

inverter and all associated circuits are removed. In addition, the proposed sensorless MPPT method in this research can help the cost lower than the conventional hybrid system. The proposed method is not as complicated as methods using observers. It simply estimate the PV power using the powers of DFIG converters. So it can be applied to the hybrid system easily.

Reducing power loss The numbers of converters in the hybrid system are less than the separate systems. Therefore, it can eliminate the power loss of the PV's inverter. The power loss of 2-level inverter is about 0.015pu [59]. This value is considerable in case of MW-level power plants.

Table 5.1: Sensors used in various systems

	DFIG sensors	Vpv sensor	Ipv sensor	Inverter sensors
Separate PV-DFIG	YES	YES	YES	YES
Hybrid PV-DFIG	YES	YES	YES	NO
Sensorless Hybrid	YES	YES	NO	NO

Integrating to available DFIG system DFIG WTs are the most popular topology recently. There are many available DFIG-based wind power plants. With investigation, appropriate sites can be used to integrate new PV systems. The PV systems with suitable rating can be connected to the available DFIG plants. The cost of these newly-installed PV systems are much lower than the separate PV systems.

5.6 Summary and Discussion

In this research, the sensorless MPPT method of the hybrid PV-DFIG system is proposed. The inverter of the separate PV system is eliminated in the typical hybrid system. In this method, the available sensors of the DFIG system are used to estimate the PV power for MPPT. Therefore, it can remove the PV current sensor of the PV system. Comparisons of sensor utilization are illustrated in Table 5.1.

The performance of the proposed method is demonstrated in simulation study. The three converters can work very well to handle the power flow under various operation scenarios, such as variations of mechanical power and irradiation, changes of DC-link voltage. Properties of the typical hybrid system and the sensorless hybrid system are illustrated in Table 5.2. Advantages and disadvantages of the proposed

Table 5.2: Comparisons between typical and sensorless hybrid PV-DFIG

	Typical hybrid PV-DFIG	Sensorless hybrid PV-DFIG
MPPT capability	YES	YES
Wind speed range	$\omega_s + 30$ to $\omega_s - 30\%$	$\omega_s + 30$ to $\omega_s - 30\%$
Steady time to measure DC-link	No delay	30ms

system are explained as follows:

Advantages:

+ The sensorless system can track the maximum power of PV without the PV current sensor.

+ The sensorless method does not affect the dynamic responses of the entire hybrid system. The system responses are very stable under changes of irradiation, mechanical power and DC-link voltage.

Disadvantages:

+ It takes about 30ms (1/60hz) for the estimation value to be steady.

With the capabilities of MPPT and fast responses, the sensorless hybrid system can be a cost-effective alternative of the two separate systems.

Chapter 6

Module-based Power Systems and Experiments

6.1 Module-based Experiment Systems

6.1.1 Introduction

Since the revolution of electricity in the end of the nineteenth century, electric power has become a crucial foundation to develop human society. The electric power industry shapes and underpins every aspects of life. The electric consumption has grown more and more in the entire world [60]. In addition to the development of the electric infrastructure, the development of human source in power engineering is very important. Electric power experts, engineers and technicians are required not only in industry but also in academy. In order to fulfill the demand, experimental models are important for students to learn and for new engineers to experience and practice. In education, experiments in lab are necessary for students in several main learning methods, such as lecture-based learning and project-based learning [61, 62]. In research, researchers and graduate students also need well-prepared experimental

systems to test and realize their ideas.

Experimental models must be similar to equipments in the field and familiar with theoretical diagrams in books and technical reports. Therefore, experimental systems for training and research are often considered in every lab of universities carefully. In literature, some systems are designed for particular parts of a power system for study and education. Experiments in [63] are used to understand the whole design process of transformers, including design, construction, modeling and analysis. A voltage flicker training facility is presented to provide practical concepts of electric power quality in [64]. In [65], an electricity market simulator can help to figure out pool-based electric markets and the role of power producers. In [66], a machinery laboratory with industrial equipments are also introduced. Conventionally, there are three types of experimental models, such as commercial products, on-demand products and self-made products. These products have disadvantages of high-cost and incapability of customization. These disadvantages will be discussed in detail in next section.

In this research, a new approach of experimental systems is proposed and developed. The proposed system is based on module concepts. Every functional parts of the experimental system are designed into separate modules. Each module represents a small model and can be used for many systems. The modules are easy to handle and arrange, so they can be used in labs and classrooms with small space. In order to demonstrate, this chapter introduces three module-based projects in Power System Lab, Shibaura Institute of Technology: Transmission system and compensation, Hydropower system and Grid-connected inverter for distributed generation (DG). These systems are fundamental but important for research groups to study and analyze. They also can be applied to help users to experience and figure out many practical aspects of the modern power system.

Figure 6.1: Commercial training system (Takahashi Industry)

6.1.2 Traditional Lab Models for Experiments

Experimental models are often employed to instruct electrical students or to train electrical engineers and technicians. There are common three types of training models: commercial products, on-demand products and self-made products. Figs. 6.1 and 6.2 show the commercial and on-demand products respectively. These products are expensive and difficult to update. When faults occur, they cause a lot of troubles due to unclear structures inside. The self-made model is illustrated in Fig. 6.3. This model is easy to check, but its control-interface is inconvenient for users to handle and figure out. Also, users cannot imagine the specific diagram of system, which they learnt from books, when using the self-made model. Moreover, these models have fixed configuration. It is very difficult to customize the structures for various projects.

6.1.3 Development of Module-based Systems

As mentioned before, every functional part of experimental system is built into a separate module. This method can make the experimental system more flexible and

Figure 6.2: On-demand system (Shibaura Institute of Technology)

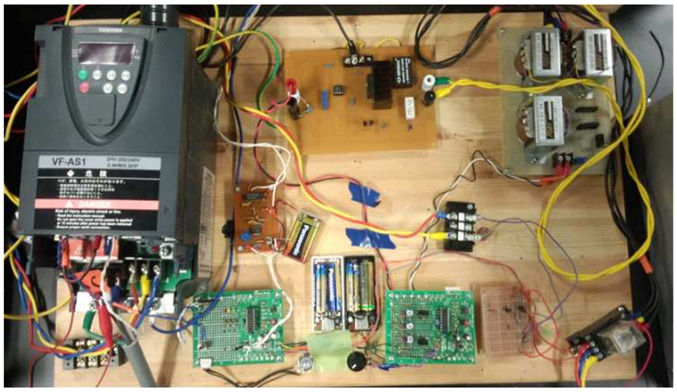

Figure 6.3: Self-made model (Shibaura Institute of Technology)

customizable. A basic module is shown in Fig. 6.4. The module has a small transparent window on the front-panel and handles on both sides. Moreover, a specification sheet is attached on a side of module. The specification sheet can help students or users understand the function and basic values of the module, as illustrated in Fig. 6.4.

Examples of constructed modules are shown in Fig. 6.5. There are many kinds

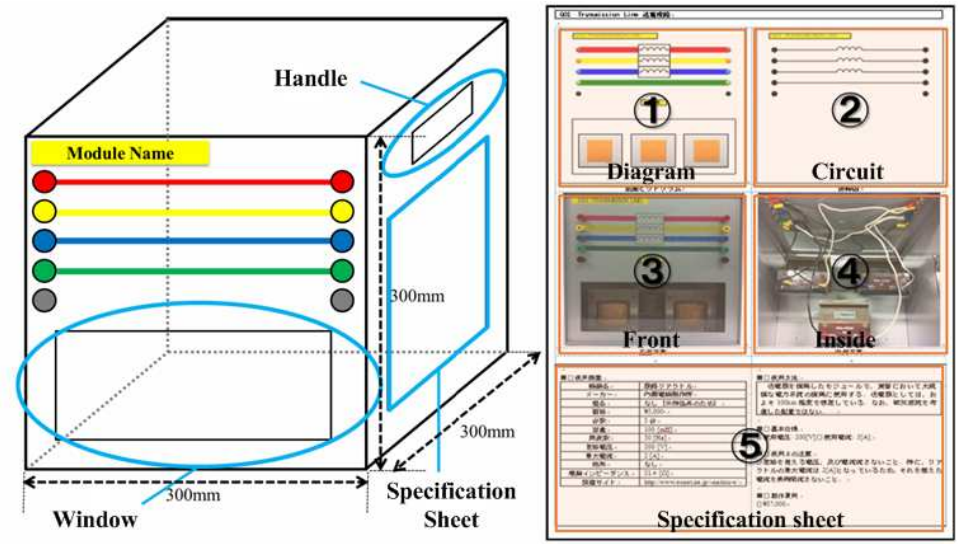

Figure 6.4: Module concept and specification sheet

of modules: transmission lines, transformers, protection devices, generators, motors etc. They are fundamental parts to build various structures of power systems. All modules have the same power terminals, except particular terminals. Hence, it is very convenient to connect them and configure new structures. More types of modules can be referred in [67, 68].

The above modules can offer many relevant usages. Advantages of modules for experimental systems will be stated as follow:

- The modules are designed in small-scale, so that they can be set up in small room. As seen in Fig. 6.6, module-based systems can be placed on a table. It is very convenient to handle the modules as well. Therefore, the module-based system can be used in labs, classrooms and training areas. A group of people can work together around the on-table system, so they can practice group-working skills.

- The module-based system is highly customized due to separate and compact modules. As explained before, the modules are designed in such a way that they can be connected and disconnected to each other quickly. Hence, it is very simple to

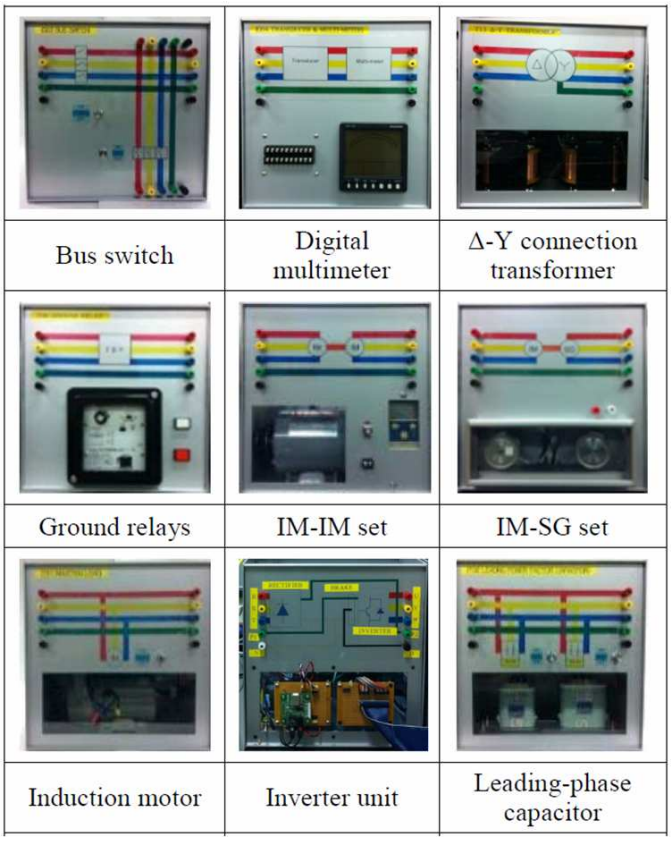

Figure 6.5: Various types of modules

Figure 6.6: Module-based system on a table

construct different structures of power systems using some basic modules. For example, as illustrated in Fig. 6.7 the module IM-SG (Induction motor and Synchronous generator) can be utilized in various projects: Motor system, Hydropower system and Wind power system. This capability makes the module-based system affordable for many projects. Various structures can be built without buying new experimental

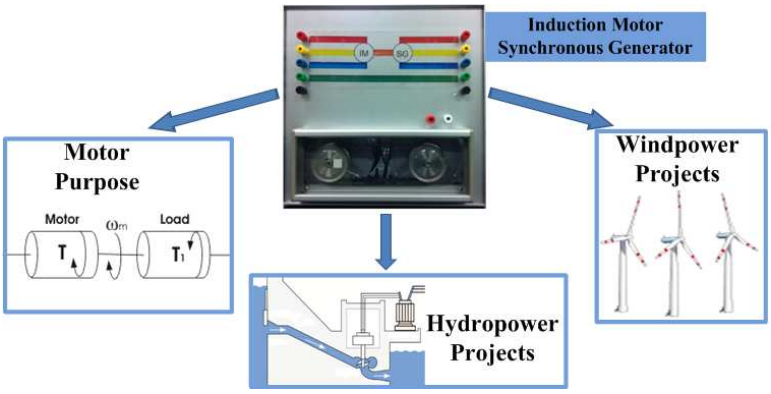

Figure 6.7: One module for various projects

products.

- The module-based system is suitable for visual learning. Users or students can figure out the function of a module because of its informative front-panel and specification sheet. Moreover, small images of front-panels can be applied for discussing. Fig. 6.8 demonstrates the schematic diagram of a basic power system in terms of modules on a whiteboard. Researchers can make these diagrams to explain and discuss theoretical ideas with each others. After understanding these diagrams on the whiteboard, users are almost able to set up the respective experimental system using available modules.

6.2 Demonstration of Power Systems based on Modules

There are various projects which are conducted in Power System Lab, Shibaura Institute of Technology. These projects are based on practical power systems and will be designed into functional modules. In this section, three projects are demonstrated: Transmission system, Hydropower system and Grid-connected inverter system. The module-based projects are suitable for undergraduate and graduate students to study

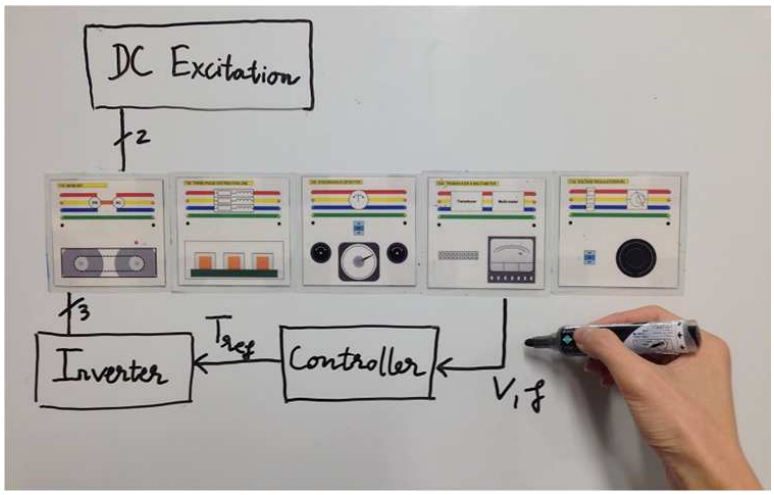

Figure 6.8: Theoretical ideas using modules

and experience. In addition, the projects are planned for Project-based Learning (PBL) programs in future. Particularly, the Transmission system project is applied as a lesson of experimental subject for 3th-grade students in Electrical Engineering Department, Shibaura Institute of Technology.

6.2.1 Transmission System and Compensation

Transmission system is a very fundamental part of a power system. There is common capacitance compensation at the receiving end of the transmission line. The compensators are to compensate the reactive power consumed by inductive loads, such as motors. This experiment provides comprehensive understanding of voltage stabilization using mechanically-switched compensators.

The basic transmission system is shown in Fig. 6.9. In this diagram, two induction motors are connected to the receiving side as induction loads. Two capacitors are also used as compensators. Fig. 6.10 shows the module-based transmission system. In the present, this system is used to teach students as a lesson in experimental class at Shibaura Institute of Technology. Using the system students can learn functions

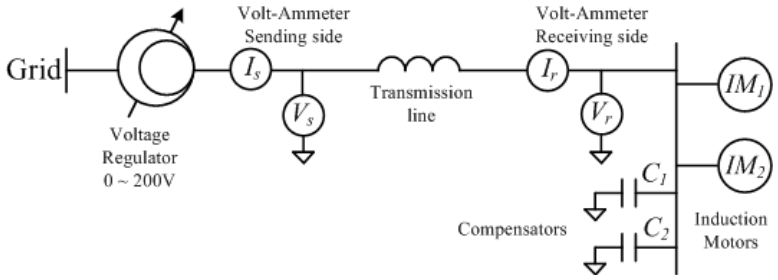

Figure 6.9: Diagram of transmission system

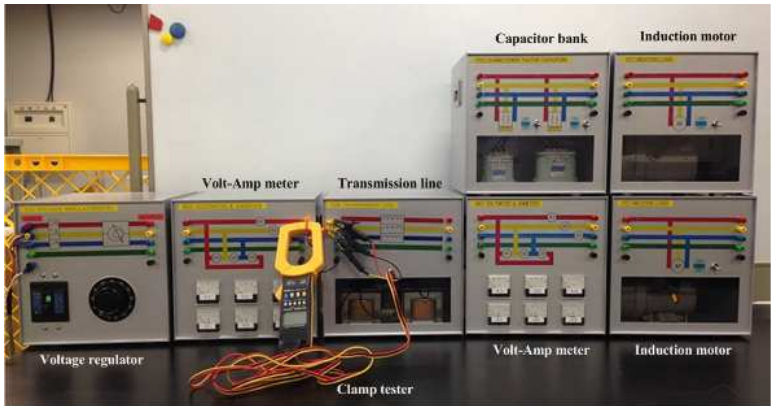

Figure 6.10: Transmission system based on modules

of every components in a practical transmission system.

Table 6.1 shows measured results of voltages, currents and powers of sending and receiving sides in 8 cases. The sending side voltage is maintained at constant 200V. When the motors are running, the receiving side voltage is decreased, and when the capacitors are switched on, the receiving voltage is increased. The measured data will be used to calculate other basic metrics of transmission line, for example power factor, transmission loss, voltage fluctuation rate etc.

6.2.2 Hydropower System

Hydropower plants have been main generation system in the world from the beginning of electricity era. Although they are not popularly used in developed countries today,

Table 6.1: Experimental Results of Transmission System

Case	Inductive Load	Compensator	Sending		Receiving		
			I[A]	P[W]	V[V]	I[A]	P[W]
1	IM1	NO	0.75	45	158	0.78	35
2	IM1	C1	0.27	60	185	0.28	50
3	IM1	C2	0.22	70	200	0.2	65
4	IM1	C1 + C2	0.84	130	235	0.81	120
5	IM1 + IM2	NO	1.23	62	133	1.25	48
6	IM1 + IM2	C1	0.89	75	152	0.89	65
7	IM1 + IM2	C2	0.7	85	162	0.71	75
8	IM1 + IM2	C1 + C2	0.37	118	188	0.36	109

they are still main power sources in many developing countries, such as China, Brazil etc. In a hydropower system, a synchronous generator is a main generation unit. Two controllers including speed governor (GOV) and automatic voltage regulator (AVR) are used to regulate the frequency and the voltage of the generator respectively. This experiment helps users to understand principles and behaviors of main components in the hydropower system: Synchronous generator, GOV and AVR.

The schematic diagram of the hydropower system is illustrated in Fig. 6.11. The synchronous generator is driven by a hydro-turbine, and its torque is supplied by water flow. The GOV control the speed of the generator by adjusting the water vane. Meanwhile, the AVR adjusts the DC current of the field winding to control the output voltage of the generator. In order to build the experimental model, a driving motor and an inverter are used as hydro-turbine and vane-controlled water flow. PIC microcontrollers are applied as both GOV and AVR. In addition, small-scale synchronous generator and induction motor are designed and ordered to make them suitable for module-size. The complete hydropower system based on modules is shown in Fig. 6.12. This on-table system can be set up in experimental room and classroom to train and research.

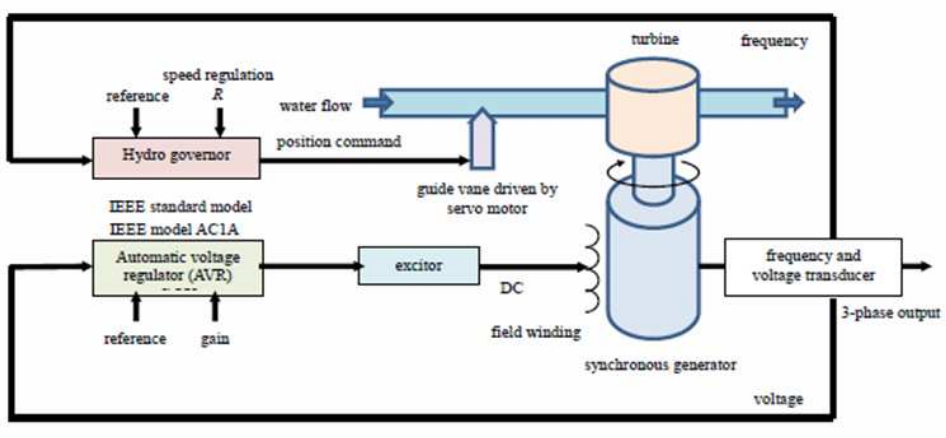

Figure 6.11: Diagram of hydropower system

The system is connected to a varied load. This experiment is conducted to validate the control capability of GOV and AVR. The generator speed and output voltage are controlled at 1pu and 0.8pu respectively. Meanwhile, the load power is changed from 0.3pu to 0.6pu, as seen in Fig. 6.13. GOV and AVR can maintain the speed and voltage stable under variations of load power. Moreover, using this system researchers can conduct more test and analysis for their study, for instance power quality of the system and transient phenomena of synchronous generator under three-phase short-circuit. Note that due to low rating the synchronous generator has high internal resistance. Hence, it can safely operate in three-phase short-circuit fault.

6.2.3 Grid-connected Inverter System

In the past decades, renewable energy has been considered as a main solution for sustainable development of human society. Distributed generation (DG) sources, such as wind turbines, photovoltaic (PV) systems and storage systems, play an important role in structures of renewable energy systems. Particularly, PV and storage systems need a power electronics interface of inverter to inject powers to the grid. Therefore, an experimental model of grid-connected inverter is very necessary to understand

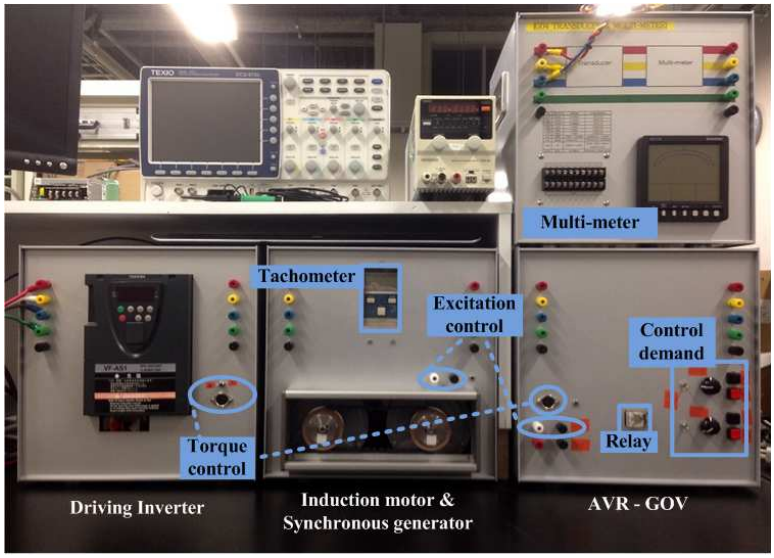

Figure 6.12: Hydropower system based on modules

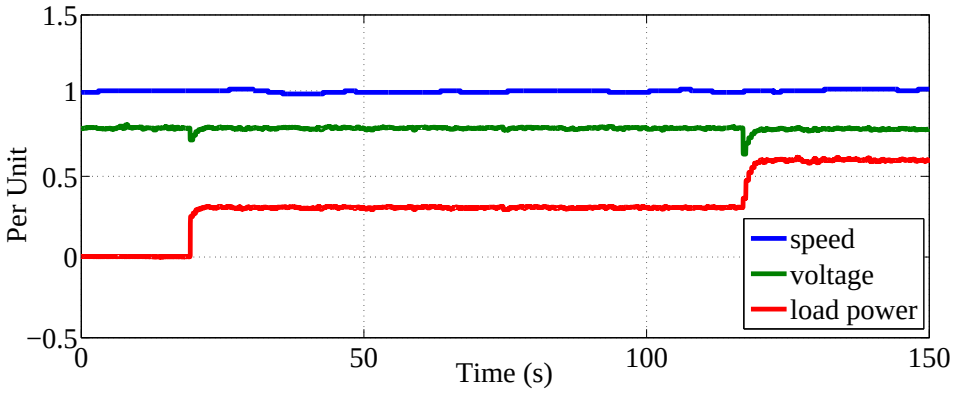

Figure 6.13: Experimental results of hydropower system

PV and storage systems. This experiment is designed to provide basic foundation to study voltage-control and power-control modes of the grid-connected inverter system.

Fig. 6.14 illustrates the schematic diagram of the constructed system. The variable AC source is utilized as the input power. An inverter from Myway company is employed in this system, and a DSP-equipped PE-Board of Myway is used as controller as well. Besides, over-current relay is placed between the inverter and the

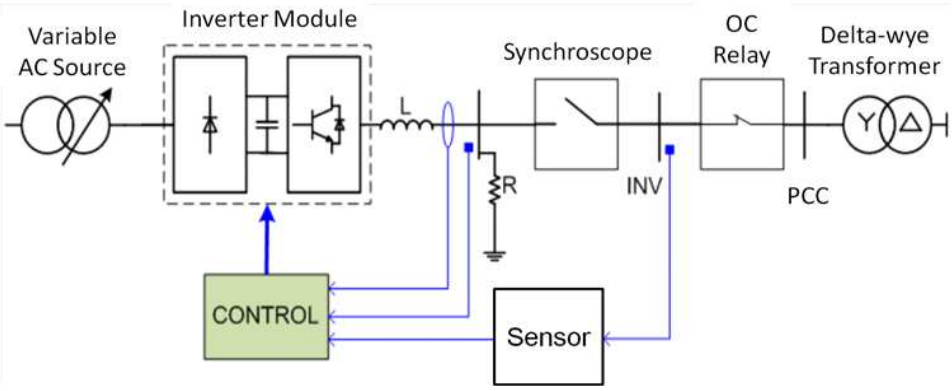

Figure 6.14: Diagram of grid-connected inverter system

grid for protection. The entire grid-connected inverter based on modules is shown in Fig. 6.15. Every module is identical to a functional part in the schematic diagram.

The voltage control mode is conducted for synchronizing before grid-connection. As seen in Fig. 6.16, the inverter voltage (after RL) and grid voltage are similar in terms of magnitude and phase. The phase angles are also stated. After connection, the inverter is switched into power control mode. In this mode, the reference power is set with four different values, which are 0.05pu (50W), 0.1pu (100W), 0.15pu (150W), and 0.2pu (200W). It can be seen that the power control works well by providing the output power according to the given reference values, as shown in Fig. 6.17. Moreover, the grid-connected inverter system can be used to research droop-control methods. In that case, the infinite bus on the grid side is replaced by the synchronous generator, or IM-SG module in Fig. 6.15.

6.3 Wind Power System based on Modules

Wind energy has become more and more important in renewable projects in the world. Hence, knowledge and understanding on Wind Energy Conversion Systems (WECS) are very necessary. In order to investigate and experience a practical WECS, students

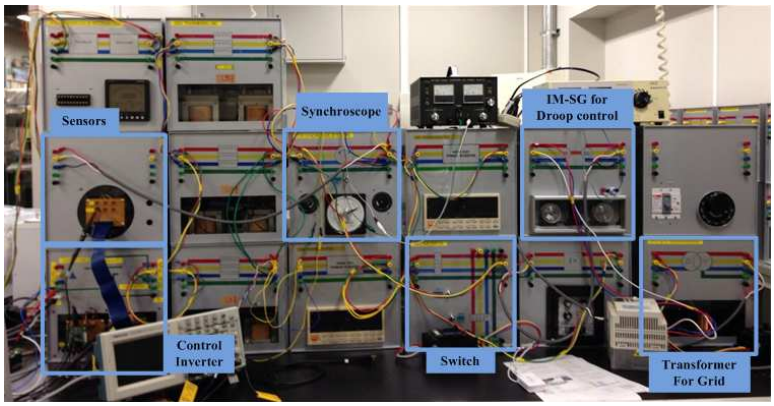

Figure 6.15: Grid-connected inverter system based on modules

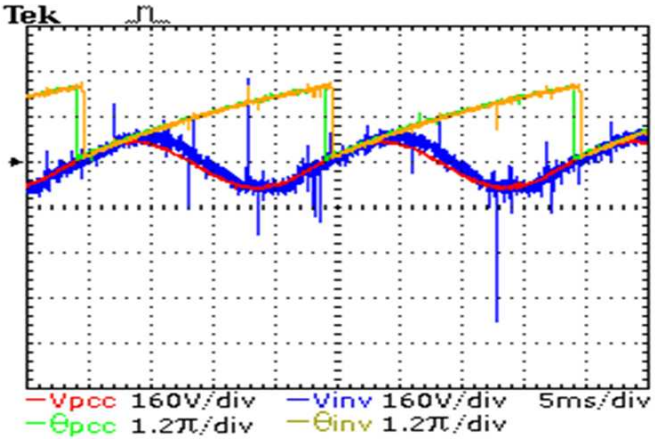

Figure 6.16: Experimental results: voltage control

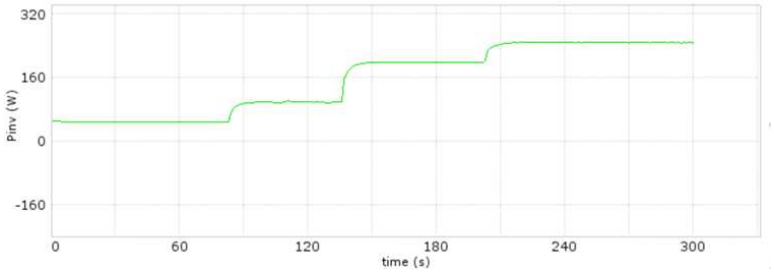

Figure 6.17: Experimental results: power control

and researchers need the system which can simulate the wind speed variations in a region, different types of generators and various strategies of WECS control. In this

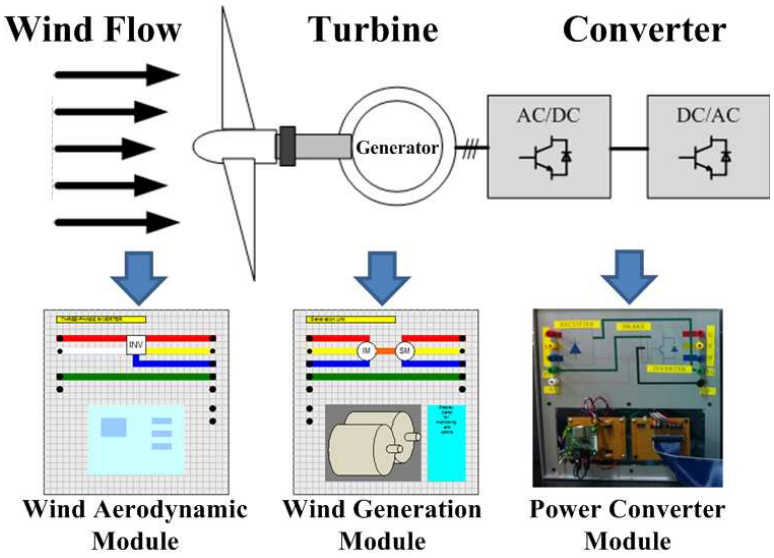

Figure 6.18: Wind energy conversion system and respective modules

ongoing project, a compact module-based system is built to imitate a practical WECS, as demonstrated in Fig. 6.18.

Mechanical input power P_m from the wind turbine is given by the general cube law equation:

$$P_m = \frac{1}{2}\rho A V_w^3 C_p \tag{6.1}$$

Where ρ is density of air, A is area swept by blades, V_w is wind speed and C_p is power coefficient.

In order to implement input power based on wind characteristics, a driving motor is employed. As seen in Fig. 6.19, a controller estimates the torque reference in respect with wind speed and rotor speed (feedback). An inverter is used to control torque. Therefore, the driving motor can drive the synchronous generator as the same way as wind aerodynamic system.

The complete modules are shown in Fig. 6.20. This system is very compact and on-

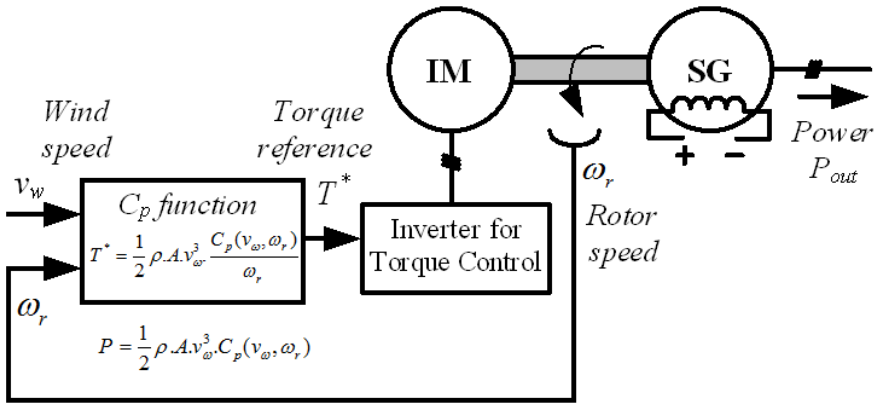

Figure 6.19: Control diagram to simulate wind aerodynamyc system

table size, so it is very convenient for research, education and training. All combined devices are explained in detail as following:

+ Aerodynamic Module (Left): Toshiba inverter VF-AS1 is used to control the demand torque of driving motor according to wind aerodynamics.

+ Generation Module (Middle): The induction motor is used to drive the synchronous generator. An tachometer is also integrated to measure rotor speed. The speed signal is fed to controller.

+ Power Converter Module (Right): A diode-bridge rectifier and a 6-switch inverter are utilized to convert the output power and supply to load or a grid in this research. The DSP-equipped PE-Board from Myway company is also integrated in this module.

+ Computer for monitoring and programming.

6.4 Future Development

A lab-scale smartgrid is a long-term provision. The concept of smartgrid is recently developed, and traditional grids are gradually improved to become smartgrids in many countries. A lab-scale model can be a necessary model to study many concepts of

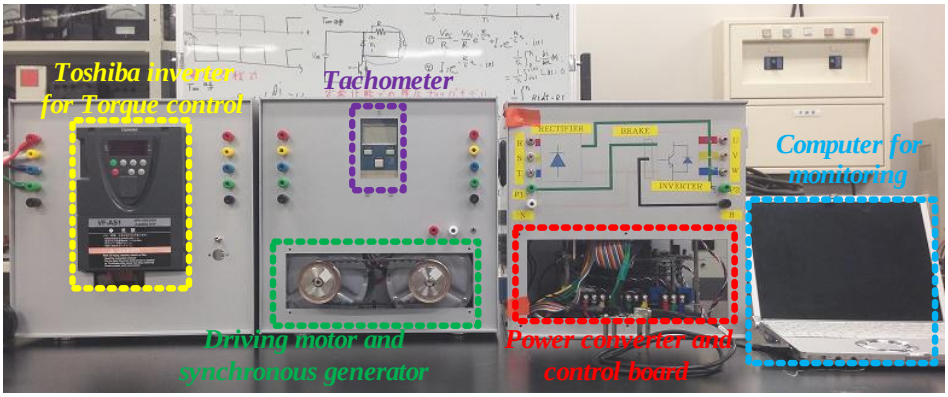

Figure 6.20: Complete system of modules

smartgrids, such as power management and wireless communication.

Eco-Power meter (Panasonic KW1M-R) is used for monitoring and communicating. This device can measure a variety of values: voltage, current, frequency, power factor, power consumption and so on. It is capable of wireless communication. In addition, there are two types: a master and a slave. Modules of the master and slave are shown in Fig. 6.21. The master can receive data coming from several slaves. Moreover, the master can be connected with a computer via Data Logger Light (DLL) by using Ethernet or USB cable. Therefore, it is possible to collect real-time data from many slaves and plot waveforms on the computer.

The Eco-power meter modules are simply integrated in every module-based system, as illustrated in Fig. 6.22. Many available systems, such as Hydropower system, Wind power system and Grid-connected inverter, can be combined to formulate the lab-scale smartgrid, as shown in Fig. 6.23. Note that this module-based smartgrid is very flexible. It can be re-structured into various configurations.

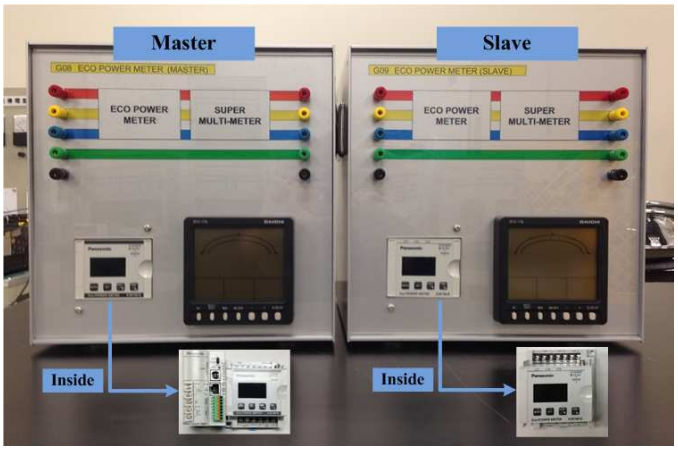

Figure 6.21: Eco-power meter:master and slave

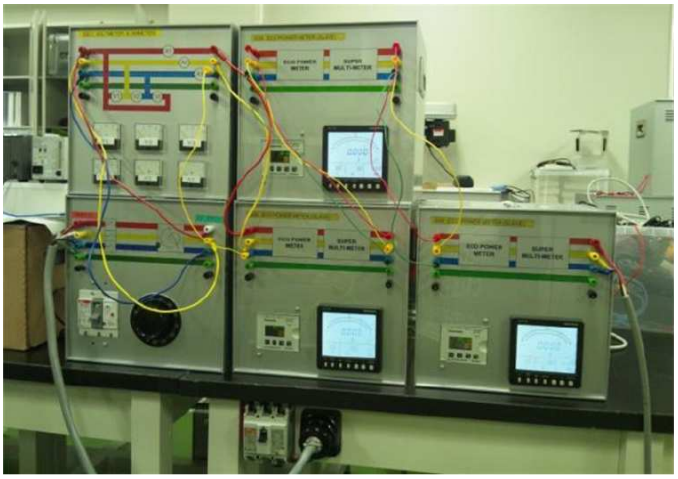

Figure 6.22: Integrated Eco-power meter

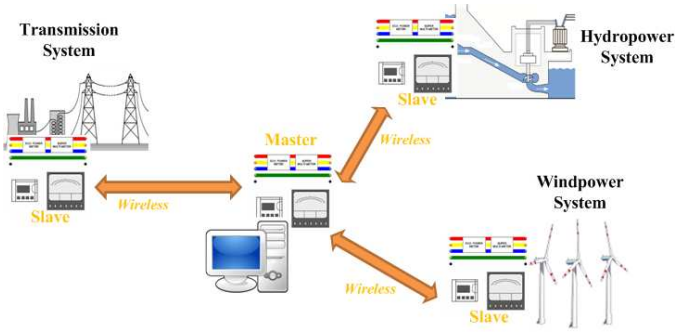

Figure 6.23: Provision for lab-scale smartgrid

Chapter 7

Conclusion and Future Work

7.1 Conclusion

In this research, several aspects of DFIG-based wind power system are addressed. These aspects are very important for DFIG studies, namely control method and structures. This research comes up with several ideas to improve them. The nonlinear control method is proposed to stabilize the DFIG system under several scenarios, as changes of machine parameters and voltage disturbances. As illustrated in simulation study, the proposed method can overcome the issues of a traditional PI-controller for DFIG under these scenarios. The research also introduces a low-cost structure of DFIG. In this structure, a simplified converter is employed to replace GSC. Therefore, it can reduce the cost of the conventional DFIG system. Especially, to maintain the power quality in the simplified structure, the concept of Self-compensating DFIG is proposed and analyzed. The low-cost system is compared with the traditional DFIG system in detail. In addition, the new sensorless MPPT method is presented for the hybrid PV-DFIG system. The hybrid system is introduced in previous research to combine PV and DFIG and reduce the number of converters. The proposed MPPT

method can also reduce the number of PV sensors. Hence, with the sensorless control, the cost of the hybrid system can become cheaper.

Moreover, the module-based experimental systems are demonstrated. These systems are very necessary in modern power system. The author is mainly involved in projects of the Hydropower system and Wind power system. Also, an overview of flicker issues and flicker mitigation methods in Wind power system is presented in Appendix A. It provides fundamental understanding on classical and new mitigation methods.

7.2 Future Work

These studies are considering and conducting:

- The wind power system based on modules is also ongoing. Further experiments are conducting. The expectation is to implement the practical wind data and to analyze influences on power quality.
- Labview hardwares are considered. Next plan is possibly to apply them for energy management of the module-based systems.
- Research on a new flicker mitigation method will be developed. The characteristics of flicker perception is considered to apply in the proposed control diagram.

Appendix A

Flicker Mitigation Control of DFIG

A.1 Introduction

Stable control method is very important for operation of power converters in DFIG WTs, as stated in chapter 3. The control under various scenarios of electrical parts in DFIG WTs is considered carefully. However, the influence of mechanical parts in DFIG WTS on power quality is necessary as well. In this appendix, flicker effect due to wind power fluctuation is presented. Moreover, the state of the art in methods of flicker mitigation control is reviewed and discussed.

A.1.1 History

Flickering lights are one of the most perceivable consequence of voltage disturbances to customers. The influence of lamp characteristics on design of the ac electrical power system dates back to the early days of the electric industry [69].

In 1891, due to visible flicker prevention, power industry pioneers select the standard frequencies as 60Hz and 50Hz in North America and Europe respectively. Difference of frequency is because of that various types of arc lamps are used, open-type

in North America and closed-type in Europe. Later, General Electric published "GE Flicker Curve", which became the voltage flicker design standard in North America, in 1925. In 1964, the standard curve from GE was revised to include periodic and non-periodic pulsations. This is also published in IEEE Standard. In 1994, EPRI published the influence of electronic and compact fluorescent lighting on flicker.

A.1.2 Flicker Definition and Analysis

Voltage flicker is the amplitude modulation of the fundamental frequency voltage waveform by one or more frequencies, typically in the 0 to 30 Hz range. Usually, magnitudes about 0.5% in electric networks can cause visual perception of voltage flicker.

There are some methods of frequency flicker calculation [69, 70]:

1) Single frequency flicker calculation: the flicker magnitude in a waveform with only one modulating frequency is estimated as:

$$percent\,voltage\,flicker = \frac{dV}{V} = \frac{V_{2pk} - V_{1pk}}{V_{2pk} + V_{1pk}} \times 100\% \tag{A.1}$$

where V_{1pk} and V_{2pk} are the minimum positive peak and the maximum positive peak respectively.

2) Weighted flicker average calculation: this quantity is an RMS type of measurement for voltage flicker over a given period. It is similar to the THD index calculation for harmonics.

$$W = C_{LO} \times \sqrt{\sum_{n} \left(\frac{F_n}{C_n}\right)^2} \tag{A.2}$$

where W is weighted average flicker level, n is frequency increment, F_n is measured flicker magnitude at the n^{th} frequency increment, C_{LO} is lowest flicker level on the

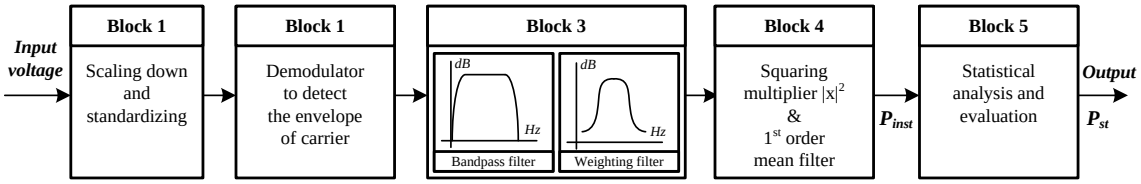

Figure A.1: Flicker Meter Diagram

perceptible flicker curve and C_n is flicker value of the perceptible flicker curve at the n^{th} frequency increment.

A.2 Flicker Meter

In this section, a diagram of flicker meter in accordance with IEC standard is presented [71]. This diagram is used to estimate the short-term flicker severity P_{st}. As demonstrated in Fig. A.1, it can be divided into two parts, which have the main functions as:

1) standardize the input signal and simulation of the lamp-eye-brain response

2) online statistical analysis of the flicker severity

Block 1 standardizes the input voltage according to reference level. Block 2 demodulates the envelope of voltage fluctuation by squaring the input voltage. There are two filters in Block 3. The first filter is bandwidth filter. This filter incorporates a first order high-pass (suggested 3 dB cut-off frequency at about 0.05 Hz) and a 6th order Butterworth low-pass (suggested 3 dB cut-off frequency at about 35 Hz in 50 Hz system and 40 Hz in 60 Hz system). The second filter is a weighting filter that simulates the frequency response of lamp to sinusoidal voltage fluctuations combined with the human visual system. Block 4 includes a squaring multiplier and a first order low-pass filter to simulate non-linearity and memorizing of human brain respectively. The output from Block 4 represents the instantaneous flicker level P_{inst}.

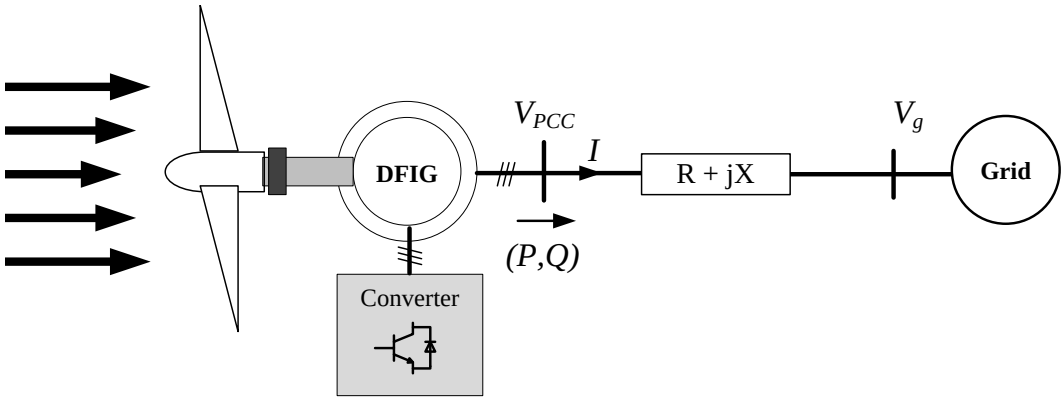

Figure A.2: Grid-connected wind turbine diagram

Block 5 performs an on-line analysis of the flicker level. At first, the cumulative probability function of the flicker levels is derived. Then the short-term flicker severity P_{st} can be calculated according to IEC standard [71].

A.3 Flicker Emission from Wind Turbines

Fig. A.2 shows a simplified single-line diagram illustrating a wind generator (WG) connected to the grid via the equivalent impedance of a distribution line. The injection of active power into the network can affect the output voltage as in eq. A.3. The voltage level fluctuates at the PCC can be derived as a function of the active and reactive power flows at the PCC eqs. A.4 and A.5 [77].

$$V_{PCC} = V_g + I \times (R + jX) \tag{A.3}$$

$$V_{PCC} - V_g = \frac{P - jQ}{V^*_{PCC}} \times (R + jX) \tag{A.4}$$

$$\Delta V = \frac{PR + QX}{V^*_{PCC}} + j\frac{PX - QR}{V^*_{PCC}} \tag{A.5}$$

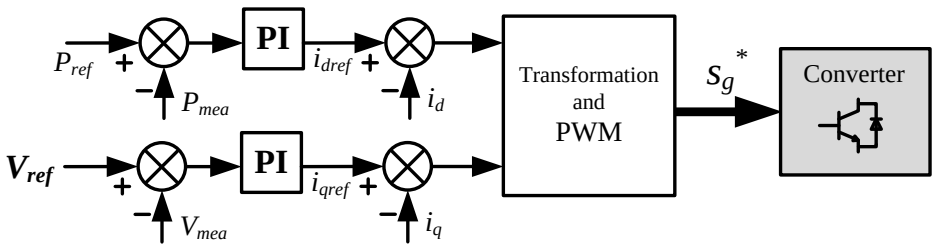

Figure A.3: Reactive power control by monitoring output voltage

where V_g is the grid voltage, V_{PCC} is the voltage at the PCC, I is the line current, P and Q are the active and reactive power flows at the PCC, respectively, X and R are the equivalent line reactance and resistance, respectively, and ΔV is a change in voltage that varies in magnitude and frequency as a function of the injected wind active power and corresponding reactive power flow.

A.4 Review of Flicker Mitigation Method

Flicker mitigation in WECS is conventionally based on reactive power compensation at the PCC. Handling the reactive power is the general method to mitigate flicker effect from wind source in distribution networks. There are also approaches of smoothing the active power output in order to suppress the flicker.

In literature, there are two popular methods of reactive power compensation. The first method is monitoring output voltages directly, as seen in Fig. A.3. This method can keep the voltage constant to reduce flicker emissions. The second method applies the relation of powers and voltage fluctuations. As demonstrated in Fig. A.4, the output power is used to calculate the compensated reactive power. In this section, three structures of flicker mitigation method for WTs are stated: STATCOM integration, Synchronous generator structure and DFIG structure.

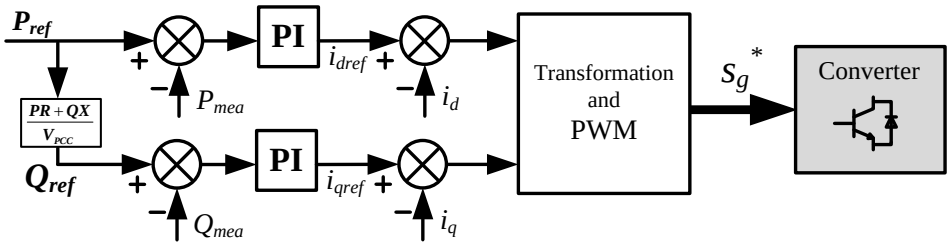

Figure A.4: Reactive power control by monitoring output power

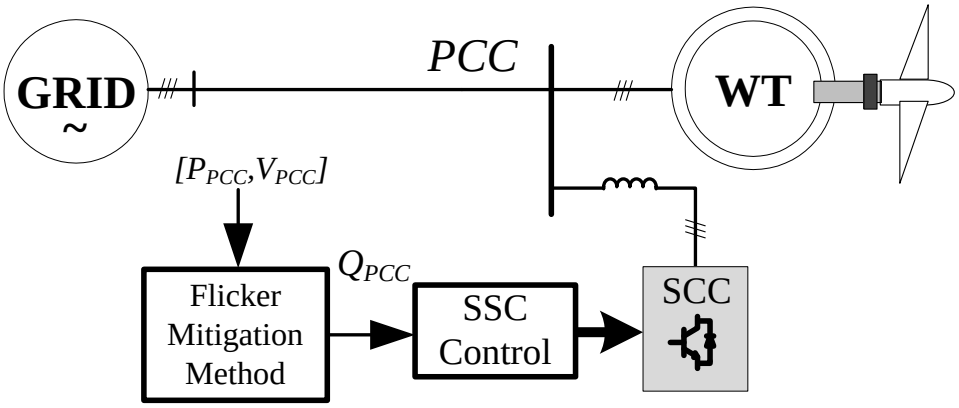

Figure A.5: Flicker Mitigation using STATCOM

A.4.1 STATCOM Integration

The most widely used flicker mitigation implementation by conventional installations is the STATCOM that is capable of controlling the flow of reactive power at the PCC [73]. The methodology employed is based on operating the STATCOM to absorb reactive power at the PCC. The STATCOM can be used for every constructed structures of WTs, for example Fixed-speed or Variable-speed. Fig. A.5 illustrates the diagram of the flicker mitigation method using STATCOM.

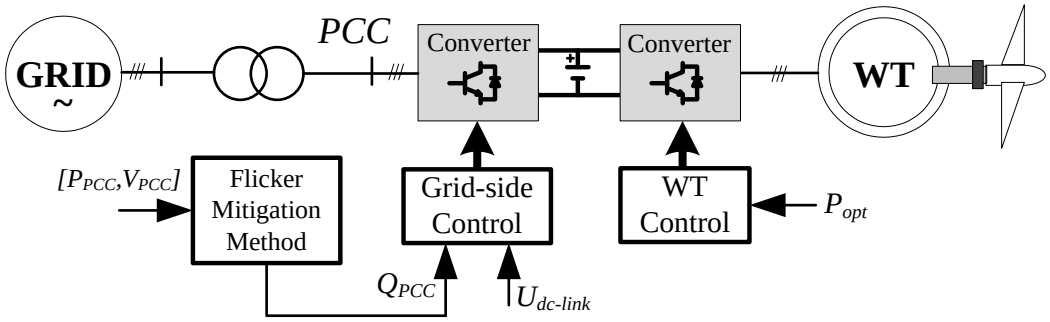

Figure A.6: Flicker Mitigation using power electronics interface of SG

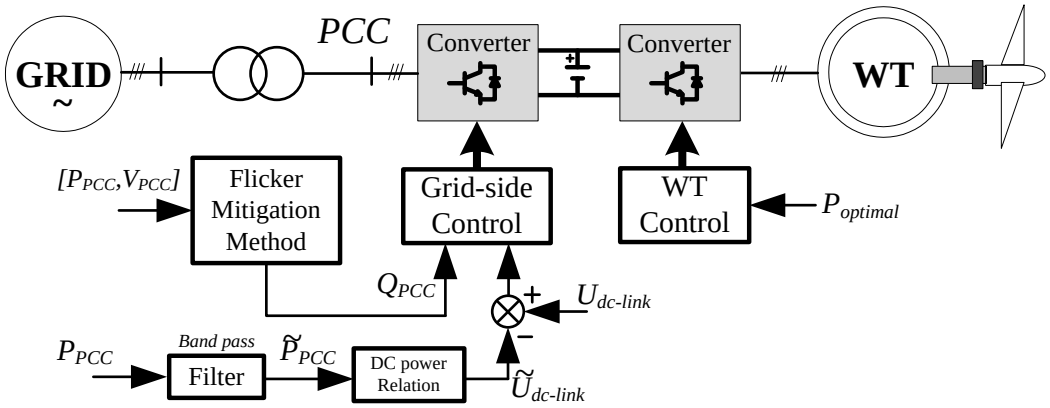

Figure A.7: Flicker Mitigation using DC-link capacitor's energy

A.4.2 Power Electronics Interface of SG

A structure of SG-based WTs consists of a bidirectional power converter. The grid-side converter of this structure can regulate the reactive power to the grid. Taking advantage of this capability, the power electronics interface of SG can be used for flicker mitigation without additional installations [74]. A basic diagram of flicker mitigation using this structure is shown in Fig. A.6. The Block of flicker mitigation method in this diagram is similar to the ones in Figs. A.3 and A.4. In addition, to make the mitigation method more effective, the DC-link energy can be used to smooth the output power [75]. As shown in Fig. A.7, the stored energy of capacitor

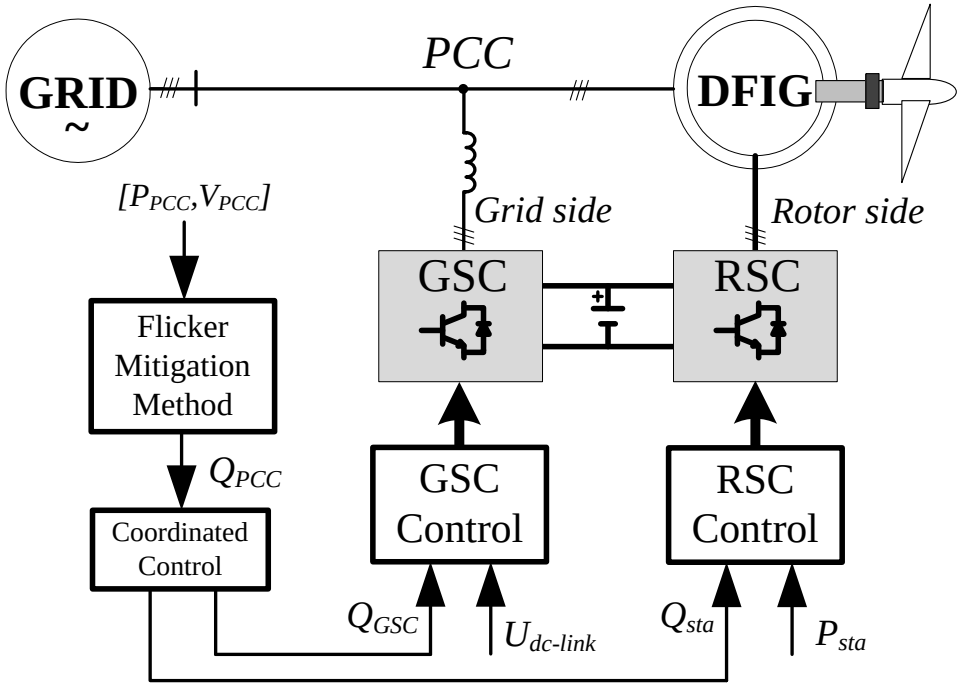

Figure A.8: Flicker Mitigation using DFIG structure

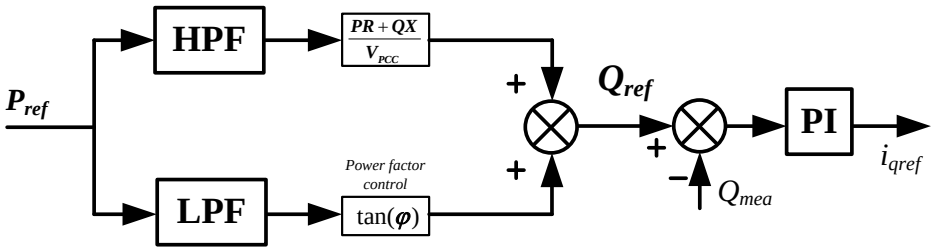

Figure A.9: Decoupling reactive power control for flicker mitigation

is applied to compensate the variations of output power.

A.4.3 Power Electronics Interface of DFIG

Recently, the structure of DFIG WTs can be employed to mitigate flicker emissions effectively [76, 77]. In particular, the DFIG structure can be generate reactive power with two ways: stator of DFIG and GSC of the converter. The coordinated control

method of stator-side and grid-side to regulate the reactive power is illustrated in Fig. A.8. Moreover, a decoupled reactive power control of DFIG structure is proposed in Fig. A.9. This method divides the output power into two components: the flicker-caused component, which is in high-frequency range, and the non fliker-caused component, which is in low-frequency range [78].

Appendix B

System Parameters

Table B.1: DFIG System Parameters

Rated Power	$1MW$
Rated Stator Voltage	$0.69kV$
Rated Frequency	$60Hz$
Pair of poles	1
Stator, Rotor Resistance (R_s, R_r)	$0.0175pu$
Stator, Rotor Leakage Inductance (L_{ls}, L_{lr})	$0.25pu$
Magnetizing Inductance L_m	$5.5pu$
Inertia	$0.75pu$
Rated DC-link voltage	$1200V$
Inductance of Filter	$0.5mH$
DC-link Capacitor	$5000\mu F$
Rated Wind Speed	$9.11m/s$

Table B.2: DFIG System Parameters (small power for PV-DFIG research)

Rated Power	$5kW$
Rated Stator Voltage	$460V$
Rated Frequency	$60Hz$
Pair of poles	1
Inductance of Filter	$10mH$
Stator, Rotor Resistance (R_s, R_r)	$0.02pu$
Stator, Rotor Leakage Inductance (L_{ls}, L_{lr})	$0.06pu$
Magnetizing Inductance L_m	$1.5pu$
Inertia	$0.04kqm^2$
Rated DC-link voltage	$200V$
DC-link Capacitor	$500\mu F$
Rated Wind Speed	$9.11m/s$

Table B.3: PV System Parameters

Open Voltage	$100V$
Short-circuit Current	$25A$
Maximum Power	$1.8kW$
Number of parallel modules	5
Number of series modules	5

List of Grants

Power Academy Grant:

Grant-in-Aid for Doctoral students awarded to support the project "Implementation of Small-Scale Wind Power System" in fiscal year 2014.

List of Publications

Journal papers

Published papers

1. D. Nguyen and G. Fujita, "Stability Enhancement of DFIG Wind Turbines with New Space-Vector based Nonlinear Control", *IEEJ Trans. Power Energy,* vol. 134B, no. 9, pp. 826-833, 2014.

Under-review papers

2. D. Nguyen and G. Fujita, "Power Regulation of DFIG Wind Turbines Using a Low Cost Power Converter", *International Transactions on Electrical Energy System (Wiley).* (Re-submission)

3. D. Nguyen, N. A. Jalalludin, A. Rizqiawan and G. Fujita, "Development of Module-based Experimental Systems for Training and Research of Power Engineering," *IEEE Transactions on Power System.*

4. D. Nguyen and G. Fujita, "Analysis of Sensorless MPPT Method for Hybrid PV-Wind System Using DFIG Wind Turbines", *Sustainable Energy, Grids and Networks (Elsevier).*

International conference papers

1. D. Nguyen and G. Fujita, "Sensorless MPPT Approach for Hybrid PV-Wind System using DFIG Wind Turbines," in *Proc. of International Conference on Electrical Engineering (ICEE)*, Hong Kong, July 2015.

2. D. Nguyen and G. Fujita, "Optimal power control of DFIG wind turbines using a simplified power converter," in *Proc. of IEEE T&D Conference and Exposition*, Chicago, IL, USA, April 2014.

3. D. Nguyen, G. Fujita, and M. N. Muhtazaruddin, "Power Smoothing Control of DFIG Wind Park with Integrated SMES," in *Proc. of IEEE ASC Annual Meeting*, Charlotte, NC, USA, Aug. 2014.

4. D. Nguyen and G. Fujita, "Control of DFIG with New Space-Vector based Hysteresis Current Regulator," in *Proc. of International Future Energy Electronics Conference (IFEEC) 2013*, Tainan, Taiwan, Nov. 2013.

5. D. Nguyen and G. Fujita, "Analysis of self-compensating DFIG for wind energy conversion systems," in *Proc. of the International Universities' Power Engineering Conference (UPEC)*, Dublin, Ireland, Sept. 2013.

6. D. Nguyen and G. Fujita, "Nonlinear Control of DFIG under Symmetrical Voltage Dips with Demagnetizing Current Solution," in *Proc. of International Conference on Power Systems Technology (POWERCON) 2012*, Auckland, New Zealand, Oct. 2012.

Domestic conference papers

1. D. Nguyen and G. Fujita, "Implementation of Small-scale Wind Power System with Module Approach," in *Proc. of IEEJ General Convention 2015*, Tokyo, Japan, Mar. 2015.

2. D. Nguyen, Q. D. Phan and G. Fujita, "The Simple Sensorless Maximum Power Point Tracker for Single-Stage Grid Connection," in *Proc. of IEEJ General Convention 2012*, Hiroshima, Japan, Mar. 2012.

Bibliography

[1] G. W. E. Council. *(2012) Global wind report*, [Online]. Available: http//www.gwec.net/

[2] S. Muller, M. Deicke, and R. W. De Doncker, "Doubly fed induction generator systems for wind turbines," *IEEE Ind. Applicat. Mag.*, pp. 26–33, May-June 2002.

[3] R. Pena, J. C. Clare, and G. M. Asher, "Doubly fed induction generator using back-to-back PWM converters and its application to variable speed wind-energy generation," *Proc. Inst. Electr. Eng. Electr. Power Appl.*, vol. 143, no. 3, pp. 231–241, May 1996.

[4] H. Akagi and H. Sato, "Control and performance of a doubly-fed induction machine intended for a flywheel energy storage system", IEEE Trans. Power Electron., vol. 17, no. 1, pp. 109-116, Jan. 2002.

[5] G. Abad, J. Lopez, M. Rodriguez, L. Marroyo and G. Iwanski, *Doubly Fed Induction Machine, Modeling and Control for Wind Energy Generation*, IEEE Press, Wiley&Sons, Inc., 2011.

[6] B. Hopfensperger, D. J. Atkinson, R. A. Lakin: "Stator-flux oriented control of a doubly-fed induction machine with and without position encoder", IEE Proc. of Electr. Power Appl., 2000, 147, (4), pp. 241-250.

[7] A. D. Hansen, P. Srensen, F. Iov, and F. Blaabjerg, "Control of variable speed wind turbines with doubly-fed induction generators," Wind Eng., vol. 28, no. 4, pp. 411-432, Jun. 2004.

[8] Ekanayake J., Holdsworth L., Jenkins N.: "Control of DFIG wind turbines", IEE Power Eng., 2003, 17, (1), pp. 28-32.

[9] D. Zhi, and L. Xu, "Direct Power Control of DFIG With Constant Switching Frequency and Improved Transient Performance," *IEEE Trans. Energ. Conv.*, vol.22, no.1, pp.110,118, March 2007.

[10] L. Xu, and P. Cartwright, "Direct active and reactive power control of DFIG for wind energy generation," *IEEE Trans. Energ. Conv.*, vol.21, no.3, pp.750,758, Sept. 2006.

[11] B. Singh, N. K. Swami Naidu, "Direct Power Control of Single VSC-Based DFIG Without Rotor Position Sensor," *IEEE Trans. Ind. Appl.*, vol.50, no.6, pp.4152,4163, Nov.-Dec. 2014.

[12] L. Xu; D. Zhi; B. W. Williams, "Predictive Current Control of Doubly Fed Induction Generators," *IEEE Trans. Ind. Electron.*, vol.56, no.10, pp.4143,4153, Oct. 2009.

[13] E. Kamal, M. Oueidat, A. Aitouche, R. Ghorbani, "Robust Scheduler Fuzzy Controller of DFIG Wind Energy Systems,", IEEE Transactions on Sustainable Energy, vol.4, no.3, pp.706,715, July 2013.

[14] C. Wei; L. Qu; W. Qiao, "Evaluation of ANN estimation-based MPPT control for a DFIG wind turbine," *Power Electronics and Machines for Wind and Water Applications (PEMWA), 2014 IEEE Symposium*, pp.1,6, 24-26 July 2014

[15] N. Jouko, "Voltage dip ride through of a double-fed generator equipped with an active crowbar", Nordic wind power conference, March 2004, Chalmers University of Technology.

[16] L. Xu; Y. Wang, "Dynamic Modeling and Control of DFIG-Based Wind Turbines Under Unbalanced Network Conditions,", IEEE Transactions on Power Systems, vol.22, no.1, pp.314,323, Feb. 2007.

[17] Y. Shokri, E. Ebrahimzadeh, H. Lesani, S. Afsharnia, "Performance improvement of DFIG-based wind farm using multilevel cascaded H-bridge converter under unbalanced grid voltage conditions," Environment and Electrical Engineering (EEEIC), 2014 14th International Conference on , pp.158,163, 10-12 May 2014.

[18] Sujod, M.Z.; Erlich, I., "A new protection scheme for three-level NPC converter based DFIG using zero state control," Innovative Smart Grid Technologies Europe (ISGT EUROPE), 2013 4th IEEE/PES, pp.1,5, 6-9 Oct. 2013

[19] J. Jeong, Y. Ju, B. Han, "Wind power system using Doubly-Fed Induction Generator and matrix converter with simple modulation scheme," Power Electronics and Machines in Wind Applications, 2009. PEMWA 2009. IEEE , pp.1,6, 24-26 June 2009.

[20] D. Nguyen and G. Fujita, "Analysis of self-compensating DFIG for wind energy conversion systems," in *Proc. of the International Universities' Power Engineering Conference (UPEC)*, Dublin, Ireland, Sept. 2013.

[21] D. Nguyen and G. Fujita, "Optimal power control of DFIG wind turbines using a simplified power converter," in *Proc. of IEEE T&D Conference and Exposition*, Chicago, IL, USA, April 2014.

[22] S. Shajari, R. Key Pour, "Reduction of battery size and charge-discharge for active power smoothing of DFIG," 11th International Conference on Environment and Electrical Engineering (EEEIC), pp.112,114, 18-25 May 2012.

[23] L. Ran, J. R. Bumby, P. J. Tavner, "Use of turbine inertia for power smoothing of wind turbines with a DFIG,", 11th International Conference on Harmonics and Quality of Power, pp.106,111, 12–15 Sept. 2004.

[24] A. Petersson, *Analysis, Modeling and Control of Doubly-Fed Induction Generators for Wind Turbines,* Ph.D Thesis, Chalmers University of Technology, Sweden, 2005.

[25] P. Sorensen, A. D. Hansen, and P. A. C. Rosas, Wind models for simulation of power fluctuations from wind farms, J. Wind Eng. Ind. Aerodynam. , vol. 90, pp. 1381-1402, Dec. 2002

[26] D. S. L. Dolan and P. W. Lehn, Simulation model of wind turbine 3p torque oscillations due to wind shear and tower shadow, IEEE Trans. Energy Convers. , vol. 21, no. 3, pp. 717-724, Sep. 2006.

[27] L. L. Freris, Wind Energy Conversion System. Englewood Cliffs, NJ: Prentice-Hall, 1990.

[28] R. Tirumala and N. Mohan, "Dynamic simulation and comparison of slip ring induction generators used for wind energy generation", Proc. IPEC-Tokyo, pp.1597 –1602, 2000.

[29] S. Morimoto, H. Nakayama, M. Sanada, and Y. Takeda, Sensorless output maximization control for variable-speed wind generation system using IPMSG, IEEE Trans. Ind. Appl., vol. 41, no. 1, pp. 60-67, Jan./Feb. 2005.

[30] N. W. Miller, W. W. Price, and J. J. Sanchez-Gasca, Dynamic modeling of GE 1.5 and 3.6 wind turbine-generators, *GE-Power Systems Energy Consulting (2003).*

[31] M. Mohseni, S. M. Islam, M. A. Masoum, Enhanced hysteresis-based current regulators in vector control of DFIG wind turbines, IEEE Trans. on Pow. Elect., vol.26. no.1, pp.223–234, 2011.

[32] J. Rodriguez, J. Pontt, C. Silva, S. Kouro, A. Liendo and J. Rebolledo, Hysteresis Current Control of a Vector Controlled Induction Motor and DTC: an assessment, Taylor&Francis Int. J. Electronics, vol. 91, no. 11, pp 639–651, Nov 2004.

[33] D. Nguyen and G. Fujita, "Stability Enhancement of DFIG Wind Turbines with New Space-Vector based Nonlinear Control", *IEEJ Trans. Power Energy,* vol. 134B, no. 9, pp. 826-833, 2014.

[34] J. Lopez, P. Sanchis, X. Roboam and L. Marroyo, Dynamic behavior of the doubly-fed induction generator during three-phase voltage dips, *IEEE Trans. Energ. Conv.*, vol. 22, pp. 709–717, Sept. 2007.

[35] J. Lopez, P. Sanchis, E. Gubia, A. Ursua, L. Marroyo, and X. Roboam, Control of doubly fed induction generator under symmetrical voltage dips, in Proc. Int. Symp. Ind. Electron., Cambridge, U.K, Jul. 2008, pp. 2456-2462.

[36] D. Xiang, L. Ran, P. J. Tavner, and S. Yang, Control of a doubly fed induction generator in a wind turbine during grid fault ride-through, IEEE Trans. Energy Convers., vol. 21, no. 3, pp. 652-662, Sep. 2006.

[37] E. ON. Netz Gmbh. Germany, Grid code regulations for high and extra high voltage, status: Apr. 1, 2006, Report ENENARHS2006, p. 46. [Online]. Available: www.eon-netz.com.

[38] J. Lpez, E. Guba, E. Olea, J. Ruiz, and L. Marroyo, Ride through of wind turbines with doubly fed induction generator under symmetrical voltage dips, IEEE Trans. Ind. Electron., vol. 56, no. 10, pp. 4246-4254, Oct. 2009.

[39] IEEE1547.1, *IEEE standard for interconnecting distributed resources with electric power systems*, 2005

[40] H. Akagi, E. H. Watanabe and M. Aredes, *Instantaneous Power Theory and Applications to Power Conditioning*, IEEE Press, Wiley&Sons, pp. 48–49, 2007.

[41] T. A. Lipo, A supersynchronous doubly fed induction generator option for wind turbine applications, in *Proc. in IEEE PEMWA* Lincoln, USA, 2009.

[42] R. Pena, R. Cardenas, E. Reyes, J. Clare, and P. Wheeler, "Control of a doubly fed induction generator via an indirect matrix converter with changing DC voltage," *IEEE Trans. Ind. Electron.*, vol. 58, no. 10, pp. 4664–4674, Oct. 2011.

[43] N. P. Soe, D. M. Vilathgamuwa, and K. S. Low, "Doubly Fed Induction Generator for wind energy generation using nine-switch power converter," in *Proc. 2011 37th Annual Conf. on IES*, Nov. 2011.

[44] D. Maksimovic, "Design of the Clamped-Current High-Power-Factor Boost Rectifier," in *APEC Conf. Proc.*, Orlando, FL, USA, Feb. 1994.

[45] Y. Jang and M. M. Jovanovic, A comparative study of single-switch three-phase high-power-factor rectifiers, *IEEE Trans. Ind. Appl.*, vol. 34, no. 6, pp. 1327-1334, Nov. 1998.

[46] E. H. Ismail, *Three-phase high quality rectification,* Ph.D Thesis, University of Colorado, Boulder, 1993.

[47] Phan Quoc Dzung, Nguyen Truong Dan Vu, Nguyen Bao Anh, Le Minh Phuong, Le Chi Hiep and Hong-Hee Lee, "The Low-Cost Single-Stage Grid Connected Photovoltaic System with a Modified MPPT Method," in *IEEE Powercon 2012*, Auckland, New Zealand, Oct. 2012.

[48] B. H. Chowdhury, A. W. Sawab, "Evaluating the value of distributed photovoltaic generations in radial distribution systems," *IEEE Trans. Energ. Conv.*, vol. 11, no. 2, pp. 595–600, Sept. 1996.

[49] N. Mutoh, M. Ohno, and T. Inoue, "A Method for MPPT Control While Searching for Parameters Corresponding to Weather Conditions for PV Generation Systems," *IEEE Trans. Ind. Elect.*, vol. 53, no. 4, pp. 1055–1065, Jun. 2006.

[50] X. Wang and A. P. Hu, "An improved maximum power point tracking algorithm for photovoltaic systems," in *Proc. Australasian Universities Power Engineering Conference (AUPEC 2004)*, Brisbane, Australia, Sept. 2004.

[51] C. A. P. Tavares, K. T. F. Leite, W. I. Suemitsu, M. D. Bellar, "Performance evaluation of photovoltaic Solar system with different MPPT methods," in *IEEE IES - 35th Annual Conference (IECON 2009)*, Porto, Portugal, Nov. 2009.

[52] T. Esram, P. L. Chapman, "Comparison of Photovoltaic Array Maximum Power Point Tracking Techniques," *IEEE Trans. Energ. Conv.*, vol. 22, no. 2, Jun. 2007.

[53] A. Bouharchouche, E. M. Berkouk, T. Ghennam, "Control and energy management of a grid connected hybrid energy system PV-wind with battery energy storage for residential applications," in *8th International Conference and Exhibition on Ecological Vehicles and Renewable Energies (EVER 2013)*, Monte Carlo, Monaco, March. 2013.

[54] N. Khemiri, A. Khedher, M. F. Mimouni, "A backstepping control strategy applied to the connected hybrid renewable energy system operated in MPPT," in *8th International Conference and Exhibition on Ecological Vehicles and Renewable Energies (EVER 2013)*, Monte Carlo, Monaco, March. 2013.

[55] M.E. Zarei, B. Asaei, M. E. Nezhad, "Integration of DFIG based wind turbine and PV plant in order to reduce the number of power converters," in *13th International Conference on Environment and Electrical Engineering (EEEIC 2013)*, Wroclaw, Poland, Nov. 2013.

[56] A. Hamadi, S. Rahmani, K. Addoweesh, K. Al-Haddad, "A modeling and control of DFIG wind and PV solar energy source generation feeding four wire isolated load," in *IEEE IES - 39th Annual Conference (IECON 2013)*, Vienna, Austria, Nov. 2013.

[57] E. Ahmed, S. Yuvarajan, "Hybrid Renewable Energy System Using DFIG and Multilevel Inverter," in *Green Technologies Conference, 2012 IEEE*, Tulsa, OK, USA, April. 2012.

[58] I. Mougharbel, Z. Shehab, S. Georges, "Simulation of a hybrid renewable energy system in rural regions," in *IEEE IES - 38th Annual Conference (IECON 2012)*, Montreal, Canada, Oct. 2012.

[59] D. Sato, J. Itoh, "Total loss comparison of inverter circuit topologies with interior permanent magnet synchronous motor drive system," in *IEEE ECCE Asia 2013*, Melbourne, Australia, Jun. 2013.

[60] Mohamed E. El-Hawary, *Introduction to Electrical Power Systems*, IEEE Press, WileySons, 2008.

[61] N. Hosseinzadeh, M. R. Hesamzadeh, M. Korki, "Role of Laboratory in the Education of Modern Power Systems," in *IEEE Power and Energy Society General Meeting (GM 2011)*, San Diego, CA, USA, Jul. 2011.

[62] G. Joos, "The role of laboratory exercises in power engineering education - an opportunity to integrate industrial concepts," in *IEEE Power and Energy Society General Meeting (GM 2008)*, Pittsburgh, PA, USA, Jul. 2008.

[63] W. T. Jewell, "Transformer Design in the Undergraduate Power Engineering Laboratory," *IEEE Trans. Power Syst.*, vol. 5, no. 2, pp. 26–33, May 1990.

[64] W. N. Chang, "A flexible voltage flicker teaching facility for electric power quality education," *IEEE Trans. Power Syst.*, vol. 13, no. 1, pp. 26–33, Feb 1998.

[65] J. Contreras, "Power engineering lab: electricity market simulator," *IEEE Trans. Power Syst.*, vol. 17, no. 2, pp. 26–33, May 2002.

[66] E. R. Collins, "An energy conversion laboratory using industrial-grade equiment," *IEEE Trans. Power Syst.*, vol. 24, no. 1, pp. 26–33, Feb 2009.

[67] Y. Hitotsumatsu, and G. Fujita, "Proposal of New Module-style Power System Training Device," in *International Universities' Power Engineering Conference (UPEC 2012)*, London, UK, Sept. 2012.

[68] T. Hoshino, and G. Fujita, "Visualization of Electric Power by Module-Type Power System Training Device," in *International Universities' Power Engineering Conference (UPEC 2013)*, Dublin, Ireland, Sept. 2013.

[69] M. Halpin, L. Conrad, and R. Burch, *Tutorial on Voltage Fluctuations and Lamp Flicker in Electric Power Systems*, IEEE Power Engineering Society publication 01TP151, 2001.

[70] S. Caldara, S. Nuccio, and C. Spataro, Digital techniques for flicker measurement: Algorithms and implementations analysis, in Proc. IEEE Instrumentation and Measurement Conf., 1999, pp. 656–661.

[71] Electromagnetic Compatability (EMC) Part 4: Testing and Measurement Techniques-Section 15: Flickermeter Functional and Design Specifications, IEC Standard 61000–4–15, 2003.

[72] T. Sun, Z. Chen, F. Blaabjerg, "Flicker mitigation of grid connected wind turbines using a STATCOM", in Proc. 2nd Int. Conf. Power Electronics and Machine Drives (PEMD 2004), pp. 175–180.

[73] Chong Han; Huang, A.Q.; Baran, M.E.; Bhattacharya, S.; Litzenberger, W.; Anderson, L.; Johnson, A.L.; Edris, A.-A.; "STATCOM impact study on the integration of a large wind farm into a weak loop power system", *IEEE Trans. Energ. Conv.*, vol. 23, pp. 226–233, Mar. 2008.

[74] A. Uehara, A. Pratap, T. Goya, T. Senjyu, A. Yona, N. Urasaki, T. Funabashi, "A coordinated control method to smooth wind power fluctuations of a PMSG-based WECS". *IEEE Trans. Energ. Conv.*, vol. 26, pp. 550 - 558, Jun. 2011.

[75] Weihao Hu; Zhe Chen; Yue Wang; Zhaoan Wang, "Flicker mitigation by active power control of variable-speed wind turbines with full-scale back-to-back power converters," IEEE Trans. Energy Convers., vol. 24, pp. 640 - 649, Sept. 2009.

[76] Hee-Sang Ko; Gi-Gab Yoon; Won-Pyo Hong; "Active use of DFIG-based variable-speed wind-turbine for voltage regulation at a remote location", IEEE Trans. Power Syst., vol. 22, pp. 1916 - 1925, Nov. 2007.

[77] Tao Sun; Zhe Chen; Blaabjerg, F.; "Flicker study on variable speed wind turbines with doubly fed induction generators," IEEE Trans. Energy Convers., vol. 20, pp. 896 - 905, Dec. 2005.

[78] Ammar, M.; Joos, G., "Impact of Distributed Wind Generators Reactive Power Behavior on Flicker Severity," *IEEE Trans. Energ. Conv.*, vol.28, no.2, pp.425,433, June 2013.